

ATLAS 1.4 GHz Data Release 2 – I. Observations of the CDF-S and ELAIS-S1 fields and methods for constructing differential number counts

C. A. Hales,^{1,2*}† R. P. Norris,^{2,3} B. M. Gaensler,^{1,3} E. Middelberg,⁴ K. E. Chow,² A. M. Hopkins,^{5,3} M. T. Huynh,⁶ E. Lenc,^{1,3} and M. Y. Mao⁷

¹*Sydney Institute for Astronomy, School of Physics, The University of Sydney, NSW 2006, Australia*

²*Australia Telescope National Facility, CSIRO Astronomy and Space Science, P.O. Box 76, Epping, NSW 1710, Australia*

³*ARC Centre of Excellence for All-sky Astrophysics (CAASTRO)*

⁴*Astronomisches Institut, Ruhr-Universität, Universitätsstr. 150, 44801 Bochum, Germany*

⁵*Australian Astronomical Observatory, P.O. Box 915, North Ryde, NSW 1670, Australia*

⁶*International Centre for Radio Astronomy Research, University of Western Australia, Crawley, WA 6009, Australia*

⁷*National Radio Astronomy Observatory, P.O. Box 0, Socorro, NM 87801, USA*

Draft version 17 October 2018

ABSTRACT

This is the first of two papers describing the second data release (DR2) of the Australia Telescope Large Area Survey (ATLAS) at 1.4 GHz, which comprises deep wide-field observations in total intensity, linear polarization, and circular polarization over the *Chandra* Deep Field-South and European Large Area *Infrared Space Observatory* Survey-South 1 regions. DR2 improves upon the first data release by maintaining consistent data reductions across the two regions, including polarization analysis, and including differential number counts in total intensity and linear polarization. Typical DR2 sensitivities across the mosaicked multi-pointing images are $30 \mu\text{Jy beam}^{-1}$ at approximately $12'' \times 6''$ resolution over a combined area of 6.4 deg^2 . In this paper we present detailed descriptions of our data reduction and analysis procedures, including corrections for instrumental effects such as positional variations in image sensitivity, bandwidth smearing with a non-circular beam, and polarization leakage, and application of the `BLOBCAT` source extractor. We present the DR2 images and catalogues of components (discrete regions of radio emission) and sources (groups of physically associated radio components). We describe new analytic methods to account for resolution bias and Eddington bias when constructing differential number counts of radio components.

Key words: methods: data analysis — polarization — radio continuum: galaxies — surveys — techniques: polarimetric.

1 INTRODUCTION

Radio surveys are a cornerstone of modern astronomy. Counts of extragalactic radio sources per steradian per unit flux density provide fundamental constraints on galaxy evolution, as they implicitly encapsulate both the underlying redshift and luminosity distributions of source populations (e.g. Longair 1966).

In total intensity, the 1.4 GHz source counts are observed to flatten below 1 mJy, though the extent of this flattening is controversial because the results from deep surveys exhibit a large degree of scatter. To illustrate, see the compilation of surveys in Fig. 3

from Norris et al. (2013) where there is a factor of 2 variation in the counts below 1 mJy. Some studies have attributed the large scatter in the faint counts to cosmic variance, namely to intrinsic differences between survey fields caused by source clustering (e.g. Seymour, McHardy, & Gunn 2004). However, significant differences in the counts for fields observed by separate studies, such as the Lockman Hole (Ibar et al. 2009), indicate that calibration and data processing errors may be largely responsible for the scatter. Issues to consider include corrections for bandwidth smearing (e.g. Ibar et al. 2009), Eddington bias (e.g. Simpson et al. 2006), resolution bias (e.g. Bondi et al. 2008), and non-instrumental factors such as source clustering in the field (e.g. Heywood, Jarvis, & Condon 2013). The present conclusion in the literature is that the scatter in the sub-millijansky counts is likely to be significantly affected by data processing differences between surveys (Biggs & Ivison 2006; Condon 2007; Ibar et al. 2009; de Zotti et al. 2010; Condon et al.

* E-mail: chales@aoc.nrao.edu

† Current address: National Radio Astronomy Observatory, P.O. Box 0, Socorro, NM 87801, USA; Jansky Fellow of the National Radio Astronomy Observatory.

2012; Heywood, Jarvis, & Condon 2013). This conclusion motivates the need for studies that describe data reduction and analysis procedures in detail, so as to facilitate robust comparisons with other works and encourage future improvements.

To date, very few surveys dedicated to extragalactic polarized radio sources have been conducted, primarily because of correlator limitations that have required polarization capabilities to be sacrificed for spectral resolution. Polarization surveys at 1.4 GHz include the NRAO VLA Sky Survey (NVSS; Condon et al. 1998) observed with the Very Large Array, which encompasses 82% of the sky at resolution full-width at half-maximum (FWHM) $45''$ to a root mean square (rms) sensitivity in polarization of $0.29 \text{ mJy beam}^{-1}$, surveys of the European Large Area *Infrared Space Observatory* Survey-North 1 (ELAIS-N1) region observed using the Dominion Radio Astrophysical Observatory (DRAO) Synthesis Telescope by Taylor et al. (2007) over 7.43 deg^2 with resolution FWHM $\sim 50''$ to $78 \mu\text{Jy beam}^{-1}$ and in a deeper follow-up study with the same facility by Grant et al. (2010) over 15.16 deg^2 to $45 \mu\text{Jy beam}^{-1}$, and the Australia Telescope Low-Brightness Survey (ATLBS; Subrahmanyan et al. 2010) which encompasses two fields observed with the Australia Telescope Compact Array (ATCA) over a total of 8.42 deg^2 with resolution FWHM $\sim 50''$ to $\sim 80 \mu\text{Jy beam}^{-1}$. A summary of polarization surveys at other radio wavelengths is presented by Tucci & Toffolatti (2012). By cross-matching polarized 1.4 GHz sources with mid-infrared counterparts, Taylor et al. (2007) identified the population of polarized millijansky sources as being extragalactic radio sources powered by AGNs. Grant et al. (2010) found that the polarized emission from these sources was likely to originate in extended radio lobes. Mesa et al. (2002) and Tucci et al. (2004) found an anti-correlation between the fractional linear polarization and total intensity flux densities of NVSS sources; faint sources were more highly polarized. This finding was supported for ELAIS-N1 sources by Taylor et al. (2007) and Grant et al. (2010), and for ATLBS sources by Subrahmanyan et al. (2010). Tucci et al. (2004), Taylor et al. (2007), and Grant et al. (2010) found that the Euclidean-normalised differential number-counts of polarized sources flattened at linearly polarized flux densities $L \lesssim 1 \text{ mJy}$ to levels greater than those predicted by Beck & Gaensler (2004); the latter predicted polarized source counts to μJy levels by convolving total intensity source counts with a fractional polarization distribution modelled on NVSS data. O'Sullivan et al. (2008) were unable to reproduce the observed flattening in a population modelling study. The observed flattening suggests the emergence of systematic changes in polarized source properties with decreasing flux density, such as higher ordering of magnetic fields in fainter sources, or perhaps the emergence of an unexpected faint population. To examine the emerging fractional polarization anti-correlation and source count flattening trends in more detail, deeper and higher angular resolution observations of the 1.4 GHz polarized sky are required.

In this work we present reprocessed and new 1.4 GHz observations of the *Chandra* Deep Field-South (CDF-S; Galactic coordinates $l \approx 224^\circ$, $b \approx -55^\circ$; Norris et al. 2006) and ELAIS-South 1 (ELAIS-S1; $l \approx 314^\circ$, $b \approx -73^\circ$; Middelberg et al. 2008) regions, obtained as part of the Australia Telescope Large Area Survey (ATLAS) project with the ATCA. We collectively refer to these previous ATLAS papers as Data Release 1 (DR1) and denote the present work Data Release 2 (DR2). Given that DR1 did not include polarization analysis of the ATLAS data, we have chosen to reprocess the original observations to ensure consistent and improved data reduction and analysis between both the total intensity and polarization data and the two independent ATLAS regions. In prepara-

tion for ATLAS DR2, we have developed new tools to ensure accurate calculation of the statistical significance of flux density measurements in linear polarization (Hales et al. 2012a) and to ensure accurate measurement of these flux densities using the BLOCAT source extractor (Hales et al. 2012b).

The motivations for ATLAS DR2 are to (i) present a detailed description of our data reduction and analysis procedures to inform future deep surveys such as those being developed for SKA Pathfinder facilities around the world (see summary of facilities described by Beck et al. 2012 and Norris et al. 2013), (ii) compute differential number counts for total intensity and linearly polarized objects (total intensity counts were not included in DR1), and (iii) investigate the nature of faint polarized sources and consider possible explanations for the fractional polarization trend seen in previous studies. Clearly, biases introduced at an early stage of data reduction have the potential to propagate through to the final data in a non-linear fashion, affecting the ability for that data to be used for unplanned and novel experiments in the future (e.g. Crawford 2009). In this paper (Paper I) we focus on point (i) from above, regarding data reduction and the development of new techniques to produce high fidelity data suitable for investigating points (ii) and (iii). Results and discussion regarding points (ii) and (iii) will be presented in Paper II (Hales et al. 2014).

This paper is organised as follows. In Section 2 we describe our ATLAS radio data and ancillary mid-infrared and optical data. In Section 3 we outline our radio data reduction and post-processing procedures to obtain mosaicked images of total intensity, linear polarization (using rotation measure synthesis), and additionally circular polarization for the two ATLAS regions. In Section 4 we describe instrumental effects of time-average smearing, bandwidth smearing, and polarization leakage, our methods to account for them in our ATLAS data, and the effective survey area boundaries. In Section 5 we detail how radio components were detected and extracted in total intensity, linear polarization, and circular polarization, and how their flux densities were corrected to account for subtle noise-induced systematics. In Section 6 we describe our implementation of two cross-identification and classification schemes: the first to group components into sources, to associate these sources with infrared sources, and to classify them according to their multiwavelength properties; and the second to associate linearly polarized components or polarization upper limits with total intensity counterparts and to classify these associations based on their polarized morphologies. In Section 7 we describe in detail corrections required to calculate total intensity and linear polarization differential number-counts, including a new fully analytic method to account for resolution bias. In Section 8 we present the ATLAS DR2 total intensity and linear polarization images, and the radio component and source catalogues. We conclude in Section 9. For reference, a selection of important symbols used in this work is presented in Table 1.

2 OBSERVATIONAL DATA

2.1 Radio Data

ATLAS observations of the CDF-S and ELAIS-S1 fields were obtained with the ATCA (Frater, Brooks, & Whiteoak 1992), a synthesis telescope consisting of six 22 m alt-az antennas on an east-west baseline. Each antenna is equipped with linearly polarized feeds used to measure all four polarization products (XX , YY , XY , YX), from which all four Stokes parameters

Table 1. Selection of important symbols used in this work.

Symbol	Description	Defined
I_{MFS}	total intensity mosaic produced using multi-frequency synthesis approach	Section 3.2
V_{MFS}	circular polarization mosaic produced using multi-frequency synthesis approach	Section 3.2
I_i, Q_i, U_i	i 'th frequency channel mosaic in total intensity, Stokes Q , or Stokes U	Section 3.3
$\sigma_{Q,i}, \sigma_{U,i}$	rms noise map of i 'th frequency channel mosaic in Stokes Q or Stokes U	Section 3.5
$\sigma_{Q,U,i}$	map of combined rms noise for Stokes Q and Stokes U in i 'th frequency channel	Section 3.5
I_{CA}	total intensity mosaic produced using channel average approach	Section 3.5
L_{RM}	linear polarization mosaic produced using rotation measure synthesis	Section 3.5
$\sigma_{\text{RM}}(x, y)$	rms noise map for L_{RM}	Section 3.5
ϖ	bandwidth smearing ratio (observed divided by true surface brightness)	Section 4.2
K_{LEAK}	total intensity to linear polarization leakage mosaic	Section 4.3
$L_{\text{RM}}^{\text{CORR}}$	L_{RM} corrected for polarization leakage	Section 4.3
F^{AREA}	survey area	Section 4.4
$S_{\text{peak}}, S_{\text{int}}$	peak or integrated surface brightness (more generally, S denotes flux density)	Section 5.1
A_{S}	detection signal-to-noise ratio	Section 5.1
V^{AREA}	visibility area for detection	Section 5.1
θ, B	observed or beam full-width at half-maximum	Section 5.3
Θ	deconvolved angular size	Section 5.3
γ	slope of differential number-counts, $dN/dS \propto S^{-\gamma}$	Section 5.4
S_{ML}	deboosted flux density using maximum-likelihood scheme	Section 5.4
dN_{H03}/dS	differential number-count fit from Hopkins et al. (2003)	Section 5.4
dN_{H03M}/dS	modified version of dN_{H03}/dS	Section 5.4
f_{Π}	distribution of fractional linear polarization ($\Pi \equiv L/I$)	Section 5.4
L_{UL}	linear polarization upper limit	Section 6.2.1
r, e	resolution or Eddington bias corrections	Section 7.1
Θ_{max}	maximum intrinsic angular size for detectable component	Section 7.1.1
$\tilde{\sigma}$	local rms noise divided by local bandwidth smearing ratio	Section 7.1.1
$f_{\tilde{\sigma}}$	probability distribution for $\tilde{\sigma}$	Section 7.1.1
h	integral angular size distribution	Section 7.1.1
η	angular filling factor for linearly polarized emission ($\Theta_{\text{L}}/\Theta_{\text{I}}$)	Section 7.1.1
$dN_{\text{detectable}}/dS$	differential number-counts that are observable	Section 7.1.1
Θ_{med}	median largest angular size	Section 7.1.1
Θ_{min}	minimum intrinsic angular size for detected component to be classified as resolved	Section 7.1.2
dN_{resolved}/dS	resolved detectable number-counts	Section 7.1.2
$dN_{\text{unresolved}}/dS$	unresolved detectable number-counts, assuming ideal case without measurement bias	Section 7.1.2
$dN_{\text{unresolved-obs}}/dS$	unresolved detectable number-counts, accounting for measurement bias	Section 7.1.2

(I, Q, U, V) can be derived. Noise diodes in the feed horns of each antenna replace the need to observe a polarization position angle calibrator to derive absolute XY phase.

The two ATLAS fields were observed in mosaic mode using ATCA's standard continuum correlator setup, FULL128.2. This correlator configuration enabled observation of 2×128 MHz bandwidth windows centred on 1344 and 1432 MHz, with each 128 MHz window divided into 32×4 MHz non-independent channels. A correlator cycle time of 10 seconds was used. The full width at half maximum (FWHM) of the primary beam at these frequencies is $\sim 35'$. The standard ATCA primary flux density calibrator PKS B1934–638 (Reynolds 1994) was used for both ATLAS fields. The secondary calibrators¹ for the CDF-S and ELAIS-S1 fields were PKS B0237–233 and PKS B0022–423, respectively.

Both ATLAS fields consist of multiple pointings, as shown in Fig. 1. Each pointing was observed using a number of complementary ATCA array configurations to maximise uv -plane coverage; we show the typical uv -plane coverage for ATLAS pointings in Fig. 2. Some pointings are more sensitive than others due to non-uniform time allocation. The original DR1 CDF-S observations combined 7 pointings from Koekemoer, Mobasher, & Nor-

ris (2003) (ATCA Project ID C1035) with 21 ATLAS pointings (ATCA Project ID C1241). To boost sensitivity in the CDF-S field, in DR2 we have included 11 additional pointings from Koekemoer, Mobasher, & Norris (2003), making use of all 18 suitable pointings from their data. We have also included new CDF-S observations of the 21 ATLAS pointings, obtained in the period 2005 January to 2006 March. Observing dates, array configurations, and net integration times of the CDF-S data used in this work are shown in Table 2; pointing centres are given in Table 3. For the ELAIS-S1 field with 20 pointings, we have reprocessed the same raw DR1 data as outlined by Middelberg et al. (2008). The baselines measured for the CDF-S and ELAIS-S1 fields cover the range 31–6000 m and 46–5969 m, respectively.

2.2 Ancillary Data

We supplemented our 1.4 GHz radio observations with data at infrared and optical wavelengths, as described below, to enable source classifications using multiwavelength cross-identifications.

2.2.1 Infrared Data

Spitzer Space Telescope (Werner et al. 2004) observations encompassing the CDF-S and ELAIS-S1 ATLAS fields were car-

¹ <http://www.narrabri.atnf.csiro.au/calibrators/>

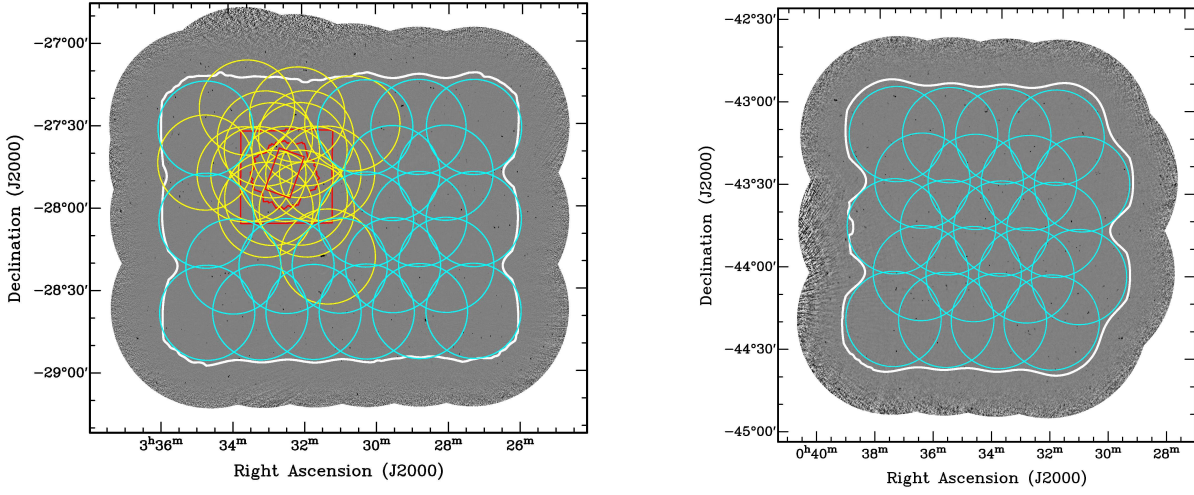


Figure 1. Overview of mosaicked observations of the CDF-S (left) and ELAIS-S1 (right) ATLAS fields; background images are of continuum total intensity (see Section 3.2) with equally-scaled shading levels. Circles indicate the locations and $35'$ half-power primary beam widths of the pointings. The CDF-S field consists of 39 pointings: 18 of these were observed by Koekemoer, Mobasher, & Norris (2003) (yellow circles), while the remaining 21 pointings were observed solely by ATLAS (cyan circles). The rotated red rectangle indicates the GOODS-South field (Giavalisco et al. 2004). The red irregular polygon and outer red square indicate the 2MS CDF-S (Luo et al. 2008) and extended-CDF-S (Lehmer et al. 2005) fields, respectively. All 20 pointings within the ELAIS-S1 field were observed solely by ATLAS. The thick outer contour (white) in each field indicates the survey area boundary (see Section 4.4). SWIRE observations (Lonsdale et al. 2003) encompass each ATLAS field.

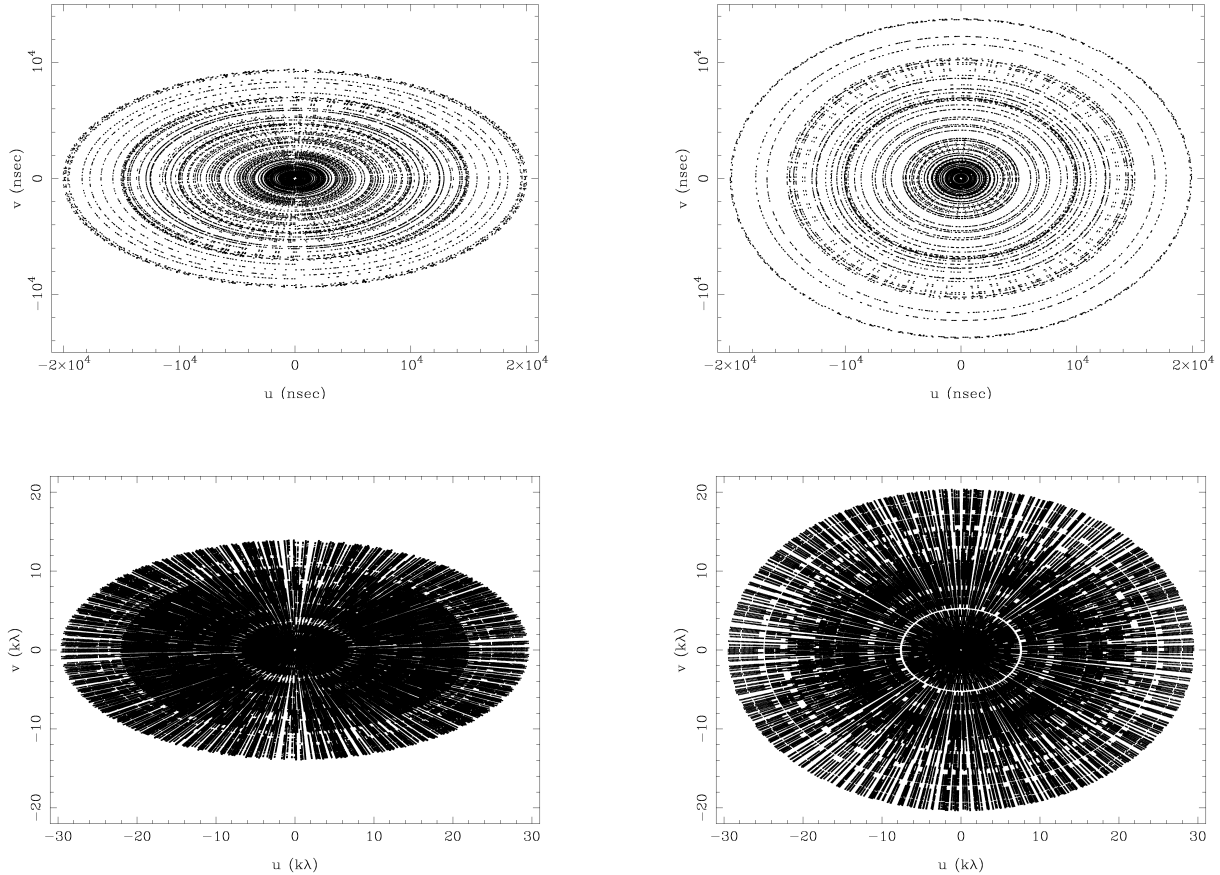


Figure 2. Typical uv -plane coverage for a pointing in each of the CDF-S (left column) and ELAIS-S1 (right column) fields in units of nano-seconds (upper row; independent of frequency) and kilo-lambda (lower row; indicates multi-channel coverage).

Table 2. Observing dates, array configurations, and net integration times on source for the ATLAS DR2 CDF-S field.

Project ID	Date	Array	Net Integration Time (h)
C1035 ...	2002 Apr 4–7, 10, 12–13	6A	72.9
	2002 Aug 23–24, 27–29	6C	29.6
C1241 ...	2004 Jan 7–8, 12	6A	23.9
	2004 Feb 3–5	6B	24.7
	2004 Jun 6, 8–12	750D	37.4
	2004 Nov 24–30	6D	50.4
	2004 Dec 28–30	1.5D	22.6
	2005 Jan 7–8, 18–19, 23	750B	31.9
	2005 Apr 9–10	6A	18.5
	2005 Apr 14	1.5A	8.9
	2005 Apr 22; 2005 May 2	750A	15.0
	2005 Jun 1, 10	EW367	11.7
	2005 Jun 25–26	6B	18.1
	2005 Dec 6	6A	8.7
	2006 Mar 23–24, 27	6C	23.0

ried out as part of the *Spitzer* Wide-Area Infrared Extragalactic Survey (SWIRE; Lonsdale et al. 2003) Legacy Project. We obtained flux densities for SWIRE sources from a pre-release version of the SWIRE Public Data Release² 3 catalogue (SDR3; Fall 2005) in five wavelength bands: 3.6, 4.5, 5.8, and 8.0 μm observed with the Infrared Array Camera (IRAC; Fazio et al. 2004), and 24.0 μm observed with the Multiband Imaging Photometer for *Spitzer* (MIPS; Rieke et al. 2004). The flux density limits for the pre-release SDR3 catalogue in each band were approximately 4, 5, 43, 38, and 230 μJy , respectively. These limits are less conservative than those applied to the general release SDR3 catalogue (Surace et al. 2005)³. SWIRE data is available over 97% and 100% of the ATLAS DR2 CDF-S and ELAIS-S1 survey areas, respectively.

2.2.2 Optical Data

In the optical band, Mao et al. (2012) obtained spectroscopic observations of SWIRE sources associated with ATLAS DR1 radio sources. Spectra were obtained for optical counterparts to 160 SWIRE sources in the CDF-S field, and 306 SWIRE sources in the ELAIS-S1 field, to limiting magnitudes of typically $R \approx 20$, extending to $R \approx 23$ for the faintest sources.

3 DATA REDUCTION AND POST-PROCESSING

We developed a semi-automated analysis pipeline to edit, calibrate, image, and post-process the ATLAS radio data using a combination of the MIRIAD package (Sault, Teuben, & Wright 1995) and custom software, as described in the following sections.

3.1 Flagging and Calibration

We used the MIRIAD task ATLOD to re-weight the spectrum for each visibility in the lag domain in order to reduce the Gibbs

² See <http://irsa.ipac.caltech.edu/data/SPITZER/docs/spitzermission/observingprograms/legacy/swire/>.

³ Also see http://swire.ipac.caltech.edu/swire/astronomers/publications/SWIRE2_doc_083105.pdf.

Table 3. Coordinates of ATLAS DR2 CDF-S calibrators and pointing centres.

Source/Pointing ^a	R.A. (J2000)	Decl. (J2000)
B1934–638	19:39:25.026	-63:42:45.63
B0237–233	2:40:08.175	-23:09:15.73
K2	3:31:42.777	-27:48:30.00
K3	3:32:05.390	-27:57:09.62
K4	3:32:50.610	-27:57:09.62
K5	3:33:13.223	-27:48:30.00
K6	3:32:50.610	-27:39:50.37
K7	3:32:05.390	-27:39:50.37
K8	3:31:19.682	-28:18:41.18
K9	3:34:40.330	-27:44:03.49
K10	3:33:30.909	-27:24:10.98
K11	3:32:08.381	-27:26:51.93
K12	3:30:38.126	-27:30:14.68
1	3:28:47.330	-28:38:37.98
1a	3:27:18.362	-28:38:31.14
2	3:28:03.890	-28:21:46.74
3	3:28:48.482	-28:05:05.58
3a	3:27:18.362	-28:05:05.58
4	3:28:05.258	-27:48:14.34
5	3:28:49.610	-27:31:32.82
5a	3:27:18.362	-27:31:32.82
10	3:30:16.970	-27:31:40.02
11	3:29:32.834	-27:48:22.98
12	3:30:16.298	-28:05:12.42
13	3:29:31.922	-28:21:55.74
14	3:30:15.602	-28:38:44.82
15	3:31:43.874	-28:38:48.42
16	3:30:59.954	-28:22:00.78
27	3:32:27.986	-28:22:02.58
28	3:33:12.122	-28:38:48.42
29	3:34:40.394	-28:38:44.82
30	3:33:56.018	-28:22:00.78
31	3:34:39.698	-28:05:12.42
33	3:34:39.026	-27:31:40.02
41	3:32:28.000	-27:48:30.00
42	3:31:20.166	-27:48:30.00
43	3:31:54.083	-28:01:29.43
44	3:33:01.917	-28:01:29.43
45	3:33:35.834	-27:48:30.00
46	3:33:01.917	-27:35:30.56
47	3:31:54.083	-27:35:30.56

^a The prefix K indicates a pointing from Koekemoer, Mobasher, & Norris (2003) (Project ID C1035).

phenomenon, which can cause ghost images to be reflected about the phase centre for strong sources. The FWHM of the effective spectral resolution resulting from this process was 2.11 channels (Killeen 1996). ATLOD was also used to discard a number of channels including those centred on harmonics of 128 MHz that suffered from self-interference, those located near the edges of each frequency window, and every second channel (which does not result in sensitivity loss because the 4 MHz channels are not independent). The net result is a total of 23×8 MHz channels collectively spanning 1292–1484 MHz, with a gap about the 11th harmonic at 1404–1412 MHz. Given the small amount of correlation between these 8 MHz channels (effective channel widths are 8.44 MHz), in this work we have generally assumed that our channels are statistically independent, with one exception as described in Section 4.2.

For each observational epoch we manually inspected and

flagged the primary calibrator data for radio frequency interference (RFI). We then bandpass-calibrated the secondary calibrator and field data in preparation for automated RFI removal with `PIEFLAG` (Middelberg 2006), which uses baseline-based statistics derived from a reference channel that is checked to be minimally affected by RFI. We carried out rms-based flagging on the calibrator data, and both amplitude and rms-based flagging on the field data. Shadowed antennas were flagged, limiting projected baselines to > 30 m. We then manually inspected the data, removing any residual RFI. On average, $\sim 8\%$ and $\sim 20\%$ of the data were flagged in the 1344 and 1432 MHz frequency windows, respectively. The resulting net integration times for the CDF-S and ELAIS-S1 fields were 397 and 245 hours, respectively. For completeness, we note that both the Moon and the Sun were separated by $> 42^\circ$ from either ATLAS field throughout their observation; separations from calibrators were $> 36^\circ$ for B1934–638, $> 20^\circ$ for B0237–233, and $> 37^\circ$ for B0022–423. Given these large angular separations, we assumed that any influences on our data from the Moon (e.g. as relevant to polarization: Vinyaikin & Krotikov 2007; Zhang et al. 2012) or the Sun were negligible.

`MIRIAD` was used to derive and apply the bandpass, complex gain, complex leakage, and flux density calibrations. Optimised circular polarization calibration was not pursued, limiting on-axis circular polarization leakage to no better than $V/I \sim 0.1\%$ (Rayner 2000). The ATCA’s absolute flux density scale is accurate to within 2% (Reynolds 1994). Parallactic angle coverage was sufficient within all epochs to ensure that leakage solutions could be accurately determined for each antenna. The misalignment⁴ and ellipticity were found to be small (magnitude $\lesssim 8 \times 10^{-3}$) and stable (rms $\lesssim 10^{-3}$) for each antenna over the course of 4 years of ATLAS observing. The data were then split into individual pointings in preparation for both multi-frequency synthesis and per-channel imaging.

3.2 Multi-Frequency Synthesis Imaging

In this section we describe the production of mosaics for the CDF-S and ELAIS-S1 ATLAS DR2 fields in total intensity (Stokes I) and circular polarization (Stokes V), whereby continuum images for each individual pointing were created using multi-frequency synthesis (MFS), deconvolved using `MIRIAD`’s multi-frequency cleaning routine `MFCLEAN`, primary beam corrected, and then linearly mosaicked. We term this the MFS approach in order to differentiate it from the per-channel approach described in Section 3.3. We note that the volume of ATLAS data prevented joint deconvolution of all pointings simultaneously.

We set a common pixel size of $1''$ for all ATLAS DR2 images. This size was limited by the computational capability of `MFCLEAN` to respond to strong sources significantly beyond the primary beam of some pointings. We explored a range of weighting schemes, balancing the trade-off between beam characteristics and sensitivity, selecting superuniform and uniform weighting for the CDF-S and ELAIS-S1 pointings, respectively.

For each pointing we first lightly cleaned the Stokes I image

with `MFCLEAN` to extract model components with surface brightness $\gtrsim 2$ mJy beam $^{-1}$ (higher for pointings containing strong sources). We then used these components to correct for residual phase errors by applying one iteration of phase self-calibration to the data in each of the 1344 and 1432 MHz observing windows, assuming frequency-independent corrections within each window. The self-calibration solution interval was selected to be 3 minutes, allowing for sufficient time to accumulate statistics in relatively faint pointings. Typical rms values for the variations in the resulting phase corrections were found to be 9.5° and 7.0° for pointings in the CDF-S and ELAIS-S1 fields, respectively. Using the corrected phases, the Stokes I data for each pointing were re-imaged and re-cleaned. The Stokes V data were then imaged using the corrected phases; no cleaning was required.

To efficiently clean each Stokes I image we tracked the maximum residual surface brightness, r_{max} , against number of clean iterations, k , which roughly displayed a power law decline. We empirically determined that a robust way to halt the cleaning process (specifically for our ATLAS data) was to stop when the slope flattened off to $\Delta \log_{10}(r_{max})/\Delta k \gtrsim -10^{-4}$ Jy beam $^{-1}$ iteration $^{-1}$. Using this approach in an automated manner (and checking the results manually), we were able to clean deeply enough in each pointing to ensure that sidelobes from strong sources were below the thermal noise, but shallow enough to prevent the cleaning of noise and the development of significant clean bias. Approximately 2500–5000 iterations were performed per Stokes I image, dependent on how many bright sources were visible. We checked the resultant images for clean bias, finding no significant surface brightness attenuation, as discussed further in Section 3.4.

For each pointing, the clean components were convolved with a Gaussian fit to the dirty beam (i.e. the ‘native’ pointing resolution), as calculated by the `MIRIAD` task `RESTOR`, and added to the residuals to produce an image. We did not set a common FWHM for all pointings in the `RESTOR` step because that would have decoupled the resolution of the cleaned sources from the resolution of the noise, rendering any subsequent image analysis statistically compromised. Each Stokes I and V image was then convolved with the task `CONVOL` to a common resolution, chosen to be no better than the worst resolution of all the pointings within each ATLAS field (see also discussion in Section 3.3). The final resolutions of all MFS CDF-S and ELAIS-S1 pointing images were $13''.0 \times 6''.0$ and $9''.6 \times 7''.6$, respectively, each with position angle 0° (North).

A spatial map of rms noise was produced for each pointing image, as described in Section 3.6, from which an average observational rms noise value for each pointing was obtained. The pointings for each respective ATLAS field were then primary beam corrected and linearly mosaicked, weighting each pointing by the inverse of its average observational noise variance. The use of observational noise values, as opposed to predicted theoretical values, enabled us to take into account the decreased sensitivity in pointings containing difficult-to-clean strong sources beyond the primary beam, as well as variations in the degree of data flagging, in order to produce optimally sensitive mosaics. The resulting Stokes I and V mosaics were then regridded from the ATCA’s native north-celestial-pole (NCP) projection into a zenithal equal-area (ZEA) projection (Calabretta & Greisen 2002) in preparation for source extraction. For clarity, we denote these ZEA mosaics I_{MFS} and V_{MFS} , respectively.

Noise properties of I_{MFS} and V_{MFS} are described in Section 3.6. The use of `MFCLEAN` and $1''$ pixels significantly improved image fidelity in the CDF-S field in comparison with DR1, particularly in

⁴ To good approximation, the real part of a leakage term corresponds to feed misalignment (in which the Y feed signal leaks into the X feed), whereas the imaginary part corresponds to feed ellipticity (in which the Y feed has a finite response to the X feed, seen with a phase lag of 90°) (Sault, Killeen, & Kesteven 1991).

reducing sidelobes about a strong ~ 1 Jy source (PKS B0326–288) in the south-west of the field.

3.3 Per-Channel Imaging

In this section we discuss the production of Stokes I , Q , and U mosaics in each of the 23 frequency channels for the two ATLAS fields (20 pointings in ELAIS-S1 and 39 pointings in CDF-S), obtained by imaging, primary beam correcting, and linearly mosaicking a total of $3 \times 23 \times (20 + 39) = 4071$ individual images. We term this the per-channel (PC) approach. As with the MFS approach, the volume of ATLAS data prevented joint deconvolution of all pointings simultaneously in each frequency channel.

The frequency-independent gain solutions from the MFS 1344 and 1432 MHz self-calibration process were applied to the channel data in each respective frequency window for each pointing. We explored a range of suitable weighting schemes, checking that the central core of the dirty beam could be appropriately modelled with a Gaussian⁵. We selected near-natural weighting with a robustness parameter of -0.25 to optimise the dirty beam, applying this weighting scheme to all pointings in both ATLAS fields.

We cleaned the Stokes I , Q , and U images for each pointing with CLEAN⁶, following the procedure outlined in Section 3.2. We note that our cleaning approach avoided the need to set a clean cutoff related to the theoretical noise in each pointing; the theoretical noise could have easily decoupled from the true noise in those pointings in which strong sources were present, or for which significant data-flagging had been carried out. Approximately 1000 iterations were performed per Stokes I image. Approximately 400 iterations were performed per Stokes Q or U image. We checked the resultant images for the effects of clean bias, finding no significant impact, as discussed further in Section 3.4.

For the PC images in each pointing, the clean components were convolved to the pointing's native resolution and added to the residuals. Each image was then convolved to the worst resolution of any other image at any frequency within each respective ATLAS field. These two convolution steps ensured that the final images of all pointings in all channels had the same resolution, taking into account both the differing wavelength and uv -plane coverage (due to RFI flagging) in each channel. The final resolutions of all PC CDF-S and ELAIS-S1 images were $14''.6 \times 5''.4$ and $10''.6 \times 6''.2$, respectively, both with position angle 0° (North). Mosaics of Stokes I , Q , and U in ZEA projection were then produced for each frequency channel for the two ATLAS fields, incorporating the same procedure to weight each constituent image by the inverse of their average observational noise variance as described earlier in Section 3.2. For each of these resultant PC mosaics, which we denote $I_i(x, y)$, $Q_i(x, y)$ and $U_i(x, y)$ for the i 'th channel over spatial pixels (x, y) , we computed a spatial rms noise map, as described in Section 3.6. In subsequent discussion we will typically drop the pixel (x, y) notation, unless required for clarity.

To illustrate the importance of the second convolution step described above, we note that the ratio between native beam volumes for images at either end of the observed frequency range in the

CDF-S was 1.7. Attempting to combine such native images for subsequent analysis (e.g. as required of channel mosaics in Section 3.5) would bias all measurements of integrated surface brightness. The two convolution steps were therefore critical for maintaining statistical control over the final mosaics.

3.4 Clean Bias

Clean bias is a deconvolution effect that redistributes surface brightness from real sources to noise peaks, systematically reducing the observed surface brightness of sources independent of their signal-to-noise ratio (SNR) (Condon et al. 1998). The effect is worse for observations with poor uv -coverage due to increased sidelobe levels. Despite our good uv -coverage, we have checked for clean bias in our MFS and PC data processing to ensure that ATLAS sources have errors dominated by noise and not bias.

We injected 190 point sources with SNRs ranging from 5σ to 100σ at random positions into the uv -data for a representative sample of ATLAS pointings. The data were then imaged and cleaned following both the MFS and PC approaches. For each injected source we compared the peak surface brightness with the input flux density, repeating multiple times to accumulate statistics. We found that our implemented cleaning strategy produced no discernible clean bias; we measured differences between input and output peak surface brightness of $0 \pm 5 \mu\text{Jy beam}^{-1}$ in the MFS Stokes I approach (image rms $\approx 30 \mu\text{Jy beam}^{-1}$) and $0 \pm 35 \mu\text{Jy beam}^{-1}$ in the PC Stokes I approach (image rms per channel $\approx 160 \mu\text{Jy beam}^{-1}$). We found that the number of clean cycles would need to increase by a factor of ~ 10 to induce a clean bias of $\gtrsim 5\%$ for a 5σ source (e.g. see results of DR1 clean bias calculations in Fig. 3 of Middelberg et al. 2008).

To examine the potential effects of clean bias on polarization position angles (e.g. see Battye, Browne, & Jackson 2008), we injected 40 sources with a range of SNRs into a representative sample of PC Stokes Q and U uv -data. For each injected source we specified a linearly polarized flux density and a random position angle. The Stokes Q and U data were then imaged and cleaned per the PC approach, combined in quadrature, and corrected for Ricean bias using the first-order scheme described by Leahy & Fernini (1989). We then compared both the output peak polarized surface brightness and position angle with the input values for each source, repeating the entire test multiple times. We found that neither statistic displayed significant clean bias; we measured differences between input and output peak linearly polarized surface brightness of $0 \pm 30 \mu\text{Jy beam}^{-1}$ (image rms $\approx 120 \mu\text{Jy beam}^{-1}$) and found no discernible tendency for position angles to be oriented toward multiples of 45° . We found that in order to induce discernible clean bias in linear polarization, approximately 50 times more clean cycles than originally implemented were required; an additional factor of 50 times more cycles were required to produce a clear position angle bias.

3.5 Rotation Measure Synthesis

We used rotation measure (RM) synthesis (Brentjens & de Bruyn 2005) and RM clean (Heald, Braun, & Edmonds 2009) to produce a map of linearly polarized emission for each ATLAS field, processing the Stokes $Q_i(x, y)$ and $U_i(x, y)$ mosaics and their associated rms noise maps, $\sigma_{Q,i}(x, y)$ and $\sigma_{U,i}(x, y)$, for all 23 spectral channels. For each spatial pixel, we weighted the spectral data by their combined variance, $\sigma_{Q,U,i}^2(x, y)$, which we calculated according

⁵ Natural weighting tended to produce beams with central plateaus that were non-Gaussian in appearance, due to the prevalence of short uv -spacing data. To approximate such beams with a Gaussian would have been inappropriate, and would have rendered overly complex any subsequent attempts to clean and eventually measure flux densities from the images.

⁶ MIRIAD's implementation of CLEAN takes into account sources with negative surface brightness.

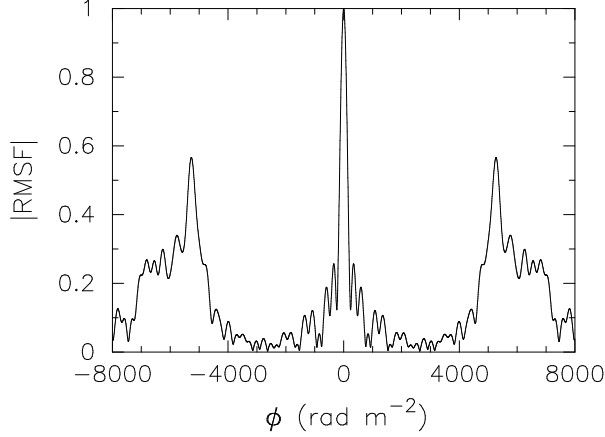


Figure 3. Absolute value of the RMSF versus Faraday depth for a typical spatial pixel in ATLAS, corresponding to the weighted spectral coverage of observations along that sightline. The observed FWHM of the main peak is 293 rad m^{-2} .

to Equations (A2)–(A3) from Hales et al. (2012a); our data are always consistent with $0.8 < \sigma_{Q,i}(x, y)/\sigma_{U,i}(x, y) < 1.2$.

In implementing RM synthesis we sampled the Faraday dispersion function at each spatial pixel, $F(x, y, \phi)$, in steps of 5 rad m^{-2} between Faraday depths $-4000 < \phi < 4000 \text{ rad m}^{-2}$. This range was selected to ensure sensitivity up to the maximum scale afforded by our spectral resolution; $\phi_{\text{max}} \approx \sqrt{3}/\min[\delta(\lambda_i^2)] = 3900 \text{ rad m}^{-2}$, where $\delta(\lambda_i^2)$ is channel width in wavelength-squared space, λ^2 , for the i 'th channel [see Equation (63) from Brentjens & de Bruyn 2005]. A typical rotation measure sampling function (RMSF) for our data is shown in Fig. 3. The main peak has a measured FWHM of $\delta\phi = 293 \text{ rad m}^{-2}$ with sidelobes of order 25% and grating lobes of order 55%. Measured FWHM's for all spatial pixels are $293 \pm 0.2 \text{ rad m}^{-2}$; the spread reflects the slightly different spectral weighting used to process each spatial pixel. For comparison, the theoretical value of $\delta\phi$ obtained by assuming uniform spectral weighting is 265 rad m^{-2} [see Equation (61) from Brentjens & de Bruyn 2005]. Strong grating lobes are present beyond $\pm 5000 \text{ rad m}^{-2}$. Given our spectral coverage, our data are insensitive to Faraday thicknesses greater than $\sim 76 \text{ rad m}^{-2}$ [max-thickness $\approx \pi/\lambda_{\text{min}}^2$, where λ_{min} is the shortest wavelength observed; see Equation (62) from Brentjens & de Bruyn 2005]. Therefore, our Faraday spectra are only sensitive to unresolved RM components.

We did not correct our data for ionospheric Faraday rotation. We note that the ionosphere will typically produce a RM that varies between approximately $+0.2$ and $+1.0 \text{ rad m}^{-2}$ for ATCA observations at zenith and at the array's elevation limit (12°), respectively (Bilitza & Reinisch 2008; Finlay et al. 2010). RM fluctuations about these mean values due to ionospheric density variations are typically $\sim 0.5 \text{ rad m}^{-2}$. Given the FWHM of our RMSF, and to some extent the phase self-calibration applied to the data, we assume that the influence of ionospheric Faraday rotation on both measured RMs and potential depolarization is negligible.

For each ATLAS field we constructed a map of linearly polarized emission, which we denote $L_{\text{RM}}(x, y)$, by applying a 3-point parabolic (3PP) fit to extract the fitted peak polarized surface brightness from within the cleaned Faraday dispersion spectrum for each spatial pixel, $F^{\text{cleaned}}(x, y, \phi)$, namely

$$L_{\text{RM}}(x, y) \equiv 3\text{PP-fit-max} \left[\left| F^{\text{cleaned}}(x, y, \phi) \right| \right]. \quad (1)$$

RM cleaning (Heald, Braun, & Edmonds 2009) was performed

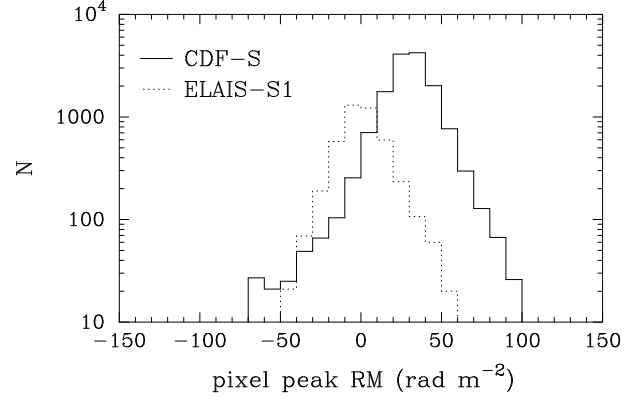


Figure 4. Distribution of RMs for all pixels with $L_{\text{RM}}(x, y)/\sigma_{\text{RM}}(x, y) \geq 7$. This ratio (which is not used elsewhere in this work) is chosen to be higher than the source detection threshold defined in Section 5.1 so as to avoid most contamination by spurious high-RM pixels associated with obvious image artefacts. The higher pixel count and increased width of the CDF-S distribution relative to the ELAIS-S1 distribution is due to the increased presence of strong artefacts in the CDF-S field, such as those about the 1 Jy source PKS B0326–288. Note that the y-axis is logarithmic.

down to a level of $4.4\sigma_{\text{RM}}(x, y)$ [Gaussian equivalent SNR of 4σ ; see Equation (15) from Hales et al. 2012a], where $\sigma_{\text{RM}}(x, y)$ is the rms noise at each spatial pixel in $L_{\text{RM}}(x, y)$. $\sigma_{\text{RM}}(x, y)$ was calculated by combining $\sigma_{Q,i}(x, y)$ and $\sigma_{U,i}(x, y)$ from each spectral channel according to Equations (20)–(23) from Hales et al. (2012a). Properties of $\sigma_{\text{RM}}(x, y)$ for each ATLAS field are presented in Section 3.6. We note that for each pixel, $L_{\text{RM}}(x, y)$ was sampled from $M \equiv 2\phi_{\text{max}}/\delta\phi \approx 28$ independent measurements. The non-Gaussian statistics exhibited by $L_{\text{RM}}(x, y)$, taking into account the value of M , are discussed by Hales et al. (2012a).

We chose to represent the polarized emission at each pixel by Equation (1) for two key reasons. First, our data are insensitive to resolved sources in Faraday depth space, enabling us to represent integrated measurements of surface brightness per unit ϕ by peak measurements of surface brightness per unit ϕ for any Faraday component. Second, we do not expect to find many polarized sources with multiple Faraday components that are separated in Faraday space by more than the FWHM of our RMSF. For example, Farnsworth, Rudnick, & Brown (2011) found that less than $\sim 7\%$ of polarized 1.4 GHz sources consisted of multiple RM components separated by more than $\sim 280 \text{ rad m}^{-2}$, when observed with high resolution in Faraday depth space. We therefore assumed that, even in cases where multiple Faraday components may be present within the width of one RMSF, the total polarized emission in Faraday space for our data could be approximated by the dominant peak. Examination of $F^{\text{cleaned}}(x, y, \phi)$ for our data revealed this to be a suitable approximation (no lines of sight with multiple RM components were detected), though we note that we did not attempt to compare the widths of Faraday components with the width of the RMSF.

Typical RMs for all significant pixels in the CDF-S and ELAIS-S1 polarization images were found to be $\lesssim 70 \text{ rad m}^{-2}$ in magnitude, as indicated in Fig. 4. Detailed analysis of the RM

⁷ For this comparison we neglect components from Farnsworth, Rudnick, & Brown (2011) with $\text{SNR} < 6$ because the statistical significance of such polarization detections drop below the Gaussian equivalent of 5σ ; see Hales et al. (2012a) with $M \approx 70$ as relevant to their data.

properties of ATLAS sources is beyond the scope of this work and will be presented in a future ATLAS data release.

We examined the data for RM clean bias (i.e. the Faraday space analogue of clean bias described in Section 3.4) by manually inspecting the locations of RM clean components. Qualitatively, we did not find any misplaced components for the vast majority of spatial pixels, indicating negligible RM clean bias. We note that clean bias due to grating lobes could only be produced by sources with $|\text{RM}| > 1000 \text{ rad m}^{-2}$; no such sources were found in our data.

In parallel with RM synthesis, we also assembled a channel-averaged Stokes I mosaic, denoted by I_{CA} , to be used for correcting the L_{RM} mosaics for spurious instrumental polarized emission (see Section 5.1). The I_{CA} mosaic was formed by stacking the PC Stokes I mosaics, $I_i(x, y)$, with weighting factors identical to those used to form $L_{\text{RM}}(x, y)$, namely

$$I_{\text{CA}}(x, y) = \left[\sum_{i=1}^{23} I_i(x, y) / \sigma_{Q,U,i}^2(x, y) \right] \left[\sum_{i=1}^{23} 1 / \sigma_{Q,U,i}^2(x, y) \right]^{-1}. \quad (2)$$

Noise properties of the I_{CA} mosaic are described in Section 3.6. We do not use the I_{CA} mosaics for radio component extraction, even though they contain regions with rms noise levels less than those in the I_{MFS} mosaics, because they contain disruptive sidelobes from strong sources interspaced between the optimal low noise regions.

3.6 Noise Distribution in Images

We used the SExtractor package (v. 2.5.0; Bertin & Arnouts 1996; Holwerda 2005) to map spatial variations in rms noise across all channel, pointing, and mosaicked images of Stokes I , Q , U , and V . As outlined in Section 3.5, maps of σ_{RM} for our L_{RM} mosaics were produced by combining $\sigma_{Q,i}$ and $\sigma_{U,i}$ for each spectral channel following the equations presented by Hales et al. (2012a).

SExtractor calculates the rms noise at each spatial pixel in an image by analysing the distribution of pixel values within a local background mesh, taking into account not only local variations in image sensitivity, but also the possible presence of DC offsets due to artefacts (e.g. sidelobes). Following Equation (3) from Hales et al. (2012b), we set the mesh size for each image analysed to the area enclosed by $N_b = 150$ independent resolution elements. Uncertainties in our estimates of local rms noise are therefore $\{[1 + 0.75/(N_b - 1)]^2 [1 - 1/N_b] - 1\}^{0.5} = 6\%$ (using an approximation to the variance of the standard error estimator, suitable for $N_b > 10$; p. 63, Johnson & Kotz 1970).

In Fig. 5 we display rms noise maps for each of the mosaics used to detect and catalogue radio components, namely I_{MFS} , V_{MFS} , and L_{RM} ; these noise maps are used in Section 5.1 to evaluate local SNRs at any spatial location. In Fig. 6 we present cumulative histograms of the rms noise distributions exhibited by each of these mosaics; for completeness, we also include the noise distributions from the I_{CA} mosaics. The linear polarization mosaics are both more sensitive, and more uniform in their sensitivity, than the total intensity images because there are fewer sources and fewer imaging artefacts in the former.

4 INSTRUMENTAL EFFECTS

In this section we describe three systematic effects – time-average smearing, bandwidth smearing, and instrumental polarization – and our methods to model their wide-field behaviours across the ATLAS mosaics. Consideration of 3D-smearing (Perley 1999) is

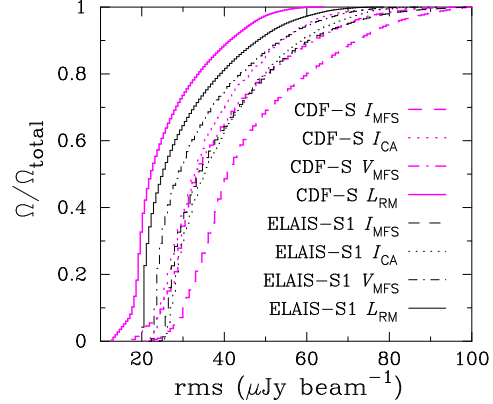


Figure 6. Fraction of sky area in ATLAS survey areas at or below a given rms noise level (calculated from Fig. 5).

not required because the ATCA is a coplanar array. We conclude this section by defining the survey area boundary for each ATLAS field.

4.1 Time-Average Smearing

Time-average smearing is the well-known effect whereby visibilities are smeared in the uv -plane due to the rotation of the sky during a correlator cycle time. The result is a decrement in the observed peak surface brightness of sources; integrated surface brightnesses are conserved.

For our correlator cycle time of 10 seconds, we used the theoretical assumptions from Bridle & Schwab (1999) to estimate a loss in peak flux density of no worse than 1.5% at the edges of individual pointing images. Consequently, we did not correct for the marginal degree of time-average smearing in our data.

4.2 Bandwidth Smearing

Bandwidth smearing, or chromatic aberration, is the well-known effect whereby visibilities are smeared in the uv -plane due to the finite bandwidth of receiver channels. The result is a decrement in the observed peak surface brightness of sources; this is accompanied by source broadening in a radial direction from the pointing phase centre, such that integrated surface brightnesses remain conserved. The bandwidth smearing effect is proportional to the radial offset from the phase centre in units of projected synthesised beamwidths, and to the fractional bandwidth $\Delta\nu_{\text{eff}}/\nu$, where ν is the reference frequency for setting delay terms when gridding in the uv -plane and $\Delta\nu_{\text{eff}}$ is the effective passband width. In the following we present our prescription for handling bandwidth smearing from a non-circular beam. While this prescription is trivial, we are unaware of any previous studies that have accounted for non-circular beams.

For a source at position angle ζ East of North with respect to the phase centre, the projected beam FWHM for an elliptical beam with major axis FWHM B_{maj} , minor axis FWHM B_{min} , and position angle ψ East of North is given by

$$B_{\text{proj}}(\zeta) = \frac{B_{\text{maj}} B_{\text{min}}}{\sqrt{[B_{\text{maj}} \sin(\zeta - \psi)]^2 + [B_{\text{min}} \cos(\zeta - \psi)]^2}}. \quad (3)$$

Assuming a Gaussian beam and rectangular passband, the bandwidth smearing effect for an individual pointing is then given by

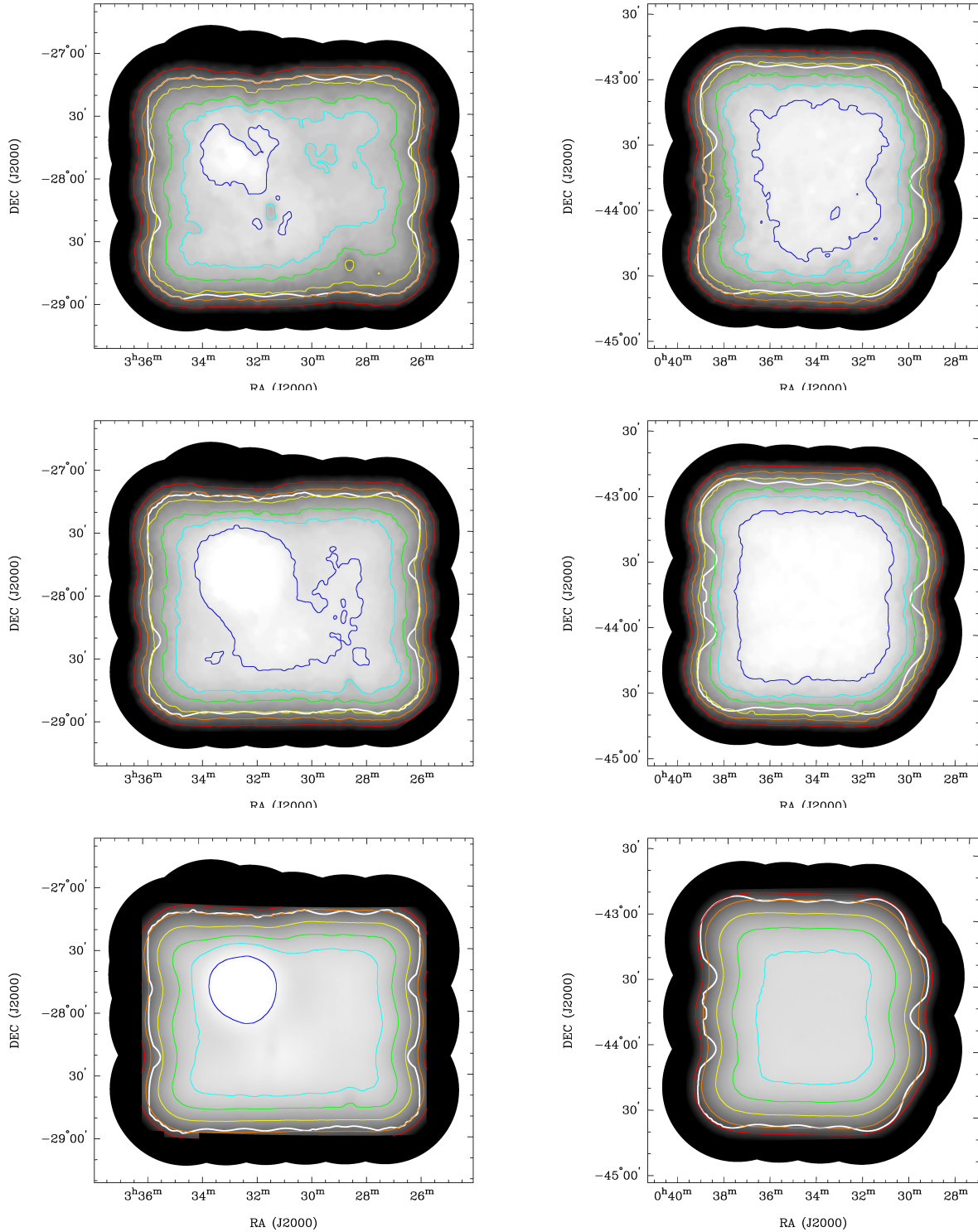


Figure 5. Spatial rms noise maps of the CDF-S (left column) and ELAIS-S1 (right column) fields for total intensity (I_{MFS} ; top row), circular polarization (V_{MFS} ; middle row) and linear polarization (L_{RM} ; bottom row). Shading levels are scaled equally between panels in each row; only the top two rows are shaded equally. Thin contours in the upper and middle panels indicate rms levels of 30, 40, 50, 75, 100, and 150 $\mu\text{Jy beam}^{-1}$, as calculated by SExtractor. Thin contours in the lower panels indicate rms levels of 17 (CDF-S panel only), 22, 27, 37, 57, and 77 (ELAIS-S1 panel only) $\mu\text{Jy beam}^{-1}$, as calculated using a combination of SExtractor and Equations (20)–(23) from Hales et al. (2012a). The bold white contours, co-located within the panels in each column, indicate the survey area boundaries (see Section 4.4).

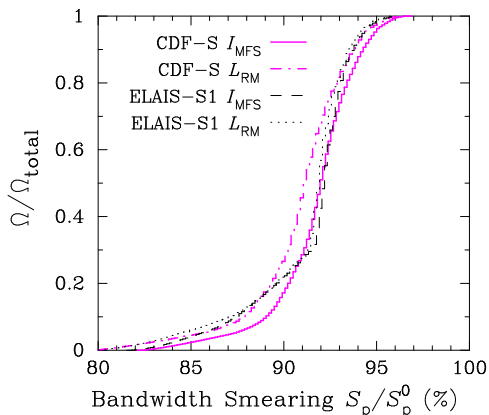


Figure 8. Fraction of sky area in ATLAS survey areas at or below a given bandwidth smearing level (calculated from Fig. 7).

(Condon et al. 1998)

$$\frac{S_{\text{peak}}}{S_{\text{peak}}^0} = \left\{ 1 + \frac{2 \ln 2}{3} \left[\frac{\Delta \nu_{\text{eff}}}{\nu} \frac{d}{B_{\text{proj}}(\zeta)} \right]^2 \right\}^{-\frac{1}{2}}, \quad (4)$$

where the ratio $S_{\text{peak}}/S_{\text{peak}}^0$ represents the peak surface brightness attenuation (smearing) for a source at radial distance d from the phase centre with respect to an unsmeared source at $d = 0$.

To model the amount of bandwidth smearing at any spatial position within the I_{MFS} mosaic for each ATLAS field, we first used Equation (4) with $\Delta \nu_{\text{eff}} = 8.44$ MHz (rather than the nominal 8 MHz; see Section 3.1) and $\nu = 1.387$ GHz to produce simulated images quantifying the smearing exhibited over individual pointings. We then mosaicked these simulated images together using the same weighting factors that were used to construct the I_{MFS} mosaics. We followed a similar procedure to model bandwidth smearing within the L_{RM} mosaics. First, we modelled the smearing effect within all Stokes Q and U images for each pointing and channel, using $\Delta \nu_{\text{eff}} = 8.44$ MHz and setting ν to each channel’s respective frequency. We then mosaicked all simulated pointing images for each channel together to produce simulated bandwidth smearing channel mosaics, using the same weighting factors that were applied to construct the PC Stokes Q_i and U_i mosaics. Next, we combined the Stokes Q and U mosaics of simulated bandwidth smearing together within each channel, weighting each mosaic by the same factors applied to construct $\sigma_{Q,U,i}$ (see Section 3.5). Finally, we stacked these combined channel mosaics together, weighting each channel by $\sigma_{Q,U,i}$ in the same way that L_{RM} was constructed (see Section 3.5). The resulting mosaics, which map the bandwidth smearing ratio $\varpi(x, y) \equiv S_{\text{peak}}(x, y)/S_{\text{peak}}^0$ over all spatial positions within the CDF-S and ELAIS-S1 I_{MFS} and L_{RM} mosaics, are presented in Fig. 7. In Fig. 8 we present cumulative histograms of the bandwidth smearing distributions from Fig. 7. Bandwidth smearing maps were not required for V_{MFS} (see Section 5.1).

We checked the accuracy of our individual pointing and combined mosaic bandwidth smearing solutions by following the procedure outlined by Prandoni et al. (2000). We measured peak and integrated surface brightnesses for a series of strong point sources visible in multiple overlapping pointings, noting offsets from their respective pointing centres. We found good agreement between observed and predicted decrements in peak surface brightness, verifying our modelled solutions.

The bandwidth smearing ratio ϖ is typically greater than 90% over the ATLAS mosaics, as indicated in Fig. 7 and Fig. 8. Un-

like for an individual pointing, bandwidth smearing in a mosaic is not negligible, even at locations situated over pointing centres. This is because many adjacent pointings overlap and contribute to the smearing at any position. Locations that experience the maximum ratio between contributing numbers of on- and off-axis pointings will experience minimal bandwidth smearing in a mosaic. For example, note the lessened smearing over the corner pointings in Fig. 7. Note also the lessened smearing over the GOODS-South region (refer to Fig. 1) in the CDF-S panels of Fig. 7, where pointings are spaced more tightly than elsewhere, in turn reducing the relative impact of adjacent off-axis pointings.

4.3 Instrumental Polarization

To model spurious polarized emission over the L_{RM} mosaics, caused by leakages of Stokes I into Stokes Q and U (Sault, Killeen, & Kesteven 1991; Cotton 1999) within individual channels for each pointing, we needed to account for two forms of instrumental polarization. The first was an ‘absolute’ contribution that was position-independent, applying uniformly over the full field of view for each pointing, while the second was a ‘relative’ contribution that was position-dependent. To estimate the former, we considered gain errors resulting from our standard complex leakage calibrations (see Section 3.1), which nominally corrected the raw ATLAS data for couplings between linear-feed outputs for each antenna. By assuming that the 10^{-3} variability exhibited by these calibration solutions represented an absolute level of instrumental polarization across each pointing, we estimated that the position-independent leakages from Stokes I to Stokes Q or U in each channel were $\sim 10^{-3}/\sqrt{2} = 0.07\%$.

Position-dependent leakages are caused by a number of telescope design properties, the most dominant of which are reflector geometry and aperture blockage by feed support struts. Because ATCA antennas are alt-az mounted, the instrumental polarization response rotates with parallactic angle against the field of view throughout an observation. A model of the ATCA’s off-axis polarization response (neglecting complicated antenna deformations, for example due to pointing elevation or wind-speed) has been included in the MIRIAD package (see also Sault 1995). In principle, the ATCA’s primary beam polarization response may be corrected by using the MIRIAD task OFFAXIS, which removes rotated instrumental leakages from visibility data as a function of time. However, we were unable to verify the performance of this task, which predicted unrealistic leakage corrections for strong Stokes I sources within the ATLAS fields.

Instead, we used the (less complicated) task OFFPOL to simulate images of the instrumental response exhibited by Stokes Q and U for each pointing in each channel of each ATLAS field. These images quantified the position-dependent fractions of Stokes I surface brightness leaked into Stokes Q and U over the course of full synthesis observations, relative to the absolute leakage level described above. The leakages exhibited at the phase centres for each of these simulated images were zero. To account for the missing absolute levels of instrumental polarization, we added 0.07% in quadrature to each Stokes Q and U leakage image. We then mosaicked all pointing images for each channel together to produce channel mosaics, using the same weighting factors that were applied to construct the PC Stokes Q_i and U_i mosaics. Next, for each channel we combined the Stokes Q and U leakage mosaics together in quadrature, weighting each mosaic by the same factors applied to construct $\sigma_{Q,U,i}$ (see Section 3.5). Finally, we stacked these combined leakage mosaics together, using the same weighting scheme as ap-

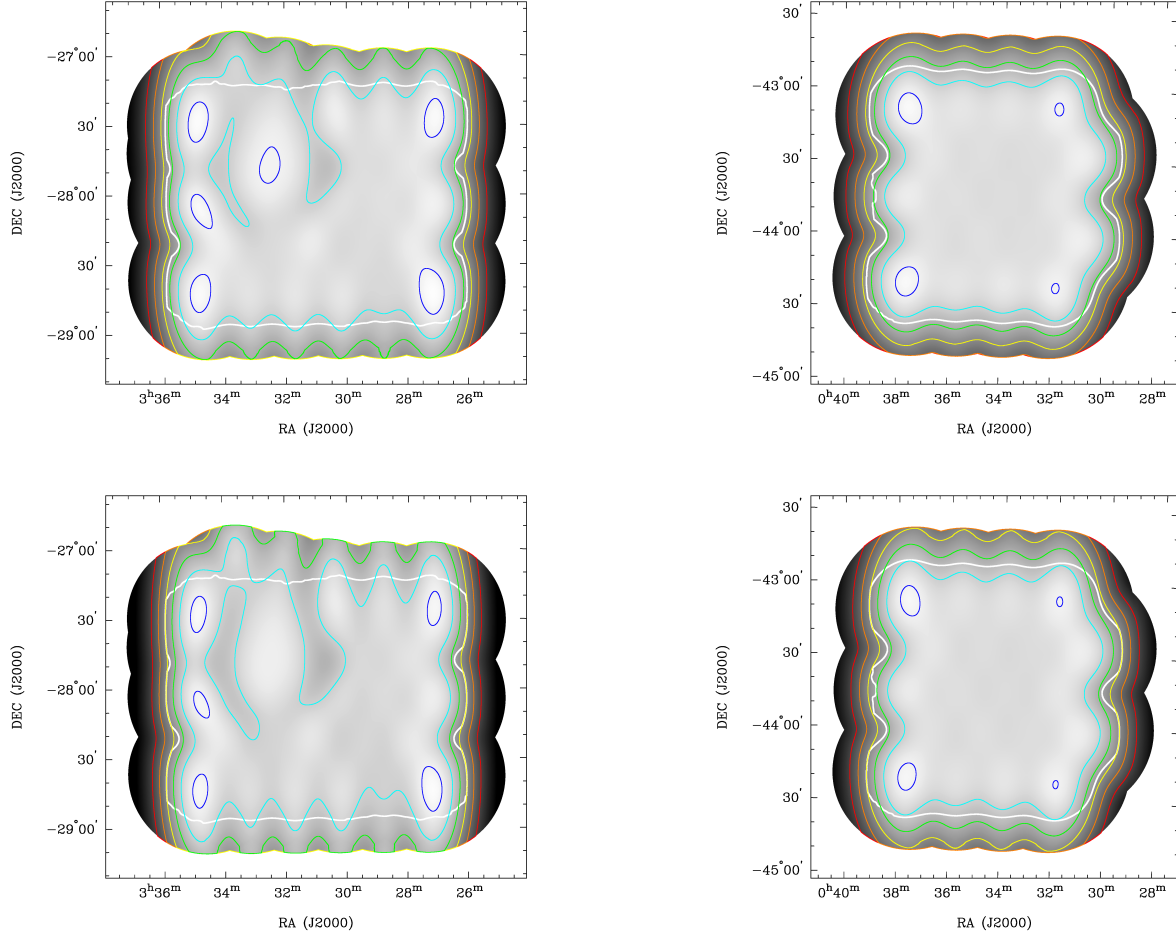


Figure 7. Top: Spatial bandwidth smearing maps of the CDF-S (left column) and ELAIS-S1 (right column) fields for total intensity (I_{MFS} ; top row) and linear polarization (L_{RM} ; bottom row). Shading levels are identical in each panel. The thin contours indicate peak surface brightness attenuation levels (ϖ ; see Section 4.2) of 70% (outermost), 75%, 80%, 85%, 90%, and 95% (innermost). The bold white contours, co-located within the upper and lower panels in each column, indicate the survey area boundaries (see Section 4.4).

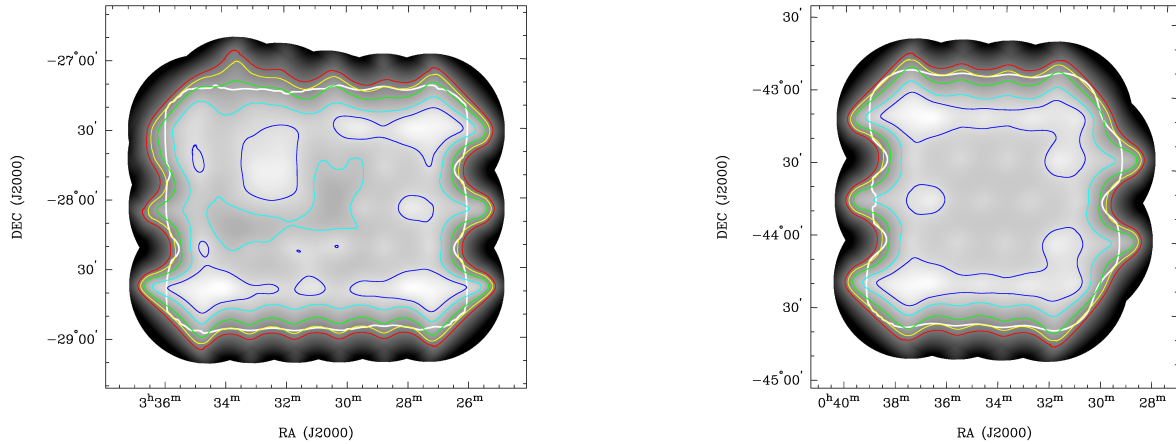


Figure 9. Spatial maps of K_{LEAK} , indicating the fraction of Stokes I surface brightness that may leak and appear as spurious polarized emission within the CDF-S (left) and ELAIS-S1 (right) linear polarization fields, due to instrumental artefacts. Contours indicate leakage levels of 0.3% (innermost), 0.4%, 0.6%, 0.8%, and 1.0% (outermost). The bold white contours indicate the survey area boundaries (see Section 4.4).

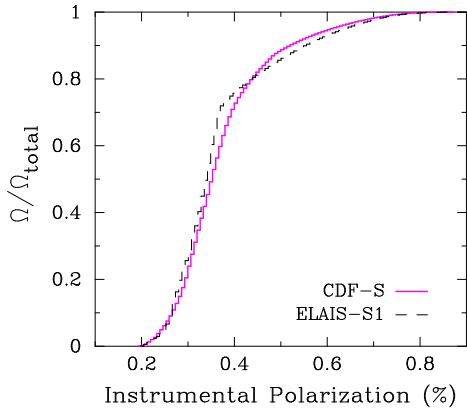


Figure 10. Fraction of sky area in ATLAS linear polarization survey areas (L_{RM}) at or below a given instrumental polarization leakage level (calculated from Fig. 9).

plied to L_{RM} and I_{CA} (see Section 3.5), resulting in what we term the K_{LEAK} mosaics. These mosaics, which map the fraction of Stokes I surface brightness that may appear as spurious linearly polarized emission at any spatial position within the CDF-S and ELAIS-S1 L_{RM} mosaics, are presented in Fig. 9. In Fig. 10 we present cumulative histograms of the instrumental leakage distributions from Fig. 9. Both figures indicate that instrumental polarization is almost always less than 0.8% over the ATLAS mosaics, though never smaller than 0.2%. As with bandwidth smearing (Section 4.2), polarization leakage levels are found to be diminished within the edge pointings of Fig. 9.

We checked the accuracy of our individual pointing and combined mosaic instrumental polarization solutions by attempting to detect spurious polarized emission from strong unpolarized sources that were visible in multiple overlapping pointings. We found good agreement between our predictions and the observed detections or upper bounds, verifying our modelled solutions.

The leakage correction scheme described above is rudimentary and only formally valid for polarized sources with rotation measures near 0 rad m^{-2} . This is because polarization leakage is not expected to vary with λ^2 . We justify our use of the scheme above to model polarization leakage in ATLAS sources at any RM by noting that typical ATLAS RMs are $\lesssim 70 \text{ rad m}^{-2}$ in magnitude, while the FWHM of the RMSF is 293 rad m^{-2} (see Section 3.5). Thus leakage near 0 rad m^{-2} will contaminate all polarized ATLAS sources. Furthermore, as will be described below, the magnitude of the polarization leakage corrections for ATLAS sources are small, particularly for faint sources which are of principal interest in this study. Any systematic overcorrection for leakage in ATLAS sources with $|\text{RM}| > 0 \text{ rad m}^{-2}$ is likely to be negligible.

In preparation for image analysis, we produced corrected maps of linearly polarized intensity for each ATLAS field, which we denote by $L_{\text{RM}}^{\text{CORR}}$, by performing a scalar correction at each spatial pixel,

$$L_{\text{RM}}^{\text{CORR}}(x, y) = L_{\text{RM}}(x, y) - I_{\text{CA}}(x, y) K_{\text{LEAK}}(x, y), \quad (5)$$

with I_{CA} from Section 3.5. We used I_{CA} rather than I_{MFS} in Equation (5) because the former was produced in an equivalent manner to L_{RM} and K_{LEAK} , thus suitably reflecting the effective Stokes I surface brightness that may have leaked into L_{RM} . We note that the noise properties of L_{RM} (as described by Hales et al. 2012a) render Equation (5) an approximation for removing underlying levels of spurious emission. However, we estimate that any systematic er-

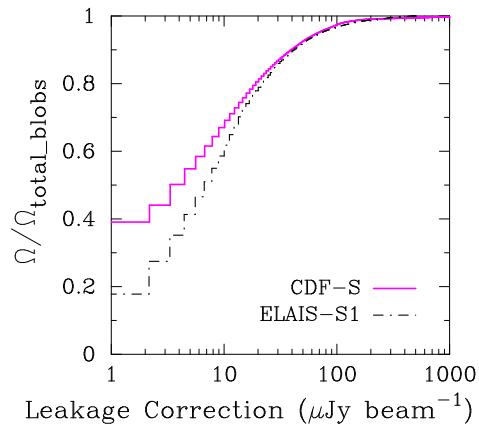


Figure 11. Fraction of polarized blob pixels within each ATLAS field at or below a given surface brightness correction for spurious instrumental polarized emission; namely $L_{\text{RM}} - L_{\text{RM}}^{\text{CORR}}$ for pixels agglomerated within linearly polarized blobs, not including field pixels.

rors resulting from the use of Equation (5) are small, and that they are accounted for by the conservative absolute calibration error set for our analysis in Section 5.1.

To evaluate the impact of using Equation (5) on the data, we extracted all pixels exhibiting significant polarized emission from $L_{\text{RM}}^{\text{CORR}}$ (blob extraction is described in Section 5.1), and compared their brightnesses with their uncorrected values from L_{RM} . In Fig. 11 we plot the difference between uncorrected and corrected pixel brightness values. Fig. 11 indicates that the surface brightness corrections for $> 80\%$ of blob pixels were smaller than the typical $\sim 25 \mu\text{Jy beam}^{-1}$ rms noise levels in the polarization mosaics. Less than 5% of corrections were greater than $100 \mu\text{Jy beam}^{-1}$; these were associated with the small number of strong $\sim \text{Jy}$ total intensity components in the ATLAS fields.

4.4 Survey Area Boundaries

We defined survey area boundaries for the CDF-S and ELAIS-S1 fields by enforcing that the following conditions were met within both the I_{MFS} and L_{RM} mosaics: rms noise $\leq 100 \mu\text{Jy beam}^{-1}$, bandwidth smearing $\varpi \geq 80\%$, instrumental polarization leakage $\leq 1\%$, and mosaicked primary beam response $\geq 40\%$. The resultant survey areas for the CDF-S and ELAIS-S1 fields, which we denote F^{AREA} , were 3.626 deg^2 and 2.766 deg^2 , respectively. These areas were largely constrained by the bandwidth smearing condition within the L_{RM} mosaics; see the lower panels in Fig. 7. We note that less than 0.3 spurious 5σ detections are expected by chance over the survey area for the CDF-S I_{MFS} mosaic [using Equation (3) from Hales et al. 2012b]; even fewer are expected over the other mosaics.

5 RADIO COMPONENT EXTRACTION

In the following sections we describe how radio components were detected and extracted from the ATLAS total intensity and polarization mosaics, taking into account the instrumental systematics described in Section 4, how unresolved and resolved components were identified and assigned flux densities given by their peak or integrated surface brightness measurements, respectively, and how

flux densities in both total intensity and linear polarization were debiased to account for noise-induced systematics. We use the term *component* to refer to an isolated region of emission that is best described by a single 2D elliptical Gaussian. Blended regions of contiguous emission may consist of multiple individual components. Following the terminology from Hales et al. (2012b), a *blob* is an agglomerated island of pixels above a SNR cutoff, which may encapsulate a single component or a blended region of emission. In Section 6 we use the term *source* to refer to single or multiple components belonging to the same astronomical object.

5.1 BLOBCAT and Follow-Up Fitting

Radio component detection and extraction were performed independently in total intensity and linear polarization using a combination of two packages. First, the BLOBCAT package (Hales et al. 2012b) was used to detect and catalogue blobs in these images, flagging all blobs likely to consist of multiple blended components for follow-up and assuming that the remainder represented individual components. For total intensity images, the MIRIAD task IMFIT was then used to decompose the flagged blobs into individual components. For linear polarization images, a combination of BLOBCAT and IMFIT was used to decompose blobs into individual components. As ATLAS DR2 is the first survey to make use of BLOBCAT, we now describe these procedures in some detail.

BLOBCAT exhibits accurate measurement performance in both total intensity and linear polarization (see Hales et al. 2012b). The software enables rms noise maps and bandwidth smearing maps to be included within the blob detection and cataloguing procedure. However, no capabilities are provided within BLOBCAT to handle instrumental polarization maps. We therefore removed spurious instrumental polarized emission from our L_{RM} mosaics prior to analysis with BLOBCAT using Equation (5).

We ran BLOBCAT over the defined survey areas within the I_{MFS} and $L_{\text{RM}}^{\text{CORR}}$ mosaics and their respective rms noise and bandwidth smearing maps for each ATLAS field. We set the SNR detection thresholds to 5σ in total intensity and $6.25\sigma_{\text{RM}}$ in linear polarization. The latter is equivalent to a statistical significance (Type-I error) of $\alpha = 10^{-7}$, or a standard Gaussian detection threshold of $\pm 5.33\sigma$; see Equation (30) from Hales et al. (2012a) with $M = 28$. We do not consider the effects of uncertainties associated with these detection thresholds, which are $\sim 0.4\sigma$ due to uncertainties in our estimates of rms noise (see Section 3.6). To ensure realistic errors were calculated for the catalogue entries, we specified a number of input arguments to BLOBCAT; see Hales et al. (2012b) for full error propagation details. We specified absolute positional uncertainties of $0''.01$ in both R.A. and Decl. for the phase calibrators⁸ PKS B0237–233 and PKS B0022–423 for the CDF-S and ELAIS-S1 fields, respectively. We characterised the relative positional uncertainties between the ATLAS mosaics and the assumed positions of the phase calibrators by specifying typical values for the standard error of the mean (SEM) of the phase variations resulting from the self-calibration step described in Section 3.2. In Section 5.2 we describe how the SEM values were calculated from the observed self-calibration rms phase variations given in Section 3.2. We set the absolute flux density error conservatively to 5%, taking into account 2% error in the ATCA’s absolute flux density scale (Reynolds 1994) and other sources of uncertainty such as time-average smearing, uncertainties in modelled instrumental system-

atics, and unflagged RFI. We set the input argument for pixellation error, which encapsulates uncertainties in peak surface brightness measurements due to image pixellation, to 1% for each mosaic. We set the clean bias correction parameter to zero for each mosaic.

For each blob we retained a subset of entries from BLOBCAT’s full output catalogue (see Section 2.6 from Hales et al. 2012b). We have used these entries to construct the ATLAS DR2 component catalogue presented in Appendix A. The retained items for each blob were their identification number, number of agglomerated pixels n_{pix} , weighted centroid position and associated errors, detection SNR A_s , local rms noise value σ_s , local bandwidth smearing value ϖ , peak surface brightness corrected for bandwidth smearing S_{peak} and associated error $\sigma_{S_{\text{peak}}}$, integrated surface brightness S_{int} and associated error $\sigma_{S_{\text{int}}}$, estimated size in units of sky area covered by an unresolved component with the same peak surface brightness R^{EST} , and fraction of survey area (or visibility area) over which the blob could have been detected due to rms noise and bandwidth smearing fluctuations V^{AREA} . BLOBCAT does not account for polarization bias in its measurements of peak polarized surface brightness. BLOBCAT’s integrated polarized surface brightnesses are unaffected by polarization bias (see Hales et al. 2012b). In Section 5.4 we account for biases in measurements of S_{peak} due to noise boosting in total intensity, and a combination of boosting and polarization bias in linear polarization.

We manually inspected all blobs identified near regions of strong total intensity emission⁹ within both the I_{MFS} and $L_{\text{RM}}^{\text{CORR}}$ mosaics. We identified ~ 30 total intensity blobs in each ATLAS field that were clearly associated with image artefacts, and removed these from the catalogue. We also removed ~ 10 linearly polarized blobs in each ATLAS field that did not exhibit total intensity counterparts; these were unlikely to be signs of Galactic foreground emission as the ATLAS fields are located more than 50° below the Galactic plane. To identify blobs likely to consist of multiple components, we flagged all catalogue entries with $R^{\text{EST}} \geq 1.4$ and $n_{\text{pix}} \geq 500$. We selected these values following manual testing to identify the most suitable criteria for conservative automatic identification of blended-component blobs. We note that the $R^{\text{EST}} \geq 1.4$ criterion is likely to be suitable for BLOBCAT analyses in general, whereas the $n_{\text{pix}} \geq 500$ criteria depends on the relationship between image resolution and pixel size (this ratio is ~ 10 for ATLAS DR2 images). We attempted to fit multiple Gaussian components to each of the total intensity flagged blobs using IMFIT. For each blob, we first identified positions at which up to 6 individual Gaussian components could be situated. We then ran IMFIT with these initial conditions and inspected the output fits and fitting residuals. Catalogue entries for each flagged blob were replaced by entries for each IMFIT component identified; component identification numbers were assigned by suffixing Cj to the original blob number for each j ’th component extracted. No more than 6 components were required for any individual blob; often, only 2 components were required. Components with $\text{SNR} < 5\sigma$ were excluded from the catalogue. For blobs best fit by a single Gaussian component, their original BLOBCAT catalogue entries were retained, unless image artefacts such as sidelobe ridge-lines were seen to be affecting them. We followed the same general procedure

⁹ The noise estimation algorithm described in Section 3.6 performs sub-optimally in regions where the rms noise changes rapidly over spatial scales much smaller than the mesh size. In the few such regions of the ATLAS images, we carefully inspected the data to account for potentially underestimated rms noise values and in turn overestimated detection significances.

⁸ <http://www.vla.nrao.edu/astro/calib/manual/index.shtml>

to decompose flagged blobs in linear polarization, with some minor differences. We applied a $4\sigma_{\text{RM}}$ cutoff threshold for fitting linearly polarized components with `IMFIT`, to prevent polarization non-Gaussianities from interfering with `IMFIT`'s least-squares fitting algorithm; all fits and fitting residuals were carefully inspected for biases. Some of the flagged polarized blobs were found to consist of isolated components that were joined by a small bridge of low-SNR emission. For these blobs, we used `BLOBCAT`, rather than `IMFIT`, to fit each clearly-separated component; image masking was applied to isolate the emission from each individual component prior to refitting. Identification numbers were assigned to each extracted component by suffixing Cj or Fj to the original blob number for fits obtained with `IMFIT` or `BLOBCAT`, respectively. All refit polarized components with $\text{SNR} < 6.25\sigma_{\text{RM}}$ were excluded from the catalogue.

All `IMFIT` measurements of total intensity and linear polarization were carefully compared with their original `BLOBCAT` measurements for consistency. We are confident that no systematic differences are present between the two samples, taking into account the different regimes where the two extraction methods are known to become inaccurate; see Hales et al. (2012b) for a formal comparison between `BLOBCAT` and `IMFIT`. A total of 1268 (113) and 1148 (59) components were extracted in total intensity and linear polarization, the latter in parentheses, within the CDF-S and ELAIS-S1 survey areas, respectively. Of these, 244 (6) and 373 (5) were extracted using `IMFIT`, while (18) and (7) were extracted following image masking using `BLOBCAT`, respectively.

Finally, we ran `BLOBCAT` over the survey areas within the CDF-S and ELAIS-S1 V_{MFS} mosaics and their associated rms noise maps, searching for blobs with positive or negative surface brightness. All ~ 20 circularly polarized blobs identified in each field were consistent with likely instrumental leakage from I_{CA} to V_{MFS} at or below the 0.5% level.

5.2 Image Frame Position Errors

Formal position errors for each blob were calculated by combining three errors as described in Hales et al. (2012b): the absolute uncertainties defined in Section 5.1, the positional uncertainties of the image frames about the assumed locations of the secondary calibrators, and the measurement errors from `BLOBCAT` or `IMFIT`. In this section we describe the calculation of SEM values for each ATLAS field, which are needed to calculate the image frame errors.

In Section 3.2, typical rms values for the variation in the phase corrections resulting from self-calibration were found to be 9.5° and 7.0° for pointings in the CDF-S and ELAIS-S1 fields, respectively. If the samples used to calculate these rms values were uncorrelated, then the SEM for each field could be calculated by dividing the rms values by the square root of the number of self-calibration intervals. However, we found that phase variations throughout our 1.4 GHz ATCA observations were correlated. To characterise this correlation and subsequently calculate a more appropriate SEM for each ATLAS field, we utilised the phase variation structure function which we defined as

$$\text{SF}_{\text{phase}}(\Delta t) = \text{median}\{[\text{phase}(t) - \text{phase}(t + \Delta t)]^2\}. \quad (6)$$

We calculated this structure function for phase variations seen towards the CDF-S and ELAIS-S1 gain calibrators, as displayed in the right panel of Fig. 12 and explained in the caption. For reference, phase variations for each of the gain calibrators are displayed for a single antenna and single observation in the left panels of

Fig. 12. The phase variation structure function is observed to flatten at $\Delta t \approx 6$ hours. The large-amplitude oscillations at large Δt , which are most significant for the CDF-S data for $\Delta t > 7$ hours about an approximately flat mean of $\sim 90 \text{ deg}^2$, likely demonstrate that coherent structures of scale length $\Delta t \approx 6$ hours are sequentially encountered by the array, each with slightly different mean phase.

For an outer scale of fluctuations at $\Delta t \approx 6$ hours, the effective timescale to observe statistically independent phases (i.e. uncorrelated samples at the Nyquist rate) is $\Delta t \approx 3$ hours. For quasi-sinusoidal fluctuations with period 12 hours, the structure function should rise to an outer scale at ~ 6 hours, consistent with Fig. 12. Such fluctuations are consistent with semi-diurnal oscillations in the ionosphere due to atmospheric tides (Chapman & Lindzen 1970; Spoelstra 1997).

We corrected the self-calibration rms phase values for correlation and calculated suitable SEM values as follows. We modelled the ATLAS observations using a synthesis timescale of 10 hours, characterised by a Gaussian autocorrelation function denoted by ρ_h with $\text{FWHM} = 3$ hours sampled at the 3 min self-calibration timescale. The autocorrelation function was therefore discretised into $\kappa = 201$ samples, with 60 samples per FWHM. We corrected the observed rms values following Anderson [1971; see Equation (51) in Chapter 8 of their work, adjusted to represent sample variance following their Equation (48)] using

$$\text{rms}_{\text{true}} = \text{rms}_{\text{obs}} \left[1 - \frac{2}{\kappa - 1} \sum_{h=1}^{\kappa-1} \left(1 - \frac{h}{\kappa} \right) |\rho_h| \right]^{-\frac{1}{2}}. \quad (7)$$

The value inside the square brackets was found to be 0.71. We then calculated the SEM following Anderson [1971; see Equation (32) in Chapter 8 of their work] using

$$\text{SEM} = \frac{\text{rms}_{\text{true}}}{\sqrt{\kappa}} \left[1 + 2 \sum_{h=1}^{\kappa-1} \left(1 - \frac{h}{\kappa} \right) |\rho_h| \right]^{\frac{1}{2}}. \quad (8)$$

The value inside the square brackets was found to be 59. The SEM values for the phase variations resulting from self-calibration were thus calculated as 6.1° and 4.5° for the CDF-S and ELAIS-S1 fields, respectively. For reference, we find that by computing Equation (19) from Hales et al. (2012b) with a $\sim 10''$ beam and $\text{SEM} \approx 5^\circ$, we estimate that the positional uncertainty of an image frame about an (assumed) position of a phase calibrator will be $\sim 0''.2$. We note that in the formalism above, we assume that any phase differences between the target field and phase calibrator (for example due to elevation differences) are accounted for because the ATLAS synthesis observations are long enough to sample many different elevations.

For completeness, we note that correlation timescales of ~ 3 hours are unlikely to be caused by tropospheric delay fluctuations due to water vapour (Lay 1997; Carilli & Holdaway 1999), though DC offsets due to clouds with scale sizes up to ~ 100 km (Wood & Field 2011) and ~ 3 hour timescales to advect over a point may be relevant to some of the ATLAS observations.

5.3 Deconvolution

In the absence of noise, the peak surface brightness of an unresolved radio component (assumed to be of 2D elliptical Gaussian morphology), measured in Jy beam^{-1} , is equal in magnitude to its integrated surface brightness, measured in Jy. The observed spatial extent of a Gaussian radio component, relative to the synthesised

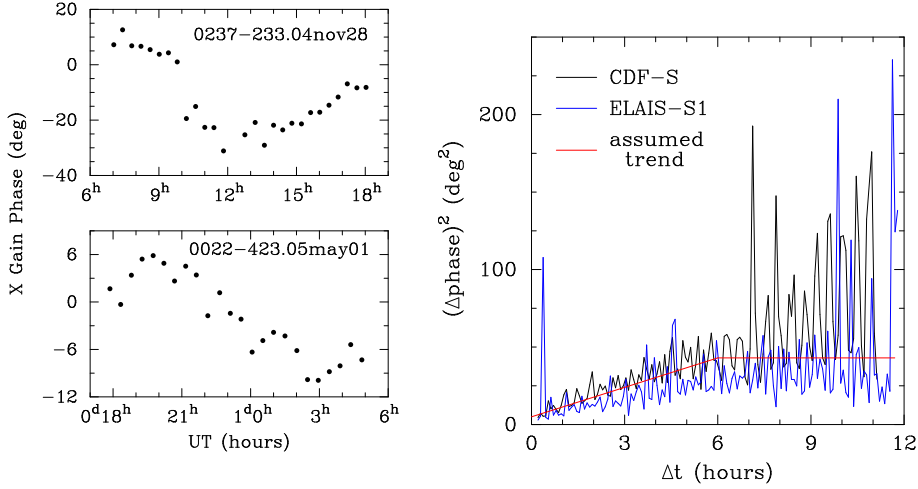


Figure 12. Upper left panel: Phase variations observed towards the CDF-S gain calibrator PKS 0237–233 using the X feed on antenna 5 throughout an observation on 2004 Nov 25. Lower left panel: Phase variations observed towards the ELAIS-S1 gain calibrator PKS 0022–423 using the X feed on antenna 4 throughout an observation on 2005 May 1. Right panel: Phase variation structure function (Equation 6), constructed by combining all ATLAS DR2 observations from all antennas for PKS 0237–233 or PKS 0022–423 in 5 min bins. The red lines represent our assumed trend (not a fit) for phase variations in the CDF-S and ELAIS-S1 data, which flatten at $\Delta t \approx 6$ hours. The oscillations with period $\Delta t \approx 25$ mins are due to aliasing; gain calibrators were typically observed every 25 mins.

beam, may therefore be deduced from its ratio of integrated to peak surface brightness (e.g. Prandoni et al. 2000; Bondi et al. 2003; Huynh et al. 2005; Schinnerer et al. 2010), namely

$$\frac{S_{\text{int}}}{S_{\text{peak}}} = \frac{\theta_{\text{maj}} \theta_{\text{min}}}{B_{\text{maj}} B_{\text{min}}} \quad (9)$$

where θ_{maj} and θ_{min} are the component’s observed (not deconvolved) major and minor axis FWHMs, respectively. If images were noise-free, then the ratio $S_{\text{int}}/S_{\text{peak}}$ would be unity for unresolved components and > 1 for resolved components, following from perfect component extraction and measurement. However, noise in real images causes some unresolved components to exhibit $S_{\text{int}} < S_{\text{peak}}$ and others $S_{\text{int}} > S_{\text{peak}}$, such that not all components with $S_{\text{int}}/S_{\text{peak}} > 1$ may be unambiguously classified as being resolved.

To classify each ATLAS component as unresolved or resolved, we first examined the distribution of $S_{\text{int}}/S_{\text{peak}}$ for all components in each survey field as a function of their detection SNR, A_s , as shown in Fig. 13. To prevent polarization bias from shifting the positions of linearly polarized components in Fig. 13, we performed two first-order debiasing (FOD) corrections (Leahy & Fernini 1989). We corrected the detection SNRs using $A_L^{\text{FOD}} \approx (A_L^2 - 1^2)^{1/2}$, and the peak polarized surface brightness measurements using $L_{\text{peak}}^{\text{FOD}} \approx [L_{\text{peak}}^2 - \sigma_{\text{RM}}^2/\varpi^2]^{1/2}$. No bias corrections were required for L_{int} (see Hales et al. 2012b). We note that, as discussed by Hales et al. (2012a), the FOD scheme is designed for application to data exhibiting Ricean statistics and not L_{RM} as relevant here. However, at the SNRs relevant to our data, the probability density functions characterising the Rice (1945) distribution and the $M = 28$ distribution for L_{RM} are very similar (see Hales et al. 2012a). We therefore assume approximate validity of the FOD scheme in application to the analysis described in this section. We found no significant shifting of points in Fig. 13 when debiasing corrections were neglected entirely, demonstrating that the distribution of points is not highly sensitive to polarization bias.

To identify unresolved components within the total intensity panels of Fig. 13, we defined a locus enveloping $\sim 99\%$ of components with $I_{\text{int}}/I_{\text{peak}} < 1$. We then mirrored this locus above the $I_{\text{int}} = I_{\text{peak}}$ line, assuming the presence of a similar distribution of unresolved components with $I_{\text{int}}/I_{\text{peak}} > 1$. We assumed that these loci also characterised the linear polarization data; separate polarization loci were not constructed. We defined the upper locus using the function (Schinnerer et al. 2010)

$$\frac{S_{\text{int}}}{S_{\text{peak}}} = a^{-b/(A_s)^c}, \quad (10)$$

with $a = 0.35$, $b = 7.0$, $c = 1.1$, and where in linear polarization we replaced S_{peak} by $L_{\text{peak}}^{\text{FOD}}$ and A_s by A_L^{FOD} . All components above the upper locus were classified as resolved and assigned flux densities given by I_{int} or L_{int} , while all components below it were classified as unresolved and assigned flux densities given by the magnitudes of I_{peak} or L_{peak} . A total of 189 (22) and 204 (7) components were classified as resolved in total intensity and linear polarization, the latter in parentheses, within the CDF-S and ELAIS-S1 survey areas, respectively. For each resolved component, we used Equation (9), with S_{peak} replaced by $L_{\text{peak}}^{\text{FOD}}$ in linear polarization, to estimate a deconvolved angular size as

$$\Theta \approx \sqrt{\theta_{\text{maj}} \theta_{\text{min}} - B_{\text{maj}} B_{\text{min}}}. \quad (11)$$

We calculated upper bounds to the deconvolved angular sizes of unresolved components by equating Equation (9) with Equation (10) and then evaluating Equation (11). We note that direct measurements of θ_{maj} and θ_{min} were not used, nor required, for the analysis presented above; a characteristic angular size $\theta \approx \sqrt{\theta_{\text{maj}} \theta_{\text{min}}}$ was evaluated for each component using Equation (9), which was then deconvolved using Equation (11). We estimated the uncertainty in measurements of Θ for resolved components by following standard

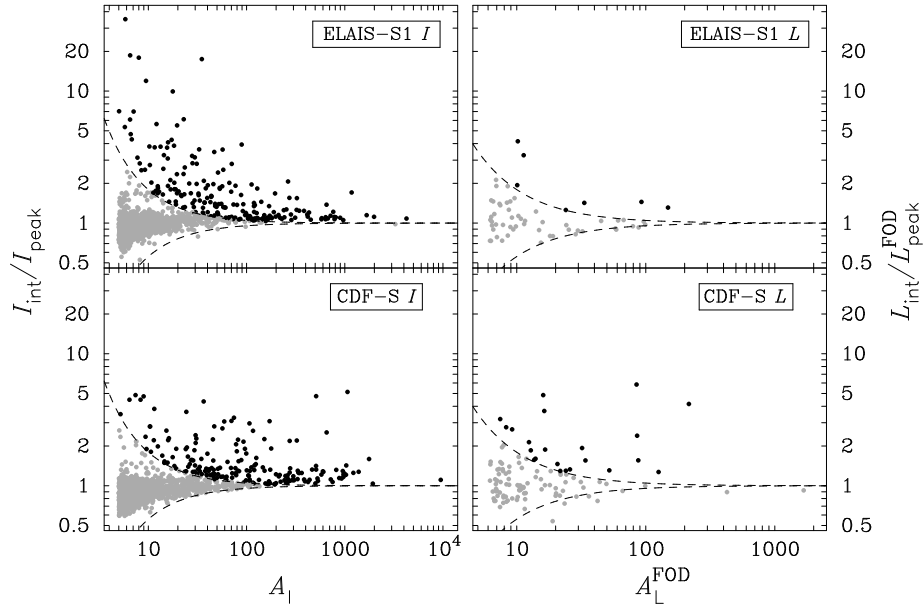


Figure 13. Ratio of integrated to peak surface brightness as a function of detection SNR for total intensity (left column) and linear polarization (right column) components in the ELAIS-S1 (top row) and CDF-S (bottom row) fields. In linear polarization, detection SNRs and peak surface brightness measurements have been corrected for Ricean bias using a first-order debiasing scheme. The loci in each panel, given by Equation (10) and mirrored below the $S_{\text{int}} = S_{\text{peak}}$ line, enable classification of components as unresolved (grey points) or resolved (black points).

error propagation, resulting in

$$\sigma_{\Theta} \approx \sqrt{\frac{B_{\text{maj}} B_{\text{min}}}{4 (S_{\text{int}}/S_{\text{peak}} - 1)} \left[\left(\frac{\sigma_{S_{\text{peak}}}}{S_{\text{peak}}} \right)^2 + \left(\frac{\sigma_{S_{\text{int}}}}{S_{\text{int}}} \right)^2 \right]}. \quad (12)$$

We set angular size uncertainties for unresolved components to zero.

In reality, it is not possible for a component to be truly unresolved (components have real physical dimensions). The flux densities of components classified as unresolved by the scheme above will therefore be systematically underestimated, due to their assignment using S_{peak} . We do not correct for this flux density bias on an individual component basis, which depends on the SNR and flux density of each component as well as the distribution of intrinsic angular sizes, and which will become increasingly significant at faint flux densities where majority of components are classified as unresolved using Equation (10). However, we do account for this bias in a collective sense in Section 7.1 when considering component number-counts in flux density bins.

5.4 Total Intensity and Linear Polarization Deboosting

For a given observed flux density, the probability of detecting a faint unresolved component located on a noise peak is greater than the probability of detecting a strong unresolved component located in a noise trough, because faint radio components are more numerous. This results in a bias between true and observed flux densities known as flux density boosting (following the terminology of Vieira et al. 2010), which depends on the SNR of the detection, the noise distribution in which the detection was made, and the slope of the radio component differential number-counts, γ , where $dN/dS \propto S^{-\gamma}$. Flux density boosting of individual components leads to Eddington (1913) bias in their observed differential number-counts; we discuss Eddington bias later in Section 7.2.

To account for flux density boosting we used Bayes' theorem

to quantify the bias (Jeffreys 1938; Eddington 1940), obtaining the posterior distribution

$$f(S_{\text{TRUE}}|S_{\text{OBS}}) \propto f(S_{\text{OBS}}|S_{\text{TRUE}}) f(S_{\text{TRUE}}), \quad (13)$$

where S_{OBS} is the observed flux density, S_{TRUE} is the true flux density, $f(S_{\text{OBS}}|S_{\text{TRUE}})$ is the likelihood of measuring S_{OBS} given S_{TRUE} , and $f(S_{\text{TRUE}})$ is a prior which is proportional to the differential number counts dN/dS . We obtained maximum-likelihood (ML) solutions to Equation (13), described as follows, to correct component flux densities for boosting in total intensity and linear polarization; we use the term deboosting to describe these corrections. We note that deboosting is not required for resolved components because noise fluctuations about their true peak surface brightnesses are largely accounted for by extraction algorithms such as those used in BLOBCAT and IMFIT; we have not applied any of the deboosting corrections described in this section to resolved components.

In total intensity, we deboosted observed flux densities using the ML solution (Jauncey 1968; Hogg & Turner 1998)

$$I_{\text{ML}} = \frac{I}{2} \left(1 + \sqrt{1 - \frac{4\gamma_1}{A_l^2}} \right), \quad (14)$$

which implicitly takes into account the presence of bandwidth smearing (provided that the assumptions described at the end of this section are met). To model the differential component number-counts curve and in turn obtain its slope γ_1 , we used the sixth-order empirical fit to the Phoenix and FIRST surveys presented by Hopkins et al. (2003). This curve, which we denote by H03, is given by

$$\log \left[\frac{dN_{\text{H03}}/dI}{I^{-2.5}} \right] = \sum_{j=0}^6 a_j \left[\log \left(\frac{I}{\text{mJy}} \right) \right]^j, \quad (15)$$

with $a_0 = 0.859$, $a_1 = 0.508$, $a_2 = 0.376$, $a_3 = -0.049$, $a_4 = -0.121$, $a_5 = 0.057$, and $a_6 = -0.008$. In Fig. 14 we

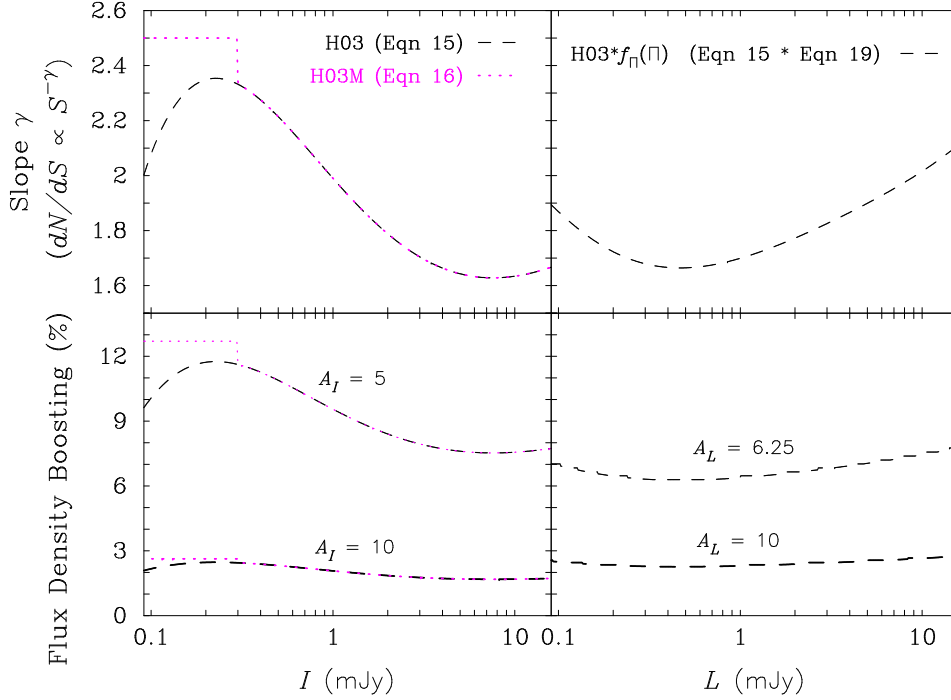


Figure 14. Flux density boosting as a function of observed flux density in total intensity (left column) and linear polarization (right column) for unresolved components with observed SNRs as indicated. The dashed and dotted curves represent different underlying number-count distributions. Polarization results utilising the H03M model are not shown, as they are identical to the H03 results over the flux density range shown.

plot the boosting ratio I/I_{ML} resulting from Equation (14) with γ_1 obtained from H03. There are suggestions that the H03 number-counts fall off too quickly at faint flux densities (e.g. Singal et al. 2010; Morrison et al. 2010; Vernstrom, Scott, & Wall 2011). To illustrate the potential boosting effects of an exaggerated population of faint components, we have constructed a modified H03 distribution, which we denote by H03M, by inserting a Euclidean slope between 30–300 μJy , namely

$$\frac{dN_{\text{H03M}}}{dI}(I) = \begin{cases} dN_{\text{H03}}/dI(I) & \text{if } I \geq 300 \mu\text{Jy} \\ dN_{\text{H03}}/dI(300 \mu\text{Jy}) & \text{if } 30 \leq I < 300 \mu\text{Jy} \\ dN_{\text{H03}}/dI(10 \times I) & \text{if } I < 30 \mu\text{Jy} \end{cases} \quad (16)$$

In Fig. 14 we plot the boosting ratio I/I_{ML} using γ_1 obtained from H03M; differences between the H03 and H03M solutions are minimal, being limited to faint components with low-SNR.

In linear polarization, we obtained the posterior distribution from Equation (13) by assuming that observational errors were described by the Rice (1945) distribution (note comments in Section 5.3), giving

$$f(L_{\text{TRUE}}|L, \sigma_{\text{RM}}, \varpi, \gamma_L) \propto \left(\frac{L_{\text{TRUE}}}{L} \right)^{-\gamma_L} \frac{L}{\tilde{\sigma}_{\text{RM}}^2} \times \exp \left(-\frac{I_{\text{TRUE}}^2 + L^2}{2\tilde{\sigma}_{\text{RM}}^2} \right), \quad (17)$$

where we define $\tilde{\sigma}_{\text{RM}} = \sigma_{\text{RM}}/\varpi$. The ML solution for each linearly polarized component with observed flux density L (corrected for bandwidth smearing) was then found by solving for L_{ML} in

$$\left(\frac{L_{\text{ML}}}{\tilde{\sigma}_{\text{RM}}} \right)^2 - \frac{L_{\text{ML}}}{\tilde{\sigma}_{\text{RM}}} \frac{\mathcal{I}_1(L_{\text{ML}}/\tilde{\sigma}_{\text{RM}})}{\mathcal{I}_0(L_{\text{ML}}/\tilde{\sigma}_{\text{RM}})} + \gamma_L = 0, \quad (18)$$

where \mathcal{I}_k are modified Bessel functions of the first kind of order k . To enable evaluation of γ_L , the slope of the linearly polarized

differential component number-counts $dN/dL \propto L^{-\gamma_L}$, we constructed a model for dN/dL by convolving the total intensity H03 distribution from Equation (15) with a probability distribution for fractional linear polarization $f_{\Pi}(\Pi) \equiv f_{\Pi}(L/I)$ given by

$$f_{\Pi}(\Pi) = \frac{1}{\Pi\sigma_{10} \ln(10) \sqrt{2\pi}} \exp \left\{ -\frac{[\log_{10}(\Pi/\Pi_0)]^2}{2\sigma_{10}^2} \right\}, \quad (19)$$

where $\Pi_0 = 4.0\%$ and $\sigma_{10} = 0.3$. The motivation for using Equation (19) is described in detail in Paper II. We denote the resulting dN/dL model by $\text{H03} * f_{\Pi}(\Pi)$. The calculated L/L_{ML} boosting ratios for components with low SNR detections over a range of flux densities are displayed in Fig. 14.

Formally, Equations (14) and (18) are only valid for constant slopes (i.e. for γ_s independent of flux density); however, in practice, their solutions are valid provided that their input slopes do not exhibit large changes as functions of flux density. Separately, we note that the solutions above assume that all components are observed as truly unresolved; while this assumption is not met by our data (real sources have non-zero extents), we estimate that any resulting systematic errors due to slope miscalculation are much smaller than the flux density uncertainties for each component.

6 CROSS-IDENTIFICATION AND CLASSIFICATION

To construct a catalogue of radio sources we implemented two cross-identification and classification schemes. The first scheme was used to cross-match radio sources comprising individual or multiple total intensity components with infrared and optical counterparts, and to classify each of these sources according to their multiwavelength properties. The second scheme was used to cross-match linearly polarized radio components with their total intensity

counterparts, to obtain polarization upper limits for total intensity components and sources lacking catalogued polarized counterparts, and where possible to classify these associations based on their polarized morphologies. The two schemes are described as follows.

6.1 Total Intensity Radio–Infrared–Optical Associations

6.1.1 Cross-Identification

We followed a similar procedure to that described by Norris et al. (2006) and Middelberg et al. (2008) for ATLAS DR1 to cross-identify radio components with SWIRE infrared sources and to identify radio sources comprising multiple components. We began by utilising the DR1 radio component catalogues, searching them for matches at the position of each DR2 total intensity component. If a DR1 component was found within $5''$ of a DR2 position, then the SWIRE identification found in DR1 was applied to the DR2 component. In the case of identifications made by Middelberg et al. (2008) with the SWIRE Data Release 4 (SDR4) catalogue, which was never fully published, a re-identification with the SDR3 catalogue was made by searching for a SDR3 source within $1''$ of the SDR4 position. A small number of SDR4 sources were not found in SDR3, in which case we assumed no DR1-assisted cross-match was available for the DR2 radio component. For each remaining DR2 component without an infrared cross-identification, we searched the SDR3 catalogue for an associated source within $7''$ using a nearest-neighbour match; we did not take into account the infrared colours of potential matches. We then examined a number of components by eye using radio contours superimposed on the SWIRE $3.6\ \mu\text{m}$ image, assessing the suitability of each cross-identification, or lack thereof. We used this radio-contoured infrared image to identify nearby components that were clearly physically associated with each other. In 36 cases, nearby components were found to form a triple radio source in which a core of radio emission from a host galaxy lay roughly midway between two radio lobes; we comment on our use of the terms *core* and *lobe* below. Of these 36 cases, we found that 34 comprised 3 components, 1 comprised 4 components, and 1 comprised 6 components. In 78 cases, pairs of components were found to form a double radio source comprising twin radio lobes with no detected emission from a core. In 41 cases, pairs of components were found to exhibit core-lobe morphology. For each of these 155 multi-component cases, we grouped the components together and assigned them to a common radio source; each of the remaining 2066 radio components were assigned to a single-component radio source. The ATLAS DR2 source catalogue thus comprised a total of 2221 sources. We found that 149 of the multi-component sources and 1774 of the single-component sources were matched with SWIRE sources, leaving a total of 298 radio sources without identifiable infrared counterparts. Of these un-matched sources, only 2 of them (sources C5 and C318) were the result of incomplete SWIRE coverage (97%) over the ATLAS DR2 CDF-S survey area. Finally, using the pre-matched infrared-optical data (Section 2.2.2), we associated 409 optical sources with DR2 radio sources.

We note that not all radio components were examined by eye as part of our cross-identification procedure, and that a large number of components (perhaps ~ 200 or more) are likely to remain unassociated with true multi-component sources. Statistics regarding associations between radio components and infrared sources are thus incomplete. Furthermore, because the sky density of SWIRE sources ($\sim 60,000\ \text{deg}^{-2}$) is much higher than that of ATLAS DR2 radio sources ($\sim 350\ \text{deg}^{-2}$), there is a chance that

some of our radio-infrared cross-identifications are incorrect. We have not carried out an error analysis to estimate an upper limit to the false-positive cross-identification rate for our data. However, we note that this upper limit was estimated in DR1 as being $\sim 5\%$; see Norris et al. (2006) and Middelberg et al. (2008) for details. This rate is likely to be representative of our cross-matched DR2 data. The issues above do not impact upon the key ATLAS results presented in Paper II.

6.1.2 Classification

We classified each source according to whether their energetics were likely to be driven by an AGN, star formation (SF) within a star-forming galaxy (SFG), or emission associated with an individual star. Similar to Padovani et al. (2011), we define AGN sources as those with energetics dominated in at least one wavelength band by a supermassive black hole. We have not split sources containing an AGN into subclasses such as Fanaroff & Riley (1974) type I (FRI; limb-darkened) and type II (FRII; also known as classical double or triple radio sources due to their limb-brightened morphologies). Given that the resolutions of our ATLAS data ($\sim 10''$) often limited our ability to identify regions of emission associated with AGN jets (FRI sources) compared with lobes formed about jet-termination hotspots (FRII sources), we have systematically used the term *lobe* to describe both jets and lobes in sources with radio double or triple morphologies. For completeness, we note that our use of the term *core* in radio triple sources is generic in that it does not indicate physical association with a compact, flat-spectrum region of emission. Because spectral indices are not considered in this work, restarted AGN jets or lobes may contribute or even dominate the emission observed in the regions we have designated as cores. We provide our working definition of SFGs further below.

We used four selection criteria to identify AGNs – radio morphologies, $24\ \mu\text{m}$ to 1.4 GHz flux density ratios, mid-infrared colours, and optical spectral characteristics – with the latter also used to identify SFGs and stars. We describe each of these criteria below.

Radio morphology. – We classified each source exhibiting a lobe-core-lobe, lobe-lobe, or core-lobe radio morphology as an AGN; 150 sources were identified as AGNs by this criterion.

Infrared-radio ratio. – The linear and tight correlation between global far-infrared (FIR) and radio emission from star-forming systems (e.g. Lacki, Thompson, & Quataert 2010; Sargent et al. 2010, and references therein), known as the FIR-radio correlation (FRC), may be used to identify radio-loud AGN due to their departure from this relationship (e.g. Sopp & Alexander 1991). Following Helou, Soifer, & Rowan-Robinson (1985), the FRC is commonly referred to by the parameter q , which is the logarithm of the ratio between FIR to radio flux density. Appleton et al. (2004) found that $q_{24} = \log_{10}[S_{24.0\ \mu\text{m}}/S_{1.4\ \text{GHz}}] = 0.8$ for flux density measurements at $24\ \mu\text{m}$ and 1.4 GHz; we use this relationship as a surrogate for the FRC. We classified each source with a radio flux density more than ten times that expected from the FRC as an AGN, namely for sources with $q_{24} \leq -0.2$, including those sources with SWIRE non-detections (limits are given in Section 2.2.1) meeting this criterion; 878 sources were classified as AGNs by this approach. Given the relative lack of multiwavelength data included in this work, no corrections were made to convert observed $24\ \mu\text{m}$ and 1.4 GHz flux densities to rest-frame values (e.g. Padovani et al. 2011), nor were full K-corrections performed (Kellermann 1964; Sargent et al. 2010, and references therein). However, we note

that our $q_{24} \leq -0.2$ scheme ensures that only sources departing strongly from the FRC are classified as AGNs. It is therefore unlikely that the corrections above would significantly alter our AGN classifications. We note that Appleton et al. (2004) and others (e.g. Sargent et al. 2010; Mao et al. 2011) found no significant evolution of the FRC with redshift (though see Ivison et al. 2010).

Mid-infrared colours.—Following the observation of a large sample of extragalactic sources with the *Spitzer Space Telescope*, Lacy et al. (2004) recognised that the distribution of IRAC colours exhibited by AGNs extended into a region of parameter space largely devoid of other source classes. Sajina, Lacy, & Scott (2005) extended this work, investigating the parameter space occupied by continuum-dominated sources for redshifts ranging between $z \sim 0 - 2$ and investigating the colours of SFG candidates dominated by polycyclic aromatic hydrocarbon (PAH) and sources dominated by old-population (10 Gyr) starlight emission. Here we focus on the continuum-dominated sources, displayed as blue points in the top two panels of Fig. 10 from Sajina, Lacy, & Scott (2005). We followed Padovani et al. (2011) to construct a locus for identifying AGNs, which we defined as the union of $\log_{10}[S_{8.0\mu\text{m}}/S_{4.5\mu\text{m}}] > 0$, $\log_{10}[S_{5.8\mu\text{m}}/S_{3.6\mu\text{m}}] > 0$, and $\log_{10}[S_{8.0\mu\text{m}}/S_{4.5\mu\text{m}}] < 11 \log_{10}[S_{5.8\mu\text{m}}/S_{3.6\mu\text{m}}]/9 + 0.3$, and classified each source falling within its boundaries as an AGN; 238 sources were classified as AGNs by this approach.

Optical spectrum.—Each optical spectrum was classified visually by Mao et al. (2012) as an AGN, SFG, or star. Sadler et al. (1999) reported that a similar ‘eyeball’ classification scheme for spectra obtained with the 2dF (Two-degree Field) spectrograph (Lewis et al. 2002) was robust and could be used with confidence. Given this visual classification system, in this work we define SFGs (somewhat loosely) as galaxies with SF rates sufficient to produce an optical spectrum exhibiting (1) emission lines and line ratios characteristic of SF, such as a strong and narrow $\text{H}\alpha$ line, and (2) a distinct lack of features typically associated with AGN activity (see AGN/SF classification details in Sadler et al. 1999). The latter criterion maintains consistency with our definition of AGN sources above. Using the optical data, we classified 279 sources as AGNs, 126 as SFGs, and 4 as stars. Of these, we found that 12 SFGs and 2 stars had been classified as an AGN by one of the previously described AGN selection criteria, with an additional 2 SFGs classified as an AGN by two of the previous criteria. Given the high quality of the spectral classifications and the statistical nature of the previous AGN diagnostics, we reclassified each of these sources according to their optical classifications.

In summary, of the 2221 catalogued ATLAS DR2 sources, 1169 were classified as AGNs, 126 as SFGs, and 4 as radio stars. Of the AGN sources, 858 were recognised as such by only one of the four diagnostics above, 255 were recognised by two, 47 by three, and only 9 sources were recognised as an AGN by all four diagnostic criteria. We note that our classifications are biased in favour of AGNs, due to the overheads required to classify stars and SFGs using optical spectroscopy. Therefore, in general our data are unsuited to the investigation of relationships between star formation and AGN activity.

6.2 Linear Polarization—Total Intensity Associations

6.2.1 Cross-Identification

To enable the investigation of fractional polarization trends, we visually cross-matched each linearly polarized component with a total intensity counterpart. In most cases it was possible to match an

individual linearly polarized component with an individual total intensity component and, in turn, their associated multiwavelength counterpart from Section 6.1. However, in some cases, one-to-one matches were prevented due to ambiguities posed by the blending of adjacent components in total intensity or linear polarization. For example, we encountered situations in which a linearly polarized component was positioned mid-way between two blended total intensity components, such that it was unclear whether the polarized emission was caused by one of the total intensity components, or both. Given such complexities in our data, we avoided the use of a simple nearest-neighbour scheme for cross-matching, as this would have led to overestimates of fractional polarization for any mis-matched components. Instead, we grouped together all linearly polarized and total intensity components contributing to an ambiguous cross-match, so that the fractional polarization could be obtained for the group rather than for any potentially incorrect subset of the group. In total, we found that 130 of the 2221 catalogued ATLAS DR2 sources exhibited linearly polarized emission, 118 of which had available infrared cross-identifications. Statistics of one-to-one and group associations are presented below.

In Fig. 15 we display the four types of cross-matches encountered in our data. The top-left panel shows a one-to-one match between a linearly polarized component and a total intensity component. The bottom-left panel shows a two-component total intensity source exhibiting limb-brightened linearly polarized emission, which we interpret as an unambiguous one-to-one match between the polarized component and the western total intensity component; the eastern component is undetected in polarization. The top-right panel shows the only example in our data where a single total intensity component was found to be enveloping two separate linearly polarized components; all three components were assigned to a group. We note that this example is likely to be highlighting a total intensity component that should have been decomposed into two separate components during the `BLOCAT/IMFIT` extraction phase, rather than a perfectly Gaussian total intensity component with unusual polarization substructure. The bottom-right panel shows an example of an ambiguous match between a linearly polarized component and two total intensity components; all three components were grouped together to prevent potential overestimation of the fractional polarization for either total intensity component.

To enable the investigation of fractional polarization trends using all available radio data, not just using the one-to-one and group associations identified above, we calculated upper limits to the linearly polarized flux densities of all total intensity components lacking a polarization counterpart. As discussed extensively by Kashyap et al. (2010), we note the distinction between an upper limit and an upper bound¹⁰. We followed the procedure outlined by Kashyap et al. (2010) to evaluate polarization upper limits at the positions of unpolarized total intensity components. By combining the Type I error rate of $\alpha = 10^{-7}$ from Section 5.1, a Type II error rate conservatively defined as $\beta = 0.9$, and the probability density function (PDF) for L_{RM} with $M = 28$ given by Equation (28) from Hales et al. (2012a), we evaluated that the upper limit definition

¹⁰ An upper bound describes an inference range for a flux density measurement; an upper limit, on the other hand, describes the minimum flux density required to ensure detection at a specified false-positive (Type I) error rate (i.e. a SNR cutoff) and false-negative (Type II) error rate for a given noise distribution, and thus calibrates the detection process irrespective of the observed flux density.

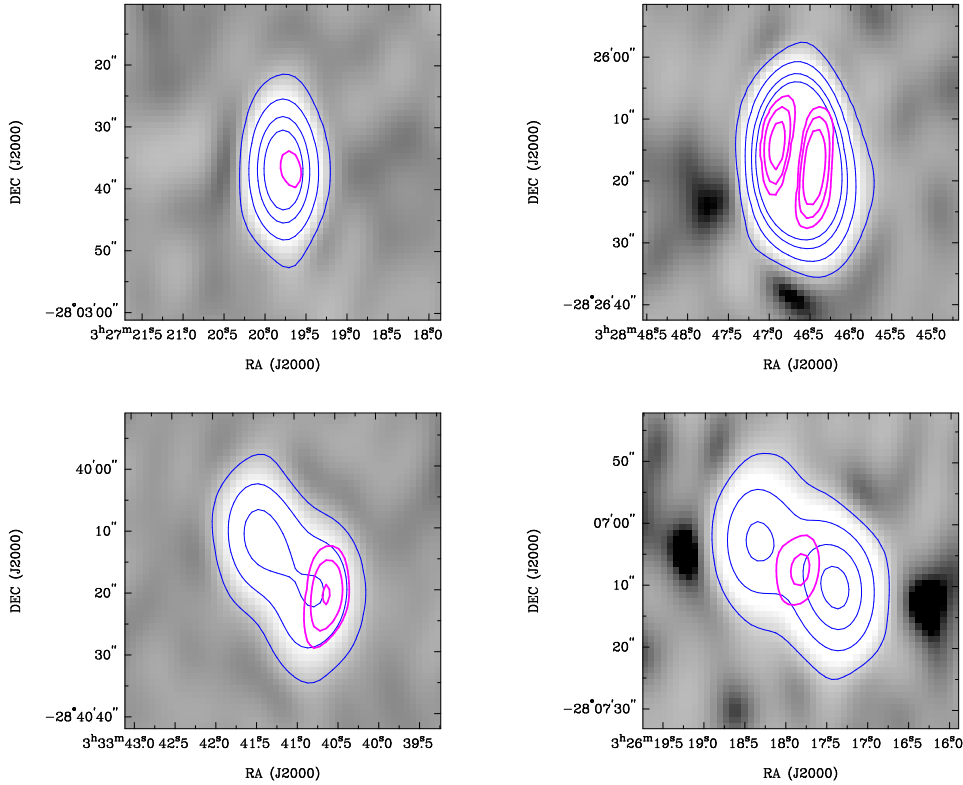


Figure 15. Examples of one-to-one (left column panels) and complex (right column panels) cross-identifications encountered between linearly polarized components and total intensity counterparts. Background total intensity images in each panel are shaded logarithmically, saturating black below $-0.2 \text{ mJy beam}^{-1}$ and white above 1 mJy beam^{-1} . Total intensity contours (blue) represent 5, 25, 60, and 100σ . Linear polarization contours (magenta) represent 6.25, 10, and $15\sigma_{\text{RM}}$. Respective beam sizes are given in Section 3.2 and Section 3.3. See Section 6.2.1 for panel details.

required to meet these statistical criteria was

$$L_{\text{UL}} = 7.46 \sigma_{\text{RM}}. \quad (20)$$

For unpolarized sources, we assigned polarization upper limits by selecting the weakest limit (i.e. largest in magnitude) associated with any constituent total intensity component.

6.2.2 Classification

We visually classified each one-to-one and group association from above, each source comprising two such associations (no source had more than two), and each unpolarized component according to the following scheme, which we designed to account for differing (de-)polarized morphologies. Examples of each classification type are displayed in Fig. 15, Fig. 16, and Fig. 17, as described below.

Type 0 – A one-to-one or group association identified as a lobe of a double or triple radio source. Both lobes of the source are clearly polarized, having linearly polarized flux densities within a factor of 3. (These criteria do not formally reference the ratio between lobe total intensity flux densities, which we note here are within a factor of 3 for all double or triple ATLAS DR2 sources; cf. Magliocchetti et al. 1998.) To illustrate, two Type 0 associations are displayed in the right panel of Fig. 16, one for each lobe.

Types 1/2 – A one-to-one or group association identified as a lobe of a double or triple radio source that does not meet the criteria for Type 0. A lobe classified as Type 1 indicates that the ratio of polar-

ized flux densities between lobes is greater than 3. A lobe classified as Type 2 indicates that the opposing lobe is undetected in polarization and that the polarization ratio may be less than 3, in which case it is possible that more sensitive observations may lead to reclassification as Type 0. Sources with lobes classified as Type 1 exhibit asymmetric depolarization in a manner qualitatively consistent with the Laing-Garrington effect (Laing 1988; Garrington et al. 1988), where one lobe appears more fractionally polarized than the opposite lobe. To illustrate, Type 1 associations are suitable for the pair of lobes displayed in each panel of Fig. 17. A Type 2 classification is appropriate for the detected lobe shown in the bottom-left panel of Fig. 15.

Type 3 – A group association representing a source, involving a linearly polarized component situated midway between two total intensity components. It is not clear whether such associations represent two polarized lobes, a polarized lobe adjacent to a depolarized lobe, or a polarized core. An example is displayed in the bottom-right panel of Fig. 15.

Type 4 – An unclassified one-to-one or group association representing a source. Examples of the former and latter are displayed in the top-left and top-right panels of Fig. 15, respectively.

Type 5 – A one-to-one association clearly identified as the core of a triple radio source (where outer lobes are clearly distinct from the core). An example is displayed in the left panel of Fig. 16.

Type 6 – A source comprising two Type 0 associations, or a group association representing a non-depolarized double or triple radio source where blended total intensity and linear polarization com-

ponents have prevented clear subdivision into two Type 0 associations. For example, a Type 6 source is displayed in the right panel of Fig. 16.

Type 7 – A source comprising one or two Type 1 associations. For example, each panel of Fig. 17 displays a Type 7 source.

Type 8 – A source comprising one Type 2 association. For example, a Type 8 source is displayed in the bottom-left panel of Fig. 15.

Type 9 – An unpolarized component or source.

From a total of 172 catalogued linearly polarized components, 138 were found to exhibit clear one-to-one associations with individual total intensity components. The remaining 34 polarized components required grouping in order to be associated with total intensity counterparts. We classified 58 one-to-one associations as Type 0, 4 as Type 1, 25 as Type 2, 48 as Type 4, and 3 as Type 5. We note that all 3 sources containing Type 5 core associations exhibited unpolarized lobes. Of the group associations comprising a total of 34 polarized components, 2 groups were classified as Type 0, 14 as Type 3, 1 as Type 4, and 8 as Type 6. We classified 29 sources comprising two Type 0 associations as Type 6. We classified 2 sources as Type 7, each of which exhibited linearly polarized emission from both the polarized and depolarized lobe, and 25 sources as Type 8.

As described above, only 1 group association was classified as Type 4 (see top-right panel of Fig. 15). While it is possible that the two polarized components within this group are in reality a single extended region of polarized emission, broken in two by a depolarization canal (e.g. Fletcher & Shukurov 2006), a more likely explanation as commented on above is that rather than there being a single total intensity component, two adjacent polarized lobes are in fact present.

7 COMPONENT NUMBER-COUNT BIASES

We used the DR2 component catalogue to construct 1.4 GHz differential component counts in total intensity and linear polarization for each ATLAS field. We did not use the DR2 source catalogue to construct differential source counts because of concern regarding the multi-component association process (recall Section 6.1.1). The resulting component counts will be presented in Paper II; here we describe our method.

The differential component counts were calculated by dividing the number of sky density normalised components (i.e. units of sr^{-1}) observed within each flux density bin by the bin width, then multiplying each bin value by two bias correction factors. The effective number of components in each i 'th flux density bin was thus calculated as

$$N_{\text{eff},i} = r_i e_i \sum_{j=1}^{J_i} (V_j^{\text{AREA}} F^{\text{AREA}})^{-1}, \quad (21)$$

where F^{AREA} denotes the relevant field area from Section 4.4, and the visibility area term V_j^{AREA} accounts for the potentially limited survey area over which each j 'th of J_i components in each bin could have been detected due to spatial variations in image sensitivity and bandwidth smearing (see Section 5.1). Only bins with visibility area factors greater than 0.1 were accepted for the number count results presented in Paper II. The correction factors r_i and e_i were used to account for resolution bias and Eddington bias, respectively, as described in Section 7.1 and Section 7.2 below. The differential counts, representing the number of components per unit sky area per unit flux density, were then normalised by the standard Euclidean slope of $S^{-2.5}$ (Longair 1966; Ryle 1968).

7.1 Resolution Bias

We use the term resolution bias to collectively describe two effects: (1) incompleteness in number-count bins resulting from a lack of sensitivity to resolved components with low surface brightness, and (2) the redistribution of counts between bins resulting from systematic undervaluation of flux densities for components classified as unresolved. An analytic scheme to account for the first effect has been attempted by Prandoni et al. (2001) and Huynh et al. (2005). The second effect was identified in an empirical investigation by Bondi et al. (2008); an analytic formalism to describe this effect is not presently available. In this section we present a new analytic method that both improves upon the scheme described by Prandoni et al. (2001) and Huynh et al. (2005) and accounts for the bias described by Bondi et al. (2008).

7.1.1 Effect 1: Sensitivity to Resolved Components

We begin by discussing incompleteness to resolved components, which may be manifested in two ways.

First, a lack of short baselines can limit the maximum observable angular size of components. For a minimum projected baseline of 30 m, at 1.4 GHz the ATCA becomes progressively insensitive¹¹ to components larger than $5'$, at which point only 50% of a component's true flux density can be detected (e.g. Forster 1983). Given that no millijansky sources are expected to exhibit such large angular sizes (according to any of the distributions described below) and that ATLAS observations include projected baselines down to 30 m (see Section 2.1), we assume that no limitations have been imposed on observable component angular sizes by ATLAS uv -plane coverage.

Second, components with flux densities sufficient to be included in a number-count bin may be resolved to the extent that their peak surface brightnesses may fall below the SNR detection threshold, preventing them from being catalogued and counted and thus resulting in bin incompleteness. To correct for this second type of incompleteness to resolved components in the total intensity and linear polarization number-counts for each ATLAS field, we estimated the fraction of missing components at any given flux density by comparing the maximum detectable angular size with an underlying true size distribution.

We estimated the maximum intrinsic (i.e. deconvolved) angular size, $\Theta_{\text{max}}(S)$, that a component with flux density S could attain while still meeting the detection threshold by modifying Equation (9) and deconvolving using Equation (11), deriving

$$[\Theta_{\text{max}}(S)]^2 = \left\{ \int_0^{S/A_S} \sqrt{\frac{S B_{\text{maj}} B_{\text{min}}}{A_S z}} f_{\tilde{\sigma}}(z) dz \times \left[\int_0^{S/A_S} f_{\tilde{\sigma}}(z') dz' \right]^{-1} \right\}^2 - B_{\text{maj}} B_{\text{min}}, \quad (22)$$

where A_S is the SNR threshold given by 5.0 in total intensity or 6.25 in linear polarization, we have defined $\tilde{\sigma}(x, y) = \sigma(x, y)/\varpi(x, y)$ (or using σ_{RM} in polarization), and where $f_{\tilde{\sigma}}$ is a probability distribution for $\tilde{\sigma}$ [in practice this is a normalised histogram of $\tilde{\sigma}(x, y)$ values]. The integrals in Equation (22) enable

¹¹ Joint deconvolution schemes can recover larger scales than those from single pointing schemes (Sault, Staveley-Smith, & Brouw 1996); computational limitations prevented joint deconvolution of the ATLAS data.

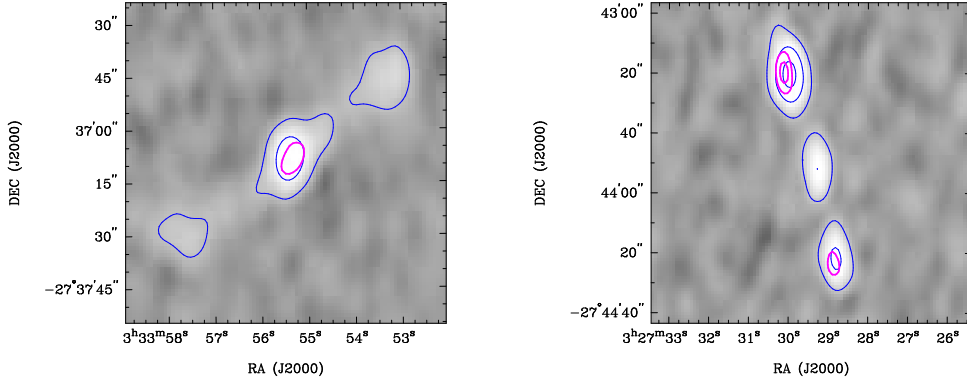


Figure 16. Examples of linear polarization–total intensity classifications (see also Fig. 15 and Fig. 17). Panel shading and contours are identical to Fig. 15. The left panel shows a Type 5 association. The right panel shows a Type 6 source with two Type 0 lobes.

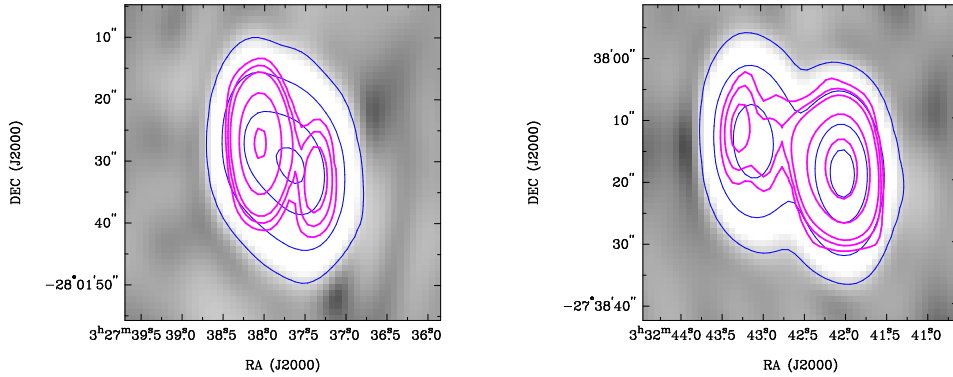


Figure 17. Classical double sources in ATLAS that appear to exhibit asymmetric depolarization. Each lobe was classified as Type 1, and thus each source as Type 7. The left panel displays source C7. This source is best fit by two Gaussian components in total intensity, the centroids of which correspond to the components observed in linear polarization. Flux densities for the Eastern and Western lobes are $I = 30.6$ mJy and $L = 2.3$ mJy, and $I = 64.5$ mJy and $L = 0.5$ mJy, respectively. The right panel displays source C8. Flux densities for the Eastern and Western lobes are $I = 38.8$ mJy and $L = 0.3$ mJy, and $I = 55.4$ mJy and $L = 2.6$ mJy, respectively. Background shading levels in each panel are identical to Fig. 15. Total intensity contours (blue) represent 10, 100, 500, and 1000σ . Linear polarization contours (magenta) represent 6.25, 10, 15, 40, and $90\sigma_{\text{RM}}$.

$\Theta_{\text{max}}(S)$ to be calculated as a weighted average, taking into account spatial variations in both sensitivity and bandwidth smearing (i.e. variations in $\tilde{\sigma}$) over each survey area. The upper limit to each integral gives the maximum value of $\tilde{\sigma}(x, y)$ for any given flux density S , above which not even an ideally unresolved component could be observed above the detection threshold. Therefore, at faint flux densities, the weighted average of observed angular sizes (square root term) is not computed using the full distribution of $\tilde{\sigma}$, but rather a renormalised distribution in which the term in square brackets has value less than unity.

In Fig. 18 we plot the deconvolved angular sizes of ATLAS DR2 components and indicate the locus defined by Equation (22) for each survey area (solid curves). For clarity, we characterise the limiting behaviour of Equation (22) at low and high flux densities by defining two simplified versions of this Equation, which we plot as dotted curves about the solid curve in each panel of

Fig. 18. The first of these uses the minimum effective noise $\tilde{\sigma}_{\text{min}} = \min[\tilde{\sigma}(x, y)]$ to characterise the maximum angular size $\Theta_{\text{max}}'(S)$ at all flux densities, given by

$$[\Theta_{\text{max}}'(S)]^2 = \frac{S B_{\text{maj}} B_{\text{min}}}{A_S \tilde{\sigma}_{\text{min}}} - B_{\text{maj}} B_{\text{min}}, \quad (23)$$

where $\tilde{\sigma}_{\text{min}}$ is 24 (14) and 27 (22) $\mu\text{Jy beam}^{-1}$ in the CDF-S and ELAIS-S1 total intensity (polarization) fields, respectively. The second definition uses the full effective noise distribution at all flux densities to evaluate a weighted maximum angular size $\Theta_{\text{max}}''(S)$, given by

$$[\Theta_{\text{max}}''(S)]^2 = \left[\int_0^\infty \sqrt{\frac{S B_{\text{maj}} B_{\text{min}}}{A_S z}} f_{\tilde{\sigma}}(z) dz \right]^2 - B_{\text{maj}} B_{\text{min}}. \quad (24)$$

Equation (22) limits to Equation (23) at faint flux densities and to

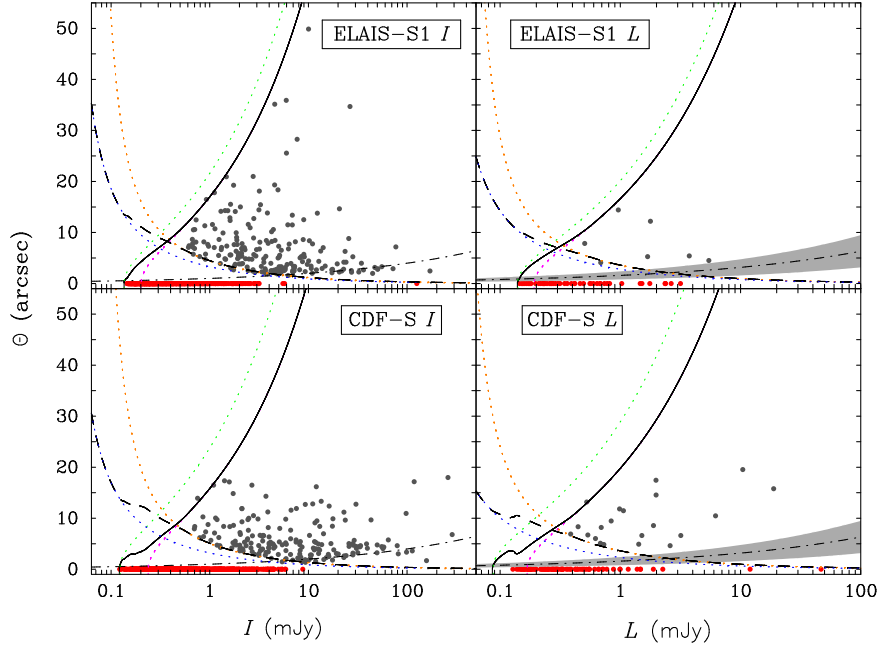


Figure 18. Deconvolved angular size as a function of flux density for ATLAS total intensity (left column) and linearly polarized (right column) components in the ELAIS-S1 (top row) and CDF-S (bottom row) fields. For visual clarity, angular sizes of unresolved components (red points) are displayed at zero, rather than at their upper bounds. The solid curve in each panel indicates the maximum angular size above which a component’s peak surface brightness will drop below the survey detection threshold, as defined by Equation (22). The dashed curve in each panel indicates the minimum angular size required of a component to be classified as resolved and deconvolved, as defined by Equation (33). The dot-dashed curve in each panel indicates the median of the assumed underlying true size distribution, with associated shaded regions in the right panels indicating filling-factor uncertainties; see text in Section 7.1.1 for details. The dotted curves indicate limiting behaviours of the solid and dashed curves, given by Equations (23) (green), (24) (magenta), (34) (blue), and (35) (orange).

Equation (24) at higher flux densities. We note that if $\Theta_{\max}(S)$ were defined using a fixed minimum noise value, as in Equation (23), then maximum angular sizes would in general be overestimated at all flux densities (or underestimated if the maximum noise value was selected). Similarly, if $\Theta_{\max}(S)$ were defined without taking into account the visibility area associated with component detection at faint flux densities, as in Equation (24), then the maximum angular sizes estimated at faint flux densities would be significantly underestimated; the relevant dotted curves in Fig. 18 fall to zero angular size at flux densities higher than the faintest observed ATLAS components, indicating that Equation (24) may not be used to estimate $\Theta_{\max}(S)$ at faint S .

To model the underlying true size distribution for *components* in total intensity, we modified the integral angular size distribution presented by Windhorst, Mathis, & Neuschaefer (1990) for 1.4 GHz *sources*. The Windhorst, Mathis, & Neuschaefer (1990) distribution gives the fraction of sources with largest angular size (LAS) greater than Θ , and is parameterised as

$$h(> \Theta, S) = 2^{-(\Theta/\Theta_{\text{med},I})^{0.62}}, \quad (25)$$

where $\Theta_{\text{med},I}$ is the median LAS as a function of flux density given by $2''0 (S_{1.4\text{GHz}}/1 \text{ mJy})^{0.3}$. The density function corresponding to Equation (25) is

$$f_{\Theta}(\Theta, S) = \frac{0.62 \ln 2}{\Theta_{\text{med},I}} \left(\frac{\Theta}{\Theta_{\text{med},I}} \right)^{-0.38} h(> \Theta, S). \quad (26)$$

The LAS of a source characterises its largest angular extent. The LAS for a single-component source is given by its deconvolved angular size. The LAS for a multi-component source is given by the

maximum angular separation between its components, or if greater, the largest deconvolved angular size of any of its components. We note that, in principle, there are no resolution bias constraints preventing the detection of multi-component sources with arbitrarily large LASs, provided that their individual components are each smaller than Θ_{\max} and thus individually detectable. We modelled the size distribution for total intensity components by retaining the parameterisation presented in Equation (25), but with a modified relationship for $\Theta_{\text{med},I}$ given by

$$\Theta_{\text{med},I} = 1.0'' \left(\frac{S}{1 \text{ mJy}} \right)^{0.3}, \quad (27)$$

where S here denotes component flux density. For a single-component source, Equation (27) predicts a median LAS that is half that predicted by Windhorst, Mathis, & Neuschaefer (1990). Equation (27) is plotted in the left-column panels of Fig. 18; this model appears to be consistent with the observed ATLAS components.

We were motivated to develop Equation (27) by considering the angular size distribution presented by Bondi et al. (2003) for sources in the VLA-VDF survey with flux density $0.4 \leq S < 1.0 \text{ mJy}$. The VLA-VDF survey is similar to ATLAS with an observing frequency of 1.4 GHz, 1 deg^2 field of view, $6''$ synthesised beam FWHM, and $\sim 17 \mu\text{Jy beam}^{-1}$ rms noise. Only 1 VLA-VDF source was found to comprise multiple components in the flux density range above, with all others forming single-component sources. We therefore assumed that the Bondi et al. (2003) size distribution could be used to characterise the true size distribution expected for ATLAS components. To demonstrate why we modified Equa-

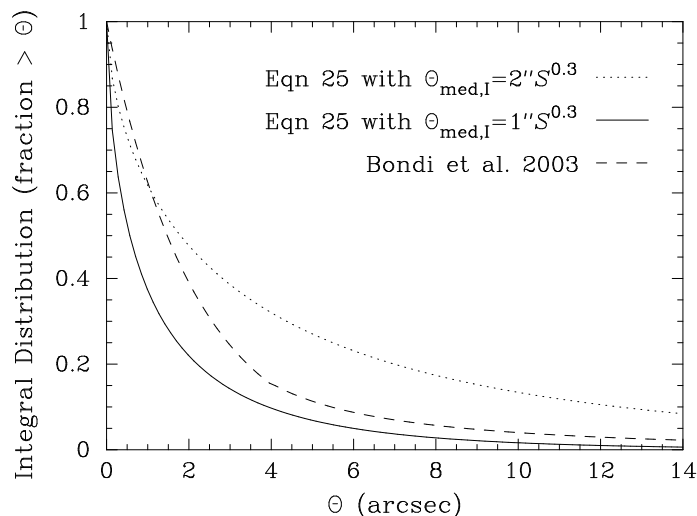


Figure 19. Integral angular size distributions in total intensity. The dashed curve gives the distribution presented by Bondi et al. (2003) for sources with $0.4 \leq S < 1.0$ mJy. The dotted curve gives the distribution for sources presented by Windhorst, Mathis, & Neuschaefer (1990). The solid curve gives our assumed distribution for ATLAS components, obtained following the Windhorst, Mathis, & Neuschaefer (1990) source parameterisation but with assumed median angular sizes reduced by a factor of 2. The solid curve assumes components with $S = 0.7$ mJy, while the dotted curve assumes sources with $S = 0.7$ mJy.

tion (27) as such and why we didn't choose to simply implement the original angular size distributions presented by Bondi et al. (2003) or Windhorst, Mathis, & Neuschaefer (1990), we have plotted each of the distributions in Fig. 19. As shown, the original Windhorst, Mathis, & Neuschaefer (1990) distribution over-predicts a substantial tail of sources with angular sizes greater than those observed and in turn modelled by Bondi et al. (2003). Our modified distribution, using Equation (25) with $\Theta_{\text{med},I}$ given by Equation (27), successfully reproduces the Bondi et al. (2003) model for component sizes $\gtrsim 3''$. However, our modified distribution predicts a greater proportion of components with sizes $< 3''$ than the Bondi et al. (2003) model. To suggest a possible explanation for this discrepancy and provide a rudimentary justification for our assumed size distribution, we note that Bondi et al. (2003) did not account for bandwidth smearing across their mosaicked data. As a result, it is likely that their results were biased against the detection of sources with small angular sizes. For example, assuming a beam FWHM of $6''$, a source with $0''.5$ true angular size would be observed in the absence of bandwidth smearing to have a size of $6''.02$. But if smearing was present at the level of 4%, as may be representative of the VLA-VDF data (recall discussion of bandwidth smearing in a mosaic from Section 4.2), then the observed and deconvolved angular sizes would be $6''.02/\sqrt{0.96}$ and $1''.3$, respectively. Regardless of true size, no source with deconvolved angular size $< 1''.22$ could be observed in this scenario. This artificial size inflation would diminish for sources with true angular sizes approaching the beam FWHM. For example, a source with $3''$ true angular size would be observed to have a deconvolved angular size of $3''.3$ if uncorrected for bandwidth smearing. While it is likely that the true underlying angular size distribution for components (or single-component sources) lies somewhere between the solid and dashed curves in Fig. 19, the key requirement of our assumed distribution in this work is that it can characterise populations of components with sizes $> 3''$. From the left column panels of Fig. 18 we find that $\Theta_{\text{max}}(S)$ does not fall below $3''$ until $S < 0.2$ mJy. Therefore, very

few flux density bins are likely to be significantly affected if our assumed true size distribution for $\Theta < 3''$ is in error.

To our knowledge, the true underlying size distribution for 1.4 GHz components in linear polarization surveys such as ATLAS with $\sim 10''$ resolution has not yet been explored. Given the small fraction of polarized components observed as resolved in our data (see Fig. 18), we were unable to directly investigate this distribution in a robust empirical manner. Instead, to obtain the polarized size distribution, we first assumed that angular sizes of polarized components could be related to their total intensity angular sizes using a filling factor η , independent of flux density; i.e. $\Theta_L = \eta\Theta_I$ where Θ_L and Θ_I are a component's deconvolved linear polarization and total intensity angular sizes, respectively. To estimate an appropriate model value for the angular filling factor, we evaluated the ratio Θ_L/Θ_I for all resolved total intensity components in ATLAS, as shown in Fig. 20. Approximate errors for this ratio were calculated following standard error propagation as

$$\sigma_\eta \approx \frac{\Theta_L}{\Theta_I} \sqrt{\left(\frac{\sigma_{\Theta_L}}{\Theta_L}\right)^2 + \left(\frac{\sigma_{\Theta_I}}{\Theta_I}\right)^2}, \quad (28)$$

with angular size uncertainties from Equation (12). Angular filling factor upper bounds for the total intensity components with an unresolved polarization counterpart, η_u , were obtained by combining Equations (9) and (10) to estimate the maximum value of Θ_L that a polarized component could attain before being classified as resolved, namely

$$\eta_u = \min \left(1, \frac{1}{\Theta_I} \sqrt{B_{\text{maj}} B_{\text{min}} \left\{ a^{-b/[L_{\text{peak}}^{\text{FOD}}/\bar{\sigma}(x,y)]^c} - 1 \right\}} \right), \quad (29)$$

where factors greater than 1 were not allowed. We note that the ATLAS components with $\eta > 1$ in Fig. 20 are diffuse in total intensity and thus poorly characterised by a 2D elliptical Gaussian, resulting in underestimated values of Θ_I and thus overestimated values of η .

To model the distribution of components and upper bounds shown in Fig. 20, we assumed that η may be characterised by a

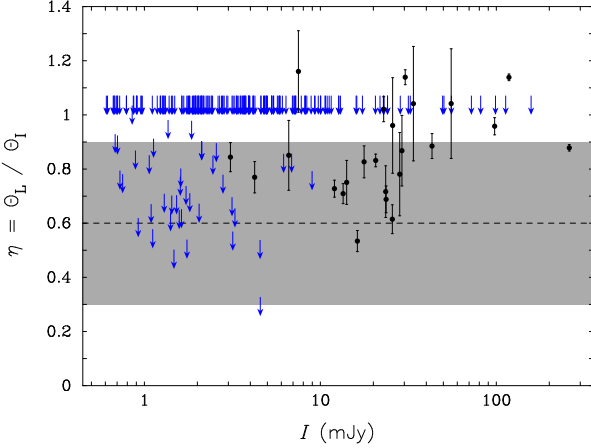


Figure 20. Angular filling factor, η , for polarized emission within resolved total intensity components in ATLAS. Upper bounds have been calculated using Equation (29). The dashed line and shaded region represent the fixed value of η_{model} and its associated uncertainty range as given by Equation (30).

constant value with an uncertainty range, rather than a distribution of values as likely to be more appropriate in reality. We conservatively modelled the angular filling factor as

$$\eta_{\text{model}} = 0.6 \pm 0.3, \quad (30)$$

as indicated by the dashed line and shading in Fig. 20. To model the distribution of median angular sizes for linearly polarized components, which we denote by $\Theta_{\text{med,L}}$, we multiplied the distribution of total intensity median angular sizes from Equation (27) by 0.3, 0.6, or 0.9 following Equation (30), and convolved each of the three resulting curves by the fractional polarization distribution from Equation (19). The resulting predicted $\Theta_{\text{med,L}}$ and its uncertainty range are displayed in the right-column panels of Fig. 18; our polarization model appears to be consistent with the observed size distribution of ATLAS components, taking into account the increased presence of unresolved components towards faint flux densities. Finally, we made the largely unjustified assumption that the angular size distribution for polarized components could be modelled using the same parameterisation presented for total intensity in Equation (25), with $\Theta_{\text{med,L}}$ replaced by $\Theta_{\text{med,L}}$. The distribution of polarized components exhibited in Fig. 18 does not refute this assumption, though future high resolution studies are clearly required to support it. We note that for simplicity, and to avoid placing too much emphasis on the exact form of the total intensity angular size density function from Equation (26), we did not estimate $\Theta_{\text{med,L}}$ above by first convolving Equation (26) with the fractional polarization distribution from Equation (19). This more standard computational path should be utilised once the total intensity angular size distribution for components is known with greater confidence.

We predicted the differential number-counts for detectable components [those with angular sizes $\leq \Theta_{\text{max}}(S)$] by evaluating Equation (25) with Equation (22) for each total intensity and linear polarization ATLAS field, namely

$$\frac{dN_{\text{detectable}}}{dS}(S) = \frac{dN_{\text{true}}}{dS}(S) \{1 - h[> \Theta_{\text{max}}(S), S]\}. \quad (31)$$

Equation (31) is displayed in Fig. 21 (dashed curves), assuming true differential component counts (solid green curves) modelled in total intensity by the H03 distribution from Equation (15) and

in linear polarization by the H03 * $f_{\Pi}(\Pi)$ distribution from Section 5.4. The correction to account for the first form of resolution bias, regarding incompleteness to resolved components, is then

$$r_{\text{effect-1}}(S) = \frac{dN_{\text{detectable}}}{dS}(S) \div \frac{dN_{\text{true}}}{dS}(S). \quad (32)$$

Equation (32) is displayed in Fig. 22 for each ATLAS field.

7.1.2 Effect 2: Flux Density Undervaluation for Unresolved Components

We accounted for the second form of resolution bias, regarding the undervaluation of flux densities for components classified as unresolved, as follows.

First, we estimated the minimum intrinsic angular size required for a component to be classified as resolved, $\Theta_{\text{min}}(S)$, following a similar formalism to that described earlier for $\Theta_{\text{max}}(S)$. By relating Equation (9) with Equation (10), we obtained

$$[\Theta_{\text{min}}(S)]^2 = \left\{ \int_0^{S/A_S} B_{\text{maj}} B_{\text{min}} a^{-b/(S/z)^c} f_{\bar{\sigma}}(z) dz \times \left[\int_0^{S/A_S} f_{\bar{\sigma}}(z') dz' \right]^{-1} \right\}^2 - B_{\text{maj}} B_{\text{min}}. \quad (33)$$

Similar to the relationships between Equation (22) and Equations (23) and (24), the limiting behaviours of Equation (33) at low and high flux densities are given by

$$[\Theta_{\text{min}'}(S)]^2 = B_{\text{maj}} B_{\text{min}} a^{-b/(S/\bar{\sigma}_{\text{min}})^c} - B_{\text{maj}} B_{\text{min}}, \quad (34)$$

and

$$[\Theta_{\text{min}''}(S)]^2 = \left[\int_0^{\infty} B_{\text{maj}} B_{\text{min}} a^{-b/(S/z)^c} f_{\bar{\sigma}}(z) dz \right]^2 - B_{\text{maj}} B_{\text{min}}, \quad (35)$$

respectively. The locus defined by Equation (33) is indicated by a dashed curve for each ATLAS field in Fig. 18. These curves are bounded by Equations (34) and (35), as indicated by the relevant dotted curves.

Next, we predicted the differential number-counts for detectable components classified as resolved by evaluating

$$\begin{aligned} \frac{dN_{\text{resolved}}}{dS}(S) &= \frac{dN_{\text{detectable}}}{dS}(S) \times \\ & \quad (h\{> \min[\Theta_{\text{min}}(S), \Theta_{\text{max}}(S)], S\} - \\ & \quad h[> \Theta_{\text{max}}(S), S]) \div \\ & \quad (1 - h[> \Theta_{\text{max}}(S), S]). \end{aligned} \quad (36)$$

We will assume that observed flux densities for resolved components are equal to their true flux densities. The predicted counts for detectable components classified as unresolved are

$$\frac{dN_{\text{unresolved}}}{dS}(S) = \frac{dN_{\text{detectable}}}{dS}(S) - \frac{dN_{\text{resolved}}}{dS}(S). \quad (37)$$

Equations (36) and (37) are displayed in Fig. 21 (dot-dashed and dotted curves, respectively).

If measurement errors were zero, flux densities for unresolved components could be obtained from observation of their integrated surface brightnesses. The observed differential counts for these unresolved components would then match the $dN_{\text{unresolved}}/dS$ curves. In reality, however, their flux densities are set by their peak surface brightnesses assuming zero intrinsic angular size, resulting in the redistribution of component counts from any given flux density

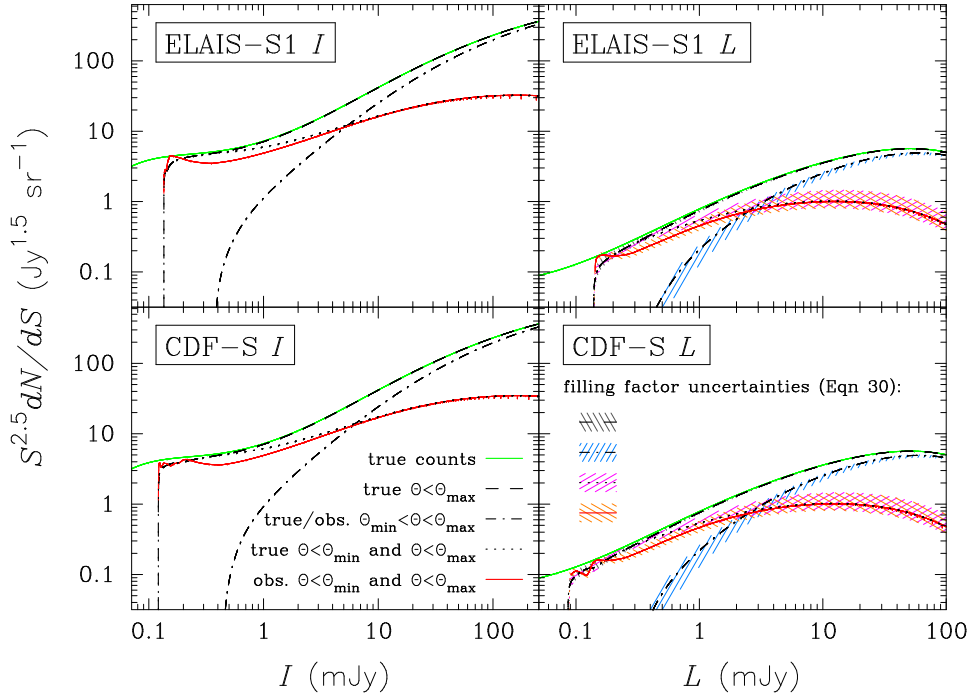


Figure 21. Modelled effects of resolution bias on differential component counts in total intensity (left column) and linear polarization (right column). The green curves show the assumed true underlying counts, given by the H03 distribution in total intensity [Equation (15)] and the H03 $\ast f_{\text{II}}$ (II) distribution in linear polarization (see Section 5.4). The dashed curves show the counts for detectable components [Equation (31)]. The dot-dashed curves show the counts for detectable components classified as resolved [Equation (36)]. The dotted curves show the counts for detectable components classified as unresolved, for a scenario where measurement systematics are zero [Equation (37)]. The red curves show the counts for detectable components classified as unresolved, for a realistic scenario where measurement systematics are taken into account [Equation (38)]. The shaded regions in the right panels represent the propagation of angular filling factor uncertainties [Equation (30)].

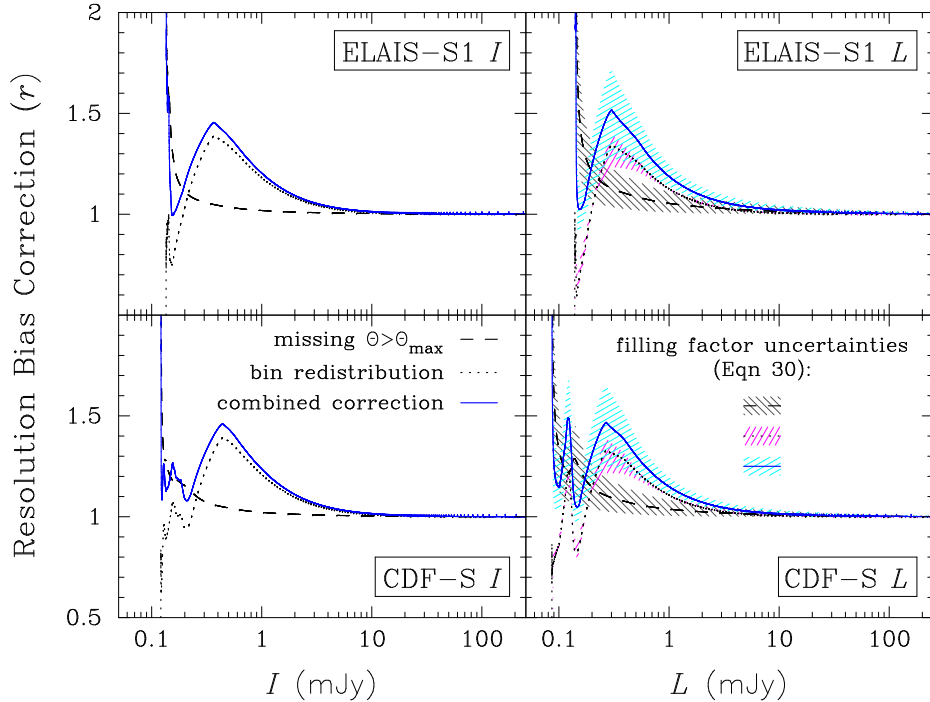


Figure 22. Resolution bias corrections for incompleteness to resolved components [Equation (32); dashed curves], flux density undervaluation for unresolved components [Equation (41); dotted curves], and the overall combined corrections [Equation (42); blue curves]. The panel layout and details are similar to Fig. 21.

bin to fainter bins because components always have physical non-zero angular sizes. To model this effect and predict the observed distribution of components classified as unresolved, we convolved Equation (37) by a suitably renormalised version of Equation (26), namely

$$\frac{dN_{\text{unresolved-obs}}}{dS}(S) = \int_S^\infty \frac{dN_{\text{unresolved}}}{dS'}(S') H(\tilde{\Theta} - \Theta') \times \frac{f_\Theta(\Theta', S')}{\int_0^{\tilde{\Theta}} f_\Theta(\Theta'', S') d\Theta''} dS', \quad (38)$$

where

$$\Theta' = \sqrt{B_{\text{maj}} B_{\text{min}}} \left(\frac{S'}{S} - 1 \right), \quad (39)$$

$$\tilde{\Theta} = \min[\Theta_{\text{min}}(S'), \Theta_{\text{max}}(S')] , \quad (40)$$

and where $H(x)$ is a unit step function with value unity for argument $x \geq 0$ and zero otherwise. Equation (38) is displayed by the red curve for each ATLAS field in Fig. 21. The wiggles in these curves at faint flux densities are real (i.e. not due to numerical instabilities); they are caused by the behaviour of $\Theta_{\text{max}}(S)$ at faint flux densities, in turn influenced by the spatial distribution of rms noise and bandwidth smearing in the ATLAS mosaics.

The correction to account for the second form of resolution bias was then calculated as

$$r_{\text{effect-2}}(S) = \frac{dN_{\text{detectable}}}{dS}(S) \div \left[\frac{dN_{\text{resolved}}}{dS}(S) + \frac{dN_{\text{unresolved-obs}}}{dS}(S) \right]. \quad (41)$$

This correction is shown as the dotted curve for each ATLAS field in Fig. 22.

We note that the form of resolution bias investigated in this section is only relevant for measurement schemes that use peak surface brightness as a proxy for unresolved component flux density (mostly relevant at low SNR; e.g. see Fig. 13; see also Schinnerer et al. 2010). The alternative is to use integrated surface brightness measurements for both unresolved and resolved components. However, such schemes will exhibit new and more significant biases in recovered flux densities at low and even moderate SNRs due to both increased statistical errors from the larger number of free parameters required to obtain an integrated measurement compared to a peak measurement (relevant to both 2D elliptical Gaussian and flood-fill fits; see Fig. 6 in Hales et al. 2012b), and increased systematic flux density errors (particularly relevant for Gaussian fits; see Fig. 6 in Hales et al. 2012b).

7.1.3 Combined Correction

The overall resolution bias correction factors for ATLAS DR2 were calculated by multiplying Equations (32) and (41) together,

$$r(S) = r_{\text{effect-1}}(S) r_{\text{effect-2}}(S). \quad (42)$$

Equation (42) is displayed by the blue curve for each ATLAS field in Fig. 22. For decreasing flux density, the correction factors for each field rise to a peak due to increasing incompleteness, fall due to the redistribution of components classified as unresolved, and then rise again at the faintest levels as incompleteness again dominates the correction (the correction rises to infinity at levels below the faintest flux density bin because the number of detectable components drops to zero). The blue curves in Fig. 22 are consistent with the results from Monte Carlo simulations presented by

Bondi et al. (2008), who found that resolution bias correction factors were not maximised for the faintest flux density bin, but rather for a higher flux density bin due to combination of the two effects described above.

Prandoni et al. (2001) and Huynh et al. (2005) have derived resolution bias correction factors exhibiting similar rise-fall behaviour to that presented by Bondi et al. (2008) and this work. Their solutions were obtained by only considering the first form of resolution bias considered in this work, regarding reduced sensitivity to resolved components. To obtain their solutions, Prandoni et al. (2001) and Huynh et al. (2005) described the use of Equations (34) or (35) [i.e. equations representing $\Theta_{\text{min}}(S)$], respectively, in characterising $\Theta_{\text{max}}(S)$ at the faintest flux densities probed by their data. Given that $\Theta_{\text{min}}(S)$ rises with decreasing flux density, eventually becoming larger than $\Theta_{\text{max}}(S)$, their resolution bias corrections were found to rise and then fall with decreasing flux density. However, their procedure is not suitable; $\Theta_{\text{max}}(S)$ represents a strict limit to the angular size of detectable components, regardless of the size of $\Theta_{\text{min}}(S)$ which dictates whether a *detected* component will be classified as unresolved or resolved.

7.2 Eddington Bias

As described in Section 5.4, random measurement errors in the presence of a non-uniformly distributed component population will redistribute components between number-count flux density bins, resulting in Eddington bias (Eddington 1913; Jeffreys 1938; Eddington 1940). We accounted for Eddington bias by considering two alternative correction schemes.

For the first method, we computed Equation (21) using the deboosted flux densities from Section 5.4, with e_i set to unity. The deboosting equations presented in Section 5.4 offer a simple approach for mitigating Eddington bias prior to the construction of differential component counts. However, these equations do not account for spatial variations in rms noise or bandwidth smearing, nor do they properly account for variations in number-count slope (γ). To account for such specifics we considered an alternative correction scheme similar to that proposed by Eddington (1913), focusing on correction factors e_i for bin counts involving raw component flux densities rather than deboosted values. We now describe this second method.

Given an observed noise distribution and an assumed underlying true component count distribution, the observed counts can be predicted (e.g. Simpson et al. 2006). The ratio between the predicted and true distributions gives the Eddington bias; the correction factors e_i are therefore given by the reciprocal of this ratio. We modelled the predicted (i.e. biased) counts in total intensity, which we denote by dN_{Edd}/dS , by assuming that the underlying counts were distributed according to the H03 model. We assess the suitability of this assumption in Section 2.3 of Paper II. By accounting for the proportion of components with true flux density $S + \epsilon$ that may be observed with flux density S due to Gaussian measurement error $-\epsilon$, we have

$$\frac{dN_{\text{Edd}}}{dS}(S) = \int_{-\infty}^{\infty} \int_0^{z''} \frac{1}{\sqrt{2\pi}} \exp\left(-\frac{\xi^2}{2}\right) \times \frac{dN_{\text{H03}}}{dS}(S + \xi z) \frac{f_{\bar{\sigma}}(z)}{\int_0^{z''} f_{\bar{\sigma}}(z') dz'} dz d\xi, \quad (43)$$

where

$$z'' = \begin{cases} -S/\xi & \text{if } \xi < 0 \\ \infty & \text{if } \xi \geq 0, \end{cases} \quad (44)$$

and $f_{\bar{\sigma}}$ is the effective noise distribution for each ATLAS field taking into account bandwidth smearing (as introduced in Section 7.1). The parameter z'' prevents the argument to dN_{H03}/dS from becoming negative (i.e. unphysical). To obtain a similar relationship for the predicted counts in linear polarization, which we denote dN_{Edd}/dL , we replaced the Gaussian error distribution from Equation (43) by the distribution for L_{RM} given by Equation (28) from Hales et al. (2012a). Assuming an underlying dN/dL distribution given by the $\text{H03} * f_{\Pi}(\Pi)$ model introduced in Section 5.4, we obtained

$$\frac{dN_{\text{Edd}}}{dL}(S) = \int_{-\infty}^{\infty} \int_0^{z''} f(L_{\text{RM}} = S \mid M = 28, L_0 = S + \xi z, \sigma_{\text{RM}} = z) \times \frac{dN_{\text{H03}*f_{\Pi}(\Pi)}}{dL}(S + \xi z) \times \frac{f_{\bar{\sigma}}(z)}{\int_0^{z''} f_{\bar{\sigma}}(z') dz'} dz d\xi, \quad (45)$$

where

$$z'' = \begin{cases} -S/\xi & \text{if } \xi < 0 \\ \infty & \text{if } \xi \geq 0, \end{cases} \quad (46)$$

and $f(L_{\text{RM}} \mid M, L_0, \sigma_{\text{RM}})$ is the PDF for L_{RM} given M , L_0 , and σ_{RM} .

In Fig. 23 we display Equations (43) and (45), their assumed underlying count distributions, and the resulting Eddington biases for each ATLAS field; these are indicated by the black curves. As expected, we find that Eddington bias becomes stronger with decreasing flux density in both total intensity and linear polarization. Deviations from this general trend are observed for the faintest flux density bins, predominantly due to the changing slope of the counts in total intensity, and to the positive-semidefinite and non-Gaussian nature of noise fluctuations in polarization. The positive nature of polarization measurements largely prevents components with low-SNR from having their flux densities underestimated (e.g. see the effective noise distribution presented in the lower panel of Fig. 1 in Hales et al. 2012a), in turn causing the faintest polarized counts to be underestimated.

For the purpose of illustration, following Section 5.4 we also predicted the Eddington bias that would be exhibited if the true underlying counts were described by the H03M model. The results in total intensity are displayed as magenta curves in Fig. 23; polarization results are not shown as they are identical to the H03 results over the flux density range displayed. Our approach of modelling the underlying counts in order to compare with the observed counts is similar to the forward modelling described by Macquart et al. (2012). However, unlike their work, our Eddington bias calculations take into account a more suitable statistical form to describe L_{RM} (see discussion in Hales et al. 2012a).

We now make some remarks about our Eddington bias calculations. Like the deboosting relationship for linear polarization presented in Equation (18), Equation (45) performs implicit polarization debiasing. However, their treatments differ: Equation (18) assumes Ricean statistics for simplicity, whereas Equation (45) incorporates the full PDF for L_{RM} .

Ideally, the Eddington bias corrections presented in Equations (43) and (45) require underlying count distributions that represent unresolved components, and not all components as implemented here (note that this distinction was made for our deboosting corrections in Section 5.4). Our solutions above implicitly assume that all components are unresolved, such that their true peak surface

brightnesses may be perturbed by noise fluctuations, in turn directly perturbing their observed flux densities. However, this simplification in our analysis is unlikely to result in any significant systematics, because the flux density range over which significant Eddington bias is observed in Fig. 23 consists overwhelmingly of unresolved components (see Fig. 21). In the future, a potential refinement may be to combine both the resolution and Eddington bias corrections, rather than splitting them as presented in this work.

Finally, we note that Equation (45) and thus our Eddington bias predictions may be inaccurate for two reasons. First, our treatment of the correlation between the error distribution and the underlying signal may not include all nuisance parameters. Second, the Eddington bias predictions for our data are relatively small, which is perhaps unusual given the non-Gaussian PDF for L_{RM} . However, as will be demonstrated in Paper II, differences between the two independent Eddington bias correction schemes described above are largely negligible when applied to both the total intensity and linear polarization number-counts, providing confidence in both approaches.

8 RESULTS

8.1 Mosaics

Figs. 24–27 display the total intensity and linear polarization mosaicked images of the CDF-S and ELAIS-S1 ATLAS fields. Residual sidelobes are observed around strong sources in the total intensity images, giving rise to minor residual polarization leakage about these sources in the polarization images. Residual sidelobes remaining after cleaning are observed in the south-east quadrant of the total intensity ELAIS-S1 field (Fig. 26), which originate from the 3.8 Jy source PKS B0039–445 outside the field of view. The random pattern of pixels with zero intensity in the polarization images is an artefact of our data processing (difficult to see in printed images; look to field edges where intensity contrast is greatest). This pattern was caused by an error recognition scheme we implemented during the RM cleaning stage, in which we automatically set Equation (1) to zero if the maximum polarized intensity was located at $\pm\phi_{\text{max}}$. Thus ~ 1 in 800 pixels was artificially set to zero. We note that this scheme did not affect subsequent data analysis.

8.2 Component and Source Catalogues

The ATLAS 1.4 GHz DR2 component catalogue is presented in Appendix A. This catalogue lists a total of 2588 components in total intensity and linear polarization; no components were detected in circular polarization.

The ATLAS 1.4 GHz DR2 source catalogue is presented in Appendix B. This catalogue lists a total of 2221 sources as identified through the cross-identification and classification schemes presented in Section 6.

9 CONCLUSION

We have presented data reduction and analysis procedures for the second data release of the Australia Telescope Large Area Survey. We produced and analysed sensitive 1.4 GHz images of the CDF-S and ELAIS-S1 regions across a combined area of 6.392 deg^2

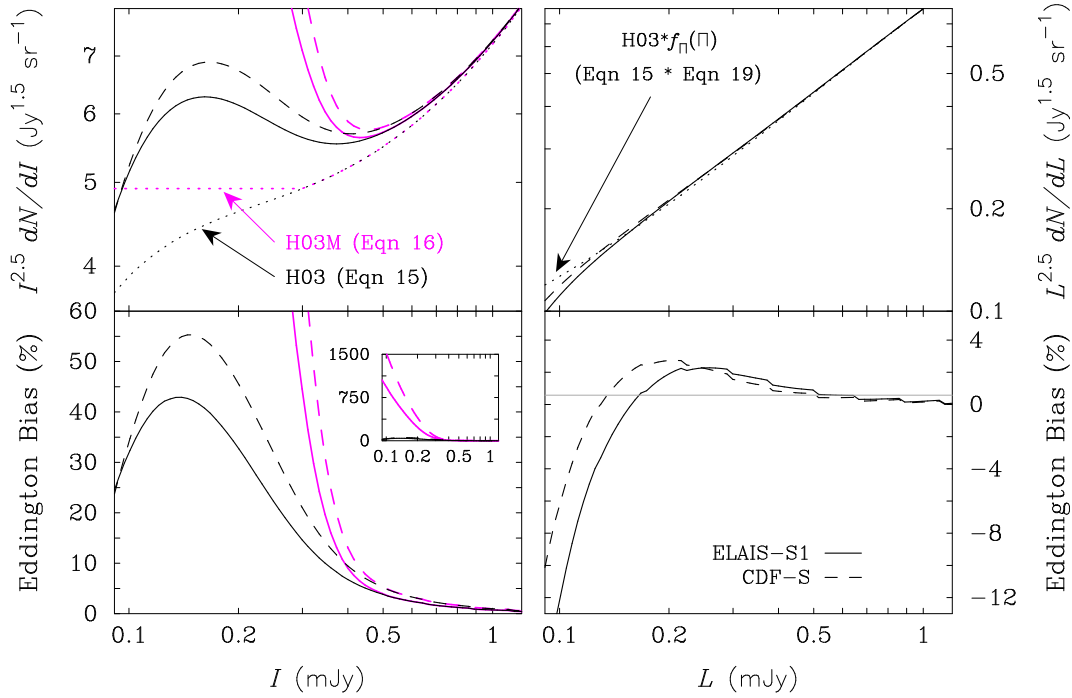


Figure 23. Modelled effects of Eddington bias on differential component counts in total intensity (left column) and linear polarization (right column). Upper panels display predicted counts for each ATLAS field (solid or dashed curves) assuming true underlying count distributions given by the H03 (dotted black) or H03M (dotted magenta) models. Polarization results utilising the H03M model are not shown, as they are identical to the H03 results over the flux density range shown. Curves in the lower panels indicate the percentages by which the predicted distributions overestimate the underlying distributions.

in total intensity (I), linear polarization (L), and circular polarization (V). The data for L were processed using RM synthesis and RM clean. Typical sensitivities across each of the mosaicked multi-pointing images are $\sim 30 \mu\text{Jy beam}^{-1}$, falling to $< 25 \mu\text{Jy beam}^{-1}$ within smaller areas. The typical spatial resolutions are $12'' \times 6''$.

We performed component detection and extraction independently in I , L , and V using a combination of **BLOBCAT** and **IMFIT**, accounting for spatial variations in image sensitivity, bandwidth smearing and instrumental polarization leakage. Corrections for clean bias were not required, due to our implemented cleaning strategy. ATLAS DR2 is the first survey to have been analysed using **BLOBCAT**. We catalogued a total of 2416, 172, and 0 components in I , L , and V , respectively, and determined flux densities for each of these components by considering their angular sizes. We catalogued 2221 sources by matching single or multiple I components with SWIRE mid-infrared sources, and by matching L components to their I counterparts. We classified these sources as AGNs, SFGs, or stars according to four diagnostic criteria. Our source catalogue is slightly biased against the detection of multi-component sources due to our nearest-neighbour cross-identification method, and toward the classification of AGNs due to lack of optical spectroscopy for the majority of sources.

We presented a comprehensive prescription for handling multi-pointing data consistently in both total intensity and linear polarization. We described our data reduction and analysis procedures in detail in order to inform future surveys and to highlight our novel extensions of processing techniques from total intensity to linear polarization. We developed new analytic techniques to account for bandwidth smearing with a non-circular beam, and resolution bias in differential number-counts. We extended the analytic

framework for Eddington bias corrections from total intensity to linear polarization.

In Paper II we present the ATLAS DR2 cross-identification and number-count results, and discuss statistics of the faint polarized 1.4 GHz sky.

ACKNOWLEDGMENTS

We thank the following for helpful discussions and support: Julie Banfield, Mark Calabretta, Chris Carilli, Tim Cornwell, Ron Ekers, Juliana Kwan, Tim Robishaw, Bob Sault, Nick Seymour, Chris Simpson, Rogier Windhorst, and Peter Zinn. We thank the anonymous referee for their comprehensive review of the manuscript and helpful comments. C. A. H. acknowledges the support of an Australian Postgraduate Award, a CSIRO OCE Scholarship, and a Jansky Fellowship from the National Radio Astronomy Observatory. B. M. G. and R. P. N. acknowledge the support of the Australian Research Council Centre of Excellence for All-sky Astrophysics (CAASTRO), through project number CE110001020. The Australia Telescope Compact Array is part of the Australia Telescope National Facility which is funded by the Commonwealth of Australia for operation as a National Facility managed by CSIRO. This paper includes archived data obtained through the Australia Telescope Online Archive (<http://atoa.atnf.csiro.au>).

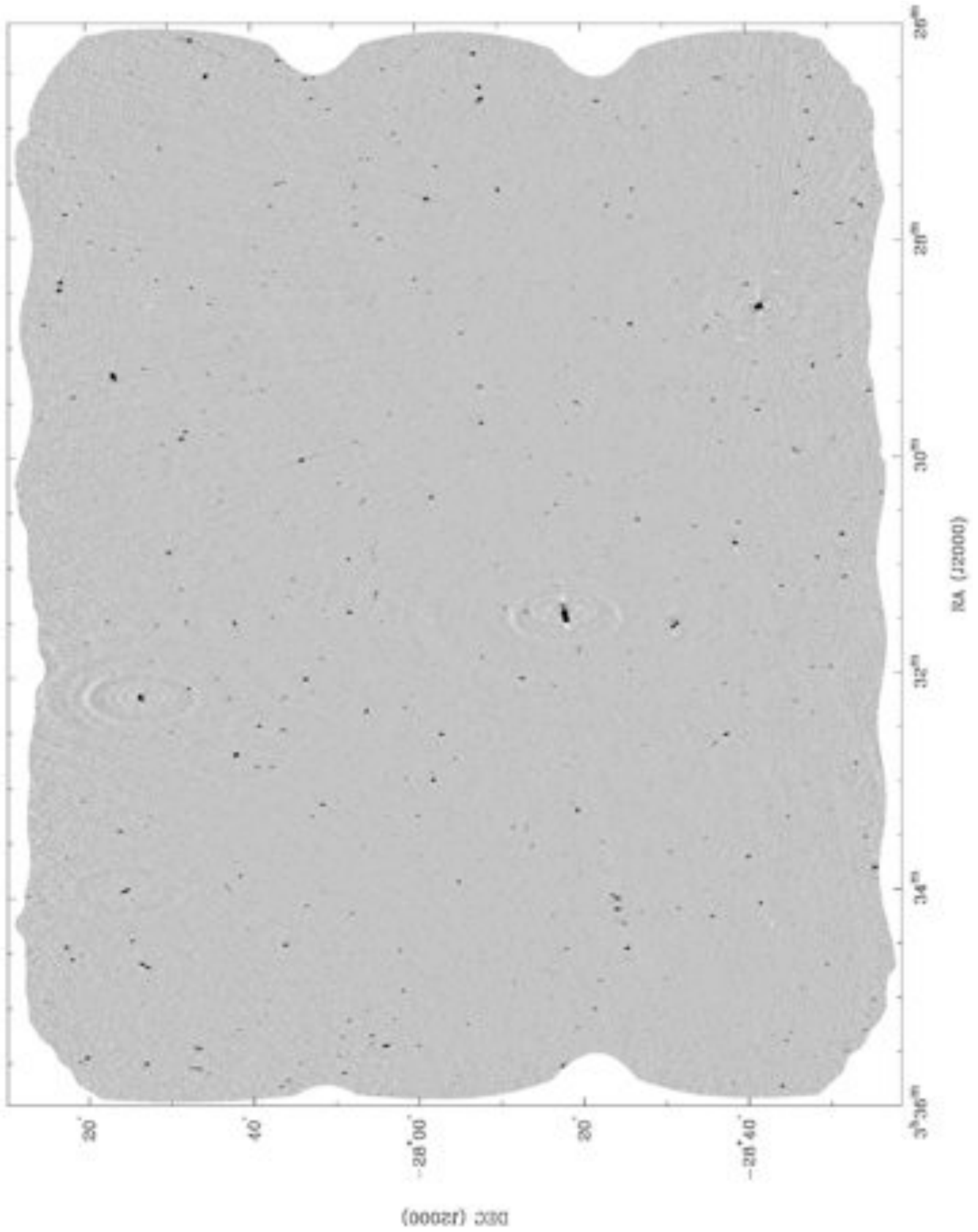


Figure 24. 1.4 GHz total intensity mosaic (I_{MFS}) of the CDF-S ATLAS field in zenithal equal-area projection at a resolution of $13''.0 \times 6''.0$. The peak surface brightness is $0.89 \text{ Jy beam}^{-1}$ and the typical rms noise is $40 \mu\text{Jy beam}^{-1}$. The intensity scale is linear, saturating white below $-0.3 \text{ mJy beam}^{-1}$ and black above 1 mJy beam^{-1} .

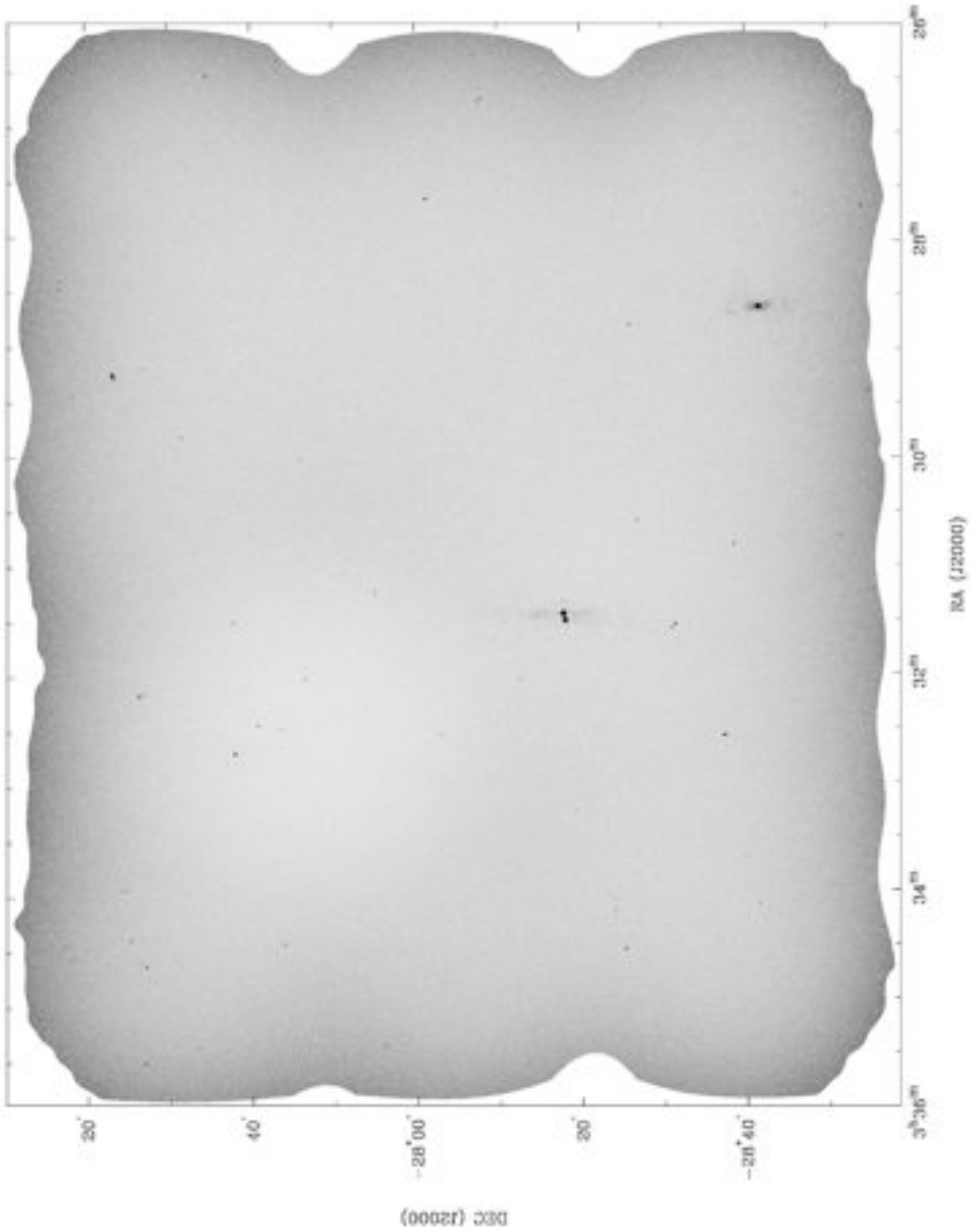


Figure 25. 1.4 GHz leakage-corrected linear polarization mosaic (L_{CORR}) of the CDF-S ATLAS field in zenithal equal-area projection at a resolution of $14''.6 \times 5''.4$. The peak surface brightness is 42 mJy beam^{-1} and the typical rms noise is $25 \text{ } \mu\text{Jy beam}^{-1}$. The intensity scale is linear, saturating white at 0 mJy beam^{-1} and black above $0.4 \text{ mJy beam}^{-1}$.

REFERENCES

- Anderson T. W., 1971, *The Statistical Analysis of Time Series*. John Wiley & Sons, New York
- Appleton P. N., et al., 2004, *ApJS*, 154, 147
- Battye R. A., Browne I. W. A., Jackson N., 2008, *MNRAS*, 385, 274
- Beck R., Gaensler B. M., 2004, *NewAR*, 48, 1289
- Beck R., Frick P., Stepanov R., Sokoloff D., 2012, *A&A*, 543, A113
- Bertin E., Arnouts S., 1996, *A&AS*, 117, 393
- Biggs A. D., Ivison R. J., 2006, *MNRAS*, 371, 963
- Biggs A. D., Ivison R. J., 2008, *MNRAS*, 385, 893
- Bilitza D., Reinisch B. W., 2008, *AdSpR*, 42, 599
- Bondi M., Ciliegi P., Schinnerer E., Smolčić V., Jahnke K., Carilli C., Zamorani G., 2008, *ApJ*, 681, 1129
- Bondi M., et al., 2003, *A&A*, 403, 857
- Brentjens M. A., de Bruyn A. G., 2005, *A&A*, 441, 1217
- Bridle A. H., Greisen E. W., 1994, *AIPS Memo No. 87*, NRAO, Charlottesville, VA
- Bridle A. H., Schwab F. R., 1999, *ASPC*, 180, 371
- Calabretta M. R., Greisen E. W., 2002, *A&A*, 395, 1077
- Carilli C. L., Holdaway M. A., 1999, *RaSc*, 34, 817
- Chapman S., Lindzen R. S., 1970, *Atmospheric tides: Thermal and gravitational*. Gordon and Breach, New York
- Condon J. J., 2007, *ASPC*, 380, 189
- Condon J. J., Cotton W. D., Greisen E. W., Yin Q. F., Perley R. A., Taylor G. B., Broderick J. J., 1998, *AJ*, 115, 1693
- Condon J. J., et al., 2012, *ApJ*, 758, 23
- Cotton W. D., 1999, *ASPC*, 180, 111
- Crawford F., 2009, *ApJ*, 692, 887
- de Zotti G., Massardi M., Negrello M., Wall J., 2010, *A&ARv*, 18, 1
- Eddington A. S., 1913, *MNRAS*, 73, 359
- Eddington A. S., Sir, 1940, *MNRAS*, 100, 354
- Fanaroff B. L., Riley J. M., 1974, *MNRAS*, 167, 31P
- Farnsworth D., Rudnick L., Brown S., 2011, *AJ*, 141, 191
- Fazio G. G., et al., 2004, *ApJS*, 154, 10
- Finlay C. C., et al., 2010, *GeoJI*, 183, 1216
- Fletcher A., Shukurov A., 2006, *MNRAS*, 371, L21
- Fomalont E. B., Kellermann K. I., Cowie L. L., Capak P., Barger A. J., Partridge R. B., Windhorst R. A., Richards E. A., 2006, *ApJS*, 167, 103
- Forster J. R., 1983, *Overall Systems Performance & Operation—File Notes No. 20.1/006*, Australia Telescope National Facility
- Frater R. H., Brooks J. W., Whiteoak J. B., 1992, *JEEEA*, 12, 103
- Garrington S. T., Leahy J. P., Conway R. G., Laing R. A., 1988, *Natur*, 331, 147
- Giavalisco M., et al., 2004, *ApJ*, 600, L93
- Grant J. K., Taylor A. R., Stil J. M., Landecker T. L., Kothes R., Ransom R. R., Scott D., 2010, *ApJ*, 714, 1689
- Hales C. A., Gaensler B. M., Norris R. P., Middelberg E., 2012a, *MNRAS*, 424, 2160
- Hales C. A., Murphy T., Curran J. R., Middelberg E., Gaensler B. M., Norris R. P., 2012b, *MNRAS*, 425, 979
- Hales C. A., Norris R. P., Gaensler B. M., Middelberg E., 2014 (Paper II), *MNRAS*, xxx, xxx
- Heald G., Braun R., Edmonds R., 2009, *A&A*, 503, 409
- Helou G., Soifer B. T., Rowan-Robinson M., 1985, *ApJ*, 298, L7
- Heywood I., Jarvis M. J., Condon J. J., 2013, *MNRAS*, 432, 2625
- Hogg D. W., Turner E. L., 1998, *PASP*, 110, 727
- Holwerda B. W., 2005, *astro*, arXiv:astro-ph/0512139
- Hopkins A. M., Afonso J., Chan B., Cram L. E., Georgakakis A., Mobasher B., 2003, *AJ*, 125, 465
- Huynh M. T., Jackson C. A., Norris R. P., Prandoni I., 2005, *AJ*, 130, 1373
- Ibar E., Ivison R. J., Biggs A. D., Lal D. V., Best P. N., Green D. A., 2009, *MNRAS*, 397, 281
- Ivison R. J., et al., 2010, *A&A*, 518, L31
- Jauncey D. L., 1968, *ApJ*, 152, 647
- Jeffreys H., 1938, *MNRAS*, 98, 190
- Johnson N. L., Kotz S., 1970, *Distributions in Statistics: Continuous Univariate Distributions—I*. Houghton Mifflin, New York
- Kashyap V. L., van Dyk D. A., Connors A., Freeman P. E., Siemiginowska A., Xu J., Zezas A., 2010, *ApJ*, 719, 900
- Kellermann K. I., 1964, *ApJ*, 140, 969
- Killeen J. E. B., 1996, *AT Technical Document Series No. 39.3/057*, Australia Telescope National Facility
- Koekemoer A. M., Mobasher B., Norris R. P., 2003, *NewAR*, 47, 391
- Lacki B. C., Thompson T. A., Quataert E., 2010, *ApJ*, 717, 1
- Lacy M., et al., 2004, *ApJS*, 154, 166
- Laing R. A., 1988, *Natur*, 331, 149
- Lay O. P., 1997, *A&AS*, 122, 535
- Leahy P., Fernini I., 1989, *VLA Scientific Memorandum No. 161*, NRAO
- Lehmer B. D., et al., 2005, *ApJS*, 161, 21
- Lewis I. J., et al., 2002, *MNRAS*, 333, 279
- Longair M. S., 1966, *MNRAS*, 133, 421
- Lonsdale C. J., et al., 2003, *PASP*, 115, 897
- Lortet M.-C., Borde S., Ochsenbein F., 1994, *A&AS*, 107, 193
- Luo B., et al., 2008, *ApJS*, 179, 19
- Machalski J., Condon J. J., 1999, *ApJS*, 123, 41
- Macquart J.-P., Ekers R. D., Feain I., Johnston-Hollitt M., 2012, *ApJ*, 750, 139
- Magliocchetti M., Maddox S. J., Lahav O., Wall J. V., 1998, *MNRAS*, 300, 257
- Mao M. Y., Huynh M. T., Norris R. P., Dickinson M., Frayer D., Helou G., Monkiewicz J. A., 2011, *ApJ*, 731, 79
- Mao M. Y., et al., 2012, *MNRAS*, 426, 3334
- Mesa D., Baccigalupi C., De Zotti G., Gregorini L., Mack K.-H., Vigotti M., Klein U., 2002, *A&A*, 396, 463
- Middelberg E., 2006, *PASA*, 23, 64
- Middelberg E., et al., 2008, *AJ*, 135, 1276
- Morrison G. E., Owen F. N., Dickinson M., Ivison R. J., Ibar E., 2010, *ApJS*, 188, 178
- Muxlow T. W. B., et al., 2005, *MNRAS*, 358, 1159
- Muxlow T. W. B., Wilkinson P. N., Richards A. M. S., Kellermann K. I., Richards E. A., Garrett M. A., 1999, *NewAR*, 43, 623
- Norris R. P., et al., 2006, *AJ*, 132, 2409
- Norris R. P., et al., 2013, *PASA*, 30, 20
- O’Sullivan S., Stil J., Taylor A. R., Ricci R., Grant J. K., Shorten K., 2008, in *POS, Proc. 9th Eur. VLBI Network Symp. for Radio Astron.*, p. 107
- Owen F. N., Morrison G. E., 2008, *AJ*, 136, 1889
- Padovani P., Miller N., Kellermann K. I., Mainieri V., Rosati P., Tozzi P., 2011, *ApJ*, 740, 20
- Perley R. A., 1999, *ASPC*, 180, 383
- Prandoni I., Gregorini L., Parma P., de Ruiter H. R., Vettolani G., Wieringa M. H., Ekers R. D., 2000, *A&AS*, 146, 41
- Prandoni I., Gregorini L., Parma P., de Ruiter H. R., Vettolani G., Wieringa M. H., Ekers R. D., 2001, *A&A*, 365, 392
- Rayner D., 2000, *AT Technical Document Series No. 39.3/102*, Australia Telescope National Facility

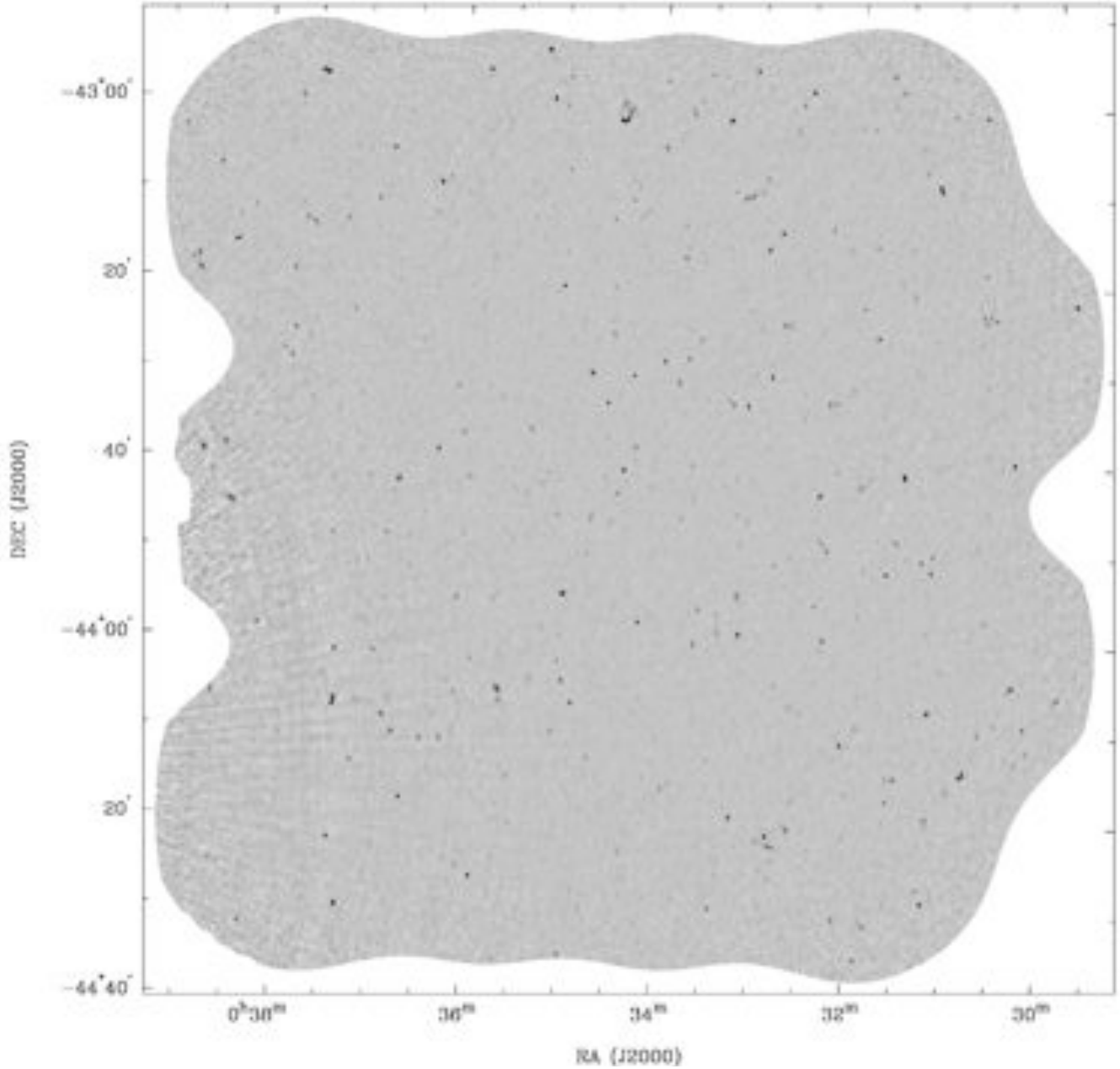


Figure 26. 1.4 GHz total intensity mosaic (I_{MFS}) of the ELAIS-S1 ATLAS field in zenithal equal-area projection at a resolution of $9''.6 \times 7''.6$. The peak surface brightness is $0.16 \text{ Jy beam}^{-1}$ and the typical rms noise is $40 \mu\text{Jy beam}^{-1}$. The intensity scale is linear, saturating white below $-0.3 \text{ mJy beam}^{-1}$ and black above 1 mJy beam^{-1} .

Reynolds J., 1994, AT Technical Document Series No. 39.3/040, Australia Telescope National Facility
 Rice S. O., 1945, Bell System Technical Journal, 24, 46; Reprinted by Wax N., 1954, Selected Papers on Noise and Stochastic Processes. Dover Publications, NY, p. 133
 Richards E. A., 2000, ApJ, 533, 611
 Rieke G. H., et al., 2004, ApJS, 154, 25
 Ryle M., 1968, ARA&A, 6, 249
 Sadler E. M., McIntyre V. J., Jackson C. A., Cannon R. D., 1999, PASA, 16, 247
 Sajina A., Lacy M., Scott D., 2005, ApJ, 621, 256
 Sargent M. T., et al., 2010, ApJS, 186, 341

Sargent M. T., et al., 2010, ApJ, 714, L190
 Sault R. J., Killeen N. E. B., Kesteven M. J., 1991, AT Technical Document Series No. 39.3/015, Australia Telescope National Facility
 Sault R. J., 1995, ATCA Off-Axis Polarimetric Response, <http://www.ph.unimelb.edu.au/~rsault/memos.html>
 Sault R. J., Teuben P. J., Wright M. C. H., 1995, ASPC, 77, 433
 Sault R. J., Staveley-Smith L., Brouw W. N., 1996, A&AS, 120, 375
 Schinnerer E., et al., 2010, ApJS, 188, 384
 Seymour N., McHardy I. M., Gunn K. F., 2004, MNRAS, 352, 131

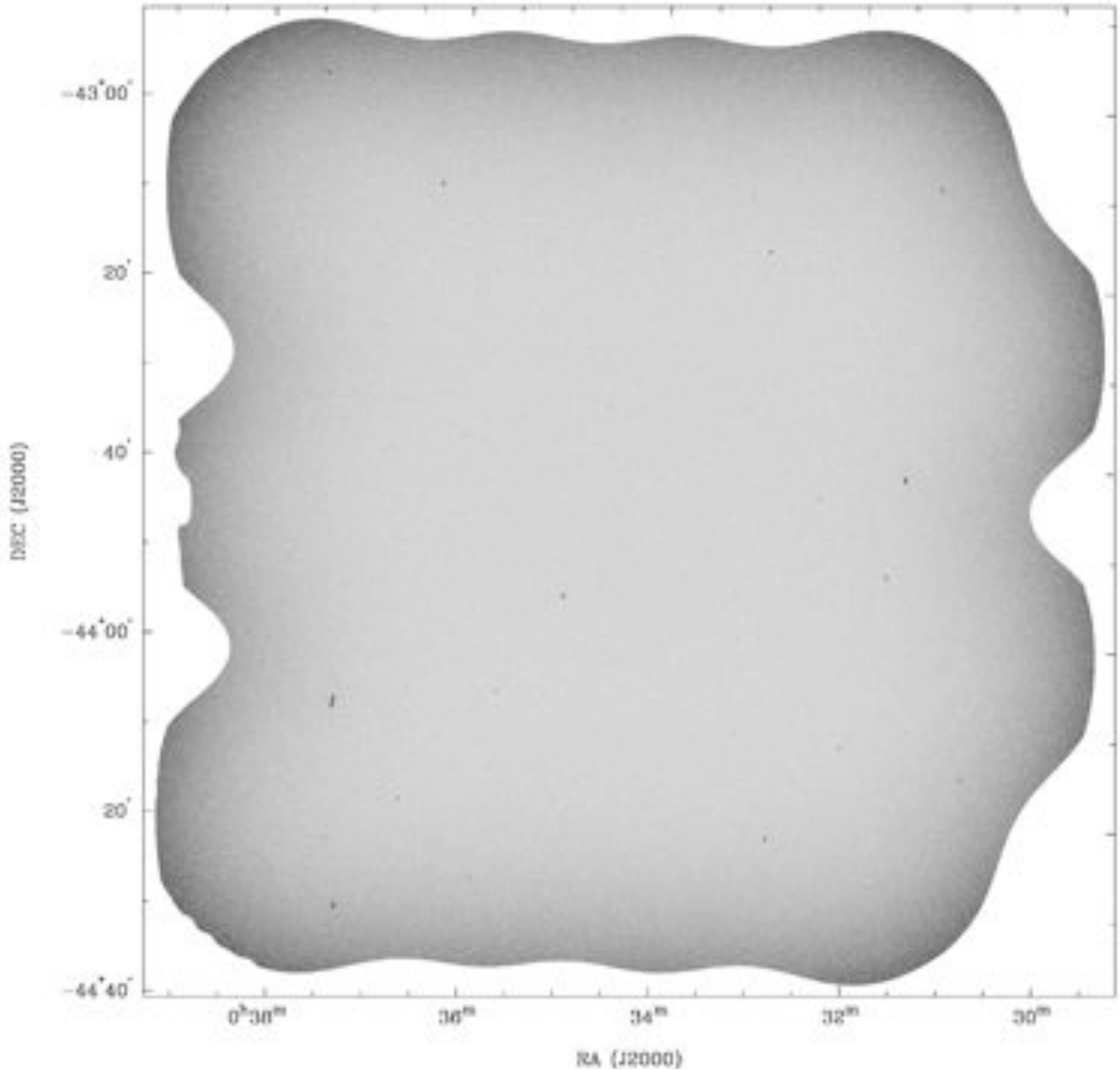


Figure 27. 1.4 GHz leakage-corrected linear polarization mosaic ($L_{\text{CORR}}^{\text{RM}}$) of the ELAIS-S1 ATLAS field in zenithal equal-area projection at a resolution of $10''.6 \times 6''.2$. The peak surface brightness is $3.8 \text{ mJy beam}^{-1}$ and the typical rms noise is $25 \mu\text{Jy beam}^{-1}$. The intensity scale is linear, saturating white at 0 mJy beam^{-1} and black above $0.4 \text{ mJy beam}^{-1}$.

Simpson C., et al., 2006, MNRAS, 372, 741
Singal J., Stawarz Ł., Lawrence A., Petrosian V., 2010, MNRAS, 409, 1172
Sopp H. M., Alexander P., 1991, MNRAS, 251, 14P
Spoelstra T. A. Th., 1997, Annals of Geophysics, 40, 4
Subrahmanyan R., Ekers R. D., Saripalli L., Sadler E. M., 2010, MNRAS, 402, 2792
Surace J. A., Shupe D. L., Fang F., Evans T., Alexov A., Frayer D., Lonsdale C. J., SWIRE Team, 2005, AAS, 37, 1246
Taylor A. R., et al., 2007, ApJ, 666, 201
Tucci M., Martínez-González E., Toffolatti L., González-Nuevo J., De Zotti G., 2004, MNRAS, 349, 1267

Tucci M., Toffolatti L., 2012, AdAst, 2012, 624987
Vernstrom T., Scott D., Wall J. V., 2011, MNRAS, 415, 3641
Vieira J. D., et al., 2010, ApJ, 719, 763
Vinyaikin E. N., Krotikov V. D., 2007, R&QE, 50, 542
Werner M. W., et al., 2004, ApJS, 154, 1
Wilman R. J., et al., 2008, MNRAS, 388, 1335
Windhorst R. A., Hathi N. P., Cohen S. H., Jansen R. A., Kawata D., Driver S. P., Gibson B., 2008, AdSpR, 41, 1965
Windhorst R. A., van Heerde G. M., Katgert P., 1984, A&AS, 58, 1
Windhorst R., Mathis D., Neuschaefer L., 1990, ASPC, 10, 389
Wood R., Field P. R., 2011, Journal of Climate, 24, 4800

Zhang X.-Z., Gray A., Su Y., Li J.-D., Landecker T., Zhang H.-B.,
Li C.-L., 2012, RAA, 12, 1297

APPENDIX A: COMPONENT CATALOGUE

This appendix presents the ATLAS 1.4 GHz DR2 component catalogue, a portion of which is displayed in Table A1 for guidance regarding its form and content. The catalogue lists a total of 2588 components in total intensity and linear polarization; no components were discovered in circular polarization. For ease of visual inspection, components have been grouped according to their nature of detection, arranged in the order total intensity then linear polarization. Components within each of these two groups are ordered by increasing right ascension. The columns of Table A1 are:

Column (1).—Component identification number. This gives the internal designation of the component used within our data processing. The form is a composite of three descriptors plus an optional fourth. The first is a single character that represents the ATLAS field, given by C for CDF-S or E for ELAIS-S1. The second descriptor is a single character that represents the nature of detection, given by T for total intensity or L for linear polarization. The third descriptor is an integer that gives the blob identification number assigned by BLOBCAT. The fourth descriptor is only suffixed for those components that were obtained through refitting all or part of the original blob using IMFIT, denoted by Cj, or BLOBCAT, denoted by Fj, for the j'th extracted component from a given blob.

Column (2).—Full ATLAS DR2 component name. This has been provided in a form acceptable for International Astronomical Union (IAU) designation (Lortet, Borde, & Ochsenbein 1994). The form is ATLAS2_JHHMMSS.SS+DDMMSS.ST where ATLAS2 is the survey acronym, J specifies the J2000.0 coordinate equinox, HH-MMSS.SS are the hours, minutes and truncated (not rounded) seconds of right ascension, + or − is the sign of declination, DDMMSS.S are the degrees, minutes and truncated seconds of declination, and the single character specifier in parentheses indicates the nature of detection as T or L. The position derives from Columns (3) and (4) below.

Columns (3) and (4).—Right ascension and declination (J2000.0) at intensity-weighted centroid.

Columns (5) and (6).—Absolute astrometric uncertainties in right ascension and declination. Minimum and maximum errors are 0".11 and 1".1 in right ascension, and 0".17 and 2".1 in declination, respectively.

Columns(7).—SNR of raw detection, A_s .

Column (8).—Local rms noise value, σ_s .

Column (9).—Local bandwidth smearing value, ϖ .

Columns (10) and (11).—Peak surface brightness corrected for bandwidth smearing, S_{peak} , and rms error, $\sigma_{S_{\text{peak}}}$.

Columns (12) and (13).—Integrated surface brightness, S_{int} , and rms error, $\sigma_{S_{\text{int}}}$.

Column (14).—Visibility area, V^{AREA} .

Columns (15) and (16).—Estimated deconvolved angular size or upper bound, Θ , and rms error, σ_Θ . If $\sigma_\Theta > 0$ then the component is resolved with flux density given by S_{int} . If $\sigma_\Theta = 0$, the component is unresolved with Θ representing an upper bound to the deconvolved angular size, and with flux density given by S_{peak} .

Column (17).—Deboosted flux density, S_{ML} .

See Section 5 and Hales et al. (2012b) for details regarding the parameters presented above.

Table A1. ATLAS 1.4 GHz DR2 Component Catalogue. This table has been truncated and is available in its entirety in the online version of this paper.

ID	Name (Prefix: ATLAS2.J) (2)	R.A. ($^{\circ}$, J2000.0) (3)	Decl. ($^{\circ}$, J2000.0) (4)	$\sigma_{R.A.}$ ($''$) (5)	$\sigma_{Decl.}$ ($''$) (6)	A_S (7)	σ_S (mJy b $^{-1}$) (8)	ϖ (9)	S_{peak} (mJy b $^{-1}$) (10)	$\sigma_{S_{peak}}$ (mJy b $^{-1}$) (11)	S_{int} (mJy) (12)	$\sigma_{S_{int}}$ (mJy) (13)	V^{AREA} (14)	Θ ($''$) (15)	σ_{Θ} ($''$) (16)	S_{ML} (mJy) (17)
ET383	002938.16–432946.7T	7.409023	-43.496308	0.45	0.64	11.06	0.069	0.84	0.913	0.095	0.999	0.086	1.000	7.08	0.00	0.897
ET691	002940.15–440309.3T	7.417319	-44.052597	0.75	1.07	6.51	0.066	0.85	0.509	0.083	0.401	0.069	0.990	10.64	0.00	0.481
ET780	002943.43–440812.1T	7.429743	-44.136712	0.82	1.18	5.89	0.066	0.84	0.462	0.082	0.309	0.068	0.977	11.59	0.00	0.430
ET727	002944.33–433629.7T	7.434732	-43.608272	0.78	1.12	6.21	0.069	0.83	0.516	0.087	0.527	0.074	0.991	11.06	0.00	0.484
ET71C2	002945.34–432148.4T	7.438933	-43.363466	0.16	0.20	73.51	0.071	0.85	6.141	0.324	8.495	0.431	1.000	5.29	0.50	8.495
ET71C1	002946.18–432149.2T	7.442417	-43.363667	0.15	0.20	79.93	0.070	0.85	6.630	0.348	9.107	0.461	1.000	5.22	0.51	9.107
ET125	002949.92–440541.3T	7.458010	-44.094817	0.17	0.23	46.01	0.059	0.86	3.164	0.175	3.461	0.183	1.000	2.90	0.00	3.161
ET760	002951.14–432354.3T	7.463110	-43.398433	0.81	1.16	5.99	0.060	0.87	0.413	0.072	0.316	0.062	0.953	11.43	0.00	0.385
ET197	002951.21–440556.5T	7.463388	-44.099045	0.23	0.32	25.40	0.059	0.86	1.725	0.111	1.811	0.108	1.000	4.12	0.00	1.721
ET986	002953.48–440618.7T	7.472854	-44.105196	0.96	1.37	5.06	0.058	0.87	0.336	0.069	0.315	0.060	0.883	13.34	0.00	0.303
ET158	003001.25–435046.6T	7.505240	-43.846287	0.20	0.26	33.96	0.058	0.85	2.300	0.136	2.589	0.142	1.000	3.46	0.00	2.297
ET481C1	003003.18–435950.9T	7.513271	-43.997472	0.60	0.86	9.11	0.051	0.89	0.520	0.063	0.579	0.059	0.992	8.14	0.00	0.505
ET956	003003.67–441238.4T	7.515330	-44.210670	0.93	1.33	5.18	0.060	0.85	0.363	0.072	0.370	0.063	0.915	13.03	0.00	0.329
ET929	003007.66–441329.8T	7.531941	-44.224947	0.92	1.31	5.26	0.058	0.85	0.359	0.071	0.354	0.061	0.910	12.85	0.00	0.326
ET997	003007.91–432725.6T	7.532983	-43.457133	0.97	1.38	5.01	0.048	0.90	0.268	0.055	0.201	0.049	0.762	13.48	0.00	0.240
ET375C1	003008.06–441148.5T	7.533613	-44.196822	0.48	0.68	12.08	0.058	0.87	0.807	0.078	0.933	0.075	1.000	6.65	0.00	0.796
ET590	003008.82–433320.5T	7.536756	-43.555700	0.67	0.95	7.35	0.046	0.89	0.377	0.055	0.362	0.049	0.928	9.62	0.00	0.361
ET375C2	003008.89–441144.7T	7.537071	-44.195772	0.85	1.21	6.59	0.058	0.87	0.436	0.070	0.505	0.063	0.965	10.53	0.00	0.413
ET62	003010.81–440907.7T	7.545050	-44.152158	0.14	0.18	108.20	0.052	0.88	6.392	0.331	7.220	0.365	1.000	3.07	0.86	7.220
ET445	003012.74–432245.8T	7.553084	-43.546061	0.52	0.74	9.54	0.045	0.90	0.476	0.055	0.387	0.049	0.982	7.87	0.00	0.464

APPENDIX B: SOURCE CATALOGUE

This appendix presents the ATLAS 1.4 GHz DR2 source catalogue, a portion of which is displayed in Table B1 for guidance regarding its form and content. The catalogue lists a total of 2221 sources as identified through the cross-identification and classification schemes presented in Section 6. Sources are ordered by increasing right ascension. The columns of the source catalogue are:

Column (1).—Source identification number. This gives the internal designation of the source used within our data processing. The form is a composite of two descriptors. The first is a single character that represents the ATLAS field, given by C for CDF-S or E for ELAIS-S1. The second descriptor is an integer that reflects the ordering of sources within each field, as described above.

Column (2).—Full ATLAS DR2 source name. This has been provided in a form appropriate for future IAU designation. The form is ATLAS2_JHHMMSS.SS+DDMMSS.S where ATLAS2 is the survey acronym, J specifies the J2000.0 coordinate equinox, HHMMSS.SS are the hours, minutes and truncated seconds of right ascension, + or – is the sign of declination, and DDMMSS.S are the degrees, minutes and truncated seconds of declination. If a SWIRE cross-identification was available, the position was specified by that of the infrared source. Otherwise, the position was calculated as the unweighted centroid of all total intensity components comprising the source.

Columns (3)–(8).—Component identification numbers for all total intensity components belonging to the source, corresponding to column (1) of Table A1. Up to 6 components may be provided; blanks are indicated by 0.

Columns (9)–(11).—Component identification numbers for all linearly polarized components belonging to the source, corresponding to column (1) of Table A1. Up to 3 components may be provided; blanks are indicated by 0.

Columns (12)–(14).—Component groupings and their Type classifications according to the linear polarization–total intensity association scheme presented in Section 6.2. Up to 3 groups may be provided, labelled A, B, and C. Each group is specified by a 9-digit string, where from left to right each digit corresponds to the respective components given in columns (3)–(11). If a component is not included in a particular group, then its respective digit is set to 9. All components belonging to a given group have their respective digit set to the Type classification for that group. Group A always represents the collection of all components comprising the source. Groups B and C represent subsets of components.

Columns (15) and (16).—Sum of deboosted flux densities for all total intensity components in Group A, and associated rms error. The error is given by the quadrature sum of the uncertainties from column (11) or (13) of Table A1, for unresolved or resolved components respectively.

Columns (17) and (18).—Same as Columns (15) and (16), but for deboosted flux densities of linearly polarized components in Group A.

Columns (19) and (20).—Same as Columns (15) and (16), but for Group B.

Columns (21) and (22).—Same as Columns (17) and (18), but for Group B.

Columns (23) and (24).—Same as Columns (15) and (16), but for Group C.

Columns (25) and (26).—Same as Columns (17) and (18), but for Group C.

Column (27).—Name of SDR3 counterpart. Listed as none for sources without an infrared cross-identification.

Columns (28) and (29).—Right ascension and declination (J2000.0), following the position definition provided for column (2).

Columns (30) and (31).—Sum of deboosted flux densities for all total intensity components belonging to the source, and associated rms error. The error is given by the quadrature sum of the uncertainties from column (11) or (13) of Table A1, for unresolved or resolved components respectively.

Columns (32) and (33).—Same as columns (30) and (31), but for linearly polarized components. For unpolarized sources, column (32) specifies the weakest polarization upper limit for any of the source’s total intensity components, calculated using Equation (20), while column (33) is set to zero.

Columns (34)–(38).—SWIRE infrared flux densities for the 3.6, 4.5, 5.8, 8.0, and 24.0 μm bands. Following Norris et al. (2006) we selected aperture extractions for unresolved infrared sources and extended (Kron) extractions for resolved sources. Entries specified as zero indicate that the infrared source was undetected.

Column (39).—Classification based on the criteria presented in Section 6.1. The categories are 0 = AGN, 1 = SFG, 2 = star, and 9 = unknown.

To illustrate use of Table B1 we interpret the data for source E26. The total intensity and linearly polarized flux densities for this source are given in Columns (30) and (32), respectively. Column (39) indicates that the source was classified as an AGN. Source E26 has a SWIRE cross-match given in Column (27) with infrared flux densities given in Columns (34)–(38). Source E26 comprises 2 total intensity components, ET71C1 and ET71C2, and a single linearly polarized component, EL26. Details for each of these components are given in Table A1. Continuing with Table B1, the polarization properties of source E26 are detailed in Columns (12)–(26). Column (12) indicates that the total intensity components from Columns (3) and (4), and the polarization component from Column (9), form a group (Group A) which has a Type 3 linear polarization–total intensity classification. This means that source E26 comprises a linearly polarized component situated midway between two total intensity components. The lack of classification information in Columns (13) and (14) indicates that smaller sub-groupings cannot be formed for source E26; it is not possible to form an unambiguous one-to-one cross-match between component EL26 and either of ET71C1 or ET71C2. The flux density information for Group A is given in Columns (15)–(18).

This paper has been typeset from a \LaTeX file prepared by the author.

Table B1. ATLAS 1.4 GHz DR2 Source Catalogue – Part I of III. This table has been truncated and is available as part of a single master table in the online version of this paper.

ID	Name	Total Intensity Component ID						Linear Pol. Component ID			Group		
(1)	(Prefix: ATLAS2_J) (2)	I1 (3)	I2 (4)	I3 (5)	I4 (6)	I5 (7)	I6 (8)	L1 (9)	L2 (10)	L3 (11)	A (12)	B (13)	C (14)
E232	002938.07–432947.9	ET383	0	0	0	0	0	0	0	0	999999999	999999999	999999999
E386	002940.19–440309.6	ET691	0	0	0	0	0	0	0	0	999999999	999999999	999999999
E420	002943.15–440813.6	ET780	0	0	0	0	0	0	0	0	999999999	999999999	999999999
E385	002944.36–433630.2	ET727	0	0	0	0	0	0	0	0	999999999	999999999	999999999
E26	002945.64–432149.3	ET71C1	ET71C2	0	0	0	0	EL26	0	0	339999399	999999999	999999999
E106	002949.92–440541.3	ET125	0	0	0	0	0	0	0	0	999999999	999999999	999999999
E468	002951.14–432355.3	ET760	0	0	0	0	0	0	0	0	999999999	999999999	999999999
E160	002951.26–440556.4	ET197	0	0	0	0	0	0	0	0	999999999	999999999	999999999
E577	002953.51–440617.8	ET986	0	0	0	0	0	0	0	0	999999999	999999999	999999999
E129	003001.30–435046.2	ET158	0	0	0	0	0	0	0	0	999999999	999999999	999999999
E367	003003.17–435951.4	ET481C1	0	0	0	0	0	0	0	0	999999999	999999999	999999999
E540	003003.73–441236.7	ET956	0	0	0	0	0	0	0	0	999999999	999999999	999999999
E543	003007.66–441329.8	ET929	0	0	0	0	0	0	0	0	999999999	999999999	999999999
E691	003007.95–432727.2	ET997	0	0	0	0	0	0	0	0	999999999	999999999	999999999
E487	003008.77–433321.6	ET590	0	0	0	0	0	0	0	0	999999999	999999999	999999999
E194	003008.87–441144.9	ET375C1	ET375C2	0	0	0	0	0	0	0	999999999	999999999	999999999
E56	003010.84–440907.1	ET62	0	0	0	0	0	0	0	0	999999999	999999999	999999999
E399	003012.78–433246.4	ET445	0	0	0	0	0	0	0	0	999999999	999999999	999999999
E426	003015.46–431201.1	ET680	0	0	0	0	0	0	0	0	999999999	999999999	999999999
E244	003015.62–441311.6	ET295C1	0	0	0	0	0	0	0	0	999999999	999999999	999999999

Table B1 – continued ATLAS 1.4 GHz DR2 Source Catalogue – Part II of III. This table has been truncated and is available as part of a single master table in the online version of this paper.

Group A				Group B				Group C			
$I_{20\text{cm}}$ (mJy)	$\sigma_{I_{20\text{cm}}}$ (mJy)	$L_{20\text{cm}}$ (mJy)	$\sigma_{L_{20\text{cm}}}$ (mJy)	$I_{20\text{cm}}$ (mJy)	$\sigma_{I_{20\text{cm}}}$ (mJy)	$L_{20\text{cm}}$ (mJy)	$\sigma_{L_{20\text{cm}}}$ (mJy)	$I_{20\text{cm}}$ (mJy)	$\sigma_{I_{20\text{cm}}}$ (mJy)	$L_{20\text{cm}}$ (mJy)	$\sigma_{L_{20\text{cm}}}$ (mJy)
(15)	(16)	(17)	(18)	(19)	(20)	(21)	(22)	(23)	(24)	(25)	(26)
0.000	0.000	0.000	0.000	0.000	0.000	0.000	0.000	0.000	0.000	0.000	0.000
0.000	0.000	0.000	0.000	0.000	0.000	0.000	0.000	0.000	0.000	0.000	0.000
0.000	0.000	0.000	0.000	0.000	0.000	0.000	0.000	0.000	0.000	0.000	0.000
0.000	0.000	0.000	0.000	0.000	0.000	0.000	0.000	0.000	0.000	0.000	0.000
17.601	0.631	0.671	0.075	0.000	0.000	0.000	0.000	0.000	0.000	0.000	0.000
0.000	0.000	0.000	0.000	0.000	0.000	0.000	0.000	0.000	0.000	0.000	0.000
0.000	0.000	0.000	0.000	0.000	0.000	0.000	0.000	0.000	0.000	0.000	0.000
0.000	0.000	0.000	0.000	0.000	0.000	0.000	0.000	0.000	0.000	0.000	0.000
0.000	0.000	0.000	0.000	0.000	0.000	0.000	0.000	0.000	0.000	0.000	0.000
0.000	0.000	0.000	0.000	0.000	0.000	0.000	0.000	0.000	0.000	0.000	0.000
0.000	0.000	0.000	0.000	0.000	0.000	0.000	0.000	0.000	0.000	0.000	0.000
0.000	0.000	0.000	0.000	0.000	0.000	0.000	0.000	0.000	0.000	0.000	0.000
0.000	0.000	0.000	0.000	0.000	0.000	0.000	0.000	0.000	0.000	0.000	0.000
0.000	0.000	0.000	0.000	0.000	0.000	0.000	0.000	0.000	0.000	0.000	0.000
0.000	0.000	0.000	0.000	0.000	0.000	0.000	0.000	0.000	0.000	0.000	0.000
0.000	0.000	0.000	0.000	0.000	0.000	0.000	0.000	0.000	0.000	0.000	0.000
0.000	0.000	0.000	0.000	0.000	0.000	0.000	0.000	0.000	0.000	0.000	0.000
0.000	0.000	0.000	0.000	0.000	0.000	0.000	0.000	0.000	0.000	0.000	0.000
0.000	0.000	0.000	0.000	0.000	0.000	0.000	0.000	0.000	0.000	0.000	0.000
0.000	0.000	0.000	0.000	0.000	0.000	0.000	0.000	0.000	0.000	0.000	0.000
0.000	0.000	0.000	0.000	0.000	0.000	0.000	0.000	0.000	0.000	0.000	0.000
0.000	0.000	0.000	0.000	0.000	0.000	0.000	0.000	0.000	0.000	0.000	0.000
0.000	0.000	0.000	0.000	0.000	0.000	0.000	0.000	0.000	0.000	0.000	0.000

Table B1 – *continued* ATLAS 1.4 GHz DR2 Source Catalogue – Part III of III. This table has been truncated and is available as part of a single master table in the online version of this paper.

SWIRE Name (Prefix: SWIRE3_⌋) (27)	R.A. (°, J2000.0) (28)	Decl. (°, J2000.0) (29)	$I_{20\text{cm}}$ (mJy) (30)	$\sigma_{I_{20\text{cm}}}$ (mJy) (31)	$L_{20\text{cm}}$ (mJy) (32)	$\sigma_{L_{20\text{cm}}}$ (mJy) (33)	$I_{3.6\mu\text{m}}$ (μJy) (34)	$I_{4.5\mu\text{m}}$ (μJy) (35)	$I_{5.8\mu\text{m}}$ (μJy) (36)	$I_{8.0\mu\text{m}}$ (μJy) (37)	$I_{24.0\mu\text{m}}$ (μJy) (38)	Class (39)
002938.07–432947.9	7.408625	-43.496639	0.897	0.095	0.524	0.000	25.22	26.13	0.00	0.00	0.00	0
002940.19–440309.6	7.417458	-44.052667	0.481	0.083	0.487	0.000	96.35	90.47	137.53	268.84	2278.89	0
002943.15–440813.6	7.429792	-44.137111	0.430	0.082	0.504	0.000	15.87	20.46	0.00	44.49	0.00	0
002944.36–433630.2	7.434833	-43.608389	0.484	0.087	0.535	0.000	75.55	80.69	74.30	0.00	0.00	0
002945.64–432149.3	7.440167	-43.363694	17.602	0.631	0.671	0.075	85.60	109.44	147.30	177.31	0.00	0
none	7.458010	-44.094817	3.161	0.175	0.429	0.000	0.00	0.00	0.00	0.00	0.00	0
002951.14–432355.3	7.463083	-43.398694	0.385	0.072	0.431	0.000	86.60	121.34	209.92	321.67	943.66	0
002951.26–440556.4	7.463583	-44.099000	1.721	0.111	0.421	0.000	12.33	7.72	0.00	0.00	0.00	0
002953.51–440617.8	7.472958	-44.104944	0.303	0.069	0.408	0.000	77.57	65.96	96.58	320.22	3744.82	9
003001.30–435046.2	7.505417	-43.846167	2.297	0.136	0.409	0.000	48.71	61.04	63.24	0.00	0.00	0
003003.17–435951.4	7.513208	-43.997611	0.505	0.063	0.339	0.000	32.75	37.27	50.42	0.00	0.00	0
003003.73–441236.7	7.515542	-44.210194	0.329	0.072	0.419	0.000	45.79	53.39	57.07	48.67	0.00	9
none	7.531941	-44.224947	0.326	0.071	0.410	0.000	0.00	0.00	0.00	0.00	0.00	9
003007.95–432727.2	7.533125	-43.457556	0.240	0.055	0.324	0.000	249.18	227.67	192.58	777.43	2843.39	1
003008.77–433321.6	7.536542	-43.556000	0.361	0.055	0.342	0.000	237.07	202.42	152.05	242.06	906.83	0
003008.87–441144.9	7.536958	-44.195806	1.208	0.105	0.381	0.000	126.14	95.56	67.32	0.00	0.00	0
003010.84–440907.1	7.545167	-44.151972	7.220	0.365	0.338	0.000	52.07	48.28	51.68	78.78	424.37	0
003012.78–433246.4	7.553250	-43.546222	0.464	0.055	0.319	0.000	77.30	62.01	49.32	59.59	0.00	0
003015.46–431201.1	7.564417	-43.200306	0.424	0.072	0.445	0.000	20.86	23.14	0.00	0.00	0.00	0
003015.62–441311.6	7.565083	-44.219889	0.842	0.075	0.362	0.000	441.01	341.78	183.83	163.94	0.00	0